



**NAVAL  
POSTGRADUATE  
SCHOOL**

**MONTEREY, CALIFORNIA**

**THESIS**

**THE EFFECTS OF APPLIED STRESS AND  
SENSITIZATION ON THE PASSIVE FILM STABILITY  
OF AL-MG ALLOYS**

by

Jennifer S. Fleming

June 2013

Thesis Advisor:  
Second Reader:

Luke N. Brewer  
Joseph C. Farmer

**Approved for public release; distribution is unlimited**

THIS PAGE INTENTIONALLY LEFT BLANK

REPORT DOCUMENTATION PAGE			Form Approved OMB No. 0704-0188	
Public reporting burden for this collection of information is estimated to average 1 hour per response, including the time for reviewing instruction, searching existing data sources, gathering and maintaining the data needed, and completing and reviewing the collection of information. Send comments regarding this burden estimate or any other aspect of this collection of information, including suggestions for reducing this burden, to Washington headquarters Services, Directorate for Information Operations and Reports, 1215 Jefferson Davis Highway, Suite 1204, Arlington, VA 22202-4302, and to the Office of Management and Budget, Paperwork Reduction Project (0704-0188) Washington DC 20503.				
1. AGENCY USE ONLY (Leave blank)		2. REPORT DATE June 2013	3. REPORT TYPE AND DATES COVERED Master's Thesis	
4. TITLE AND SUBTITLE THE EFFECTS OF APPLIED STRESS AND SENSITIZATION ON THE PASSIVE FILM STABILITY OF AL-MG ALLOYS			5. FUNDING NUMBERS	
6. AUTHOR(S) Jennifer S. Fleming				
7. PERFORMING ORGANIZATION NAME(S) AND ADDRESS(ES) Naval Postgraduate School Monterey, CA 93943-5000			8. PERFORMING ORGANIZATION REPORT NUMBER	
9. SPONSORING /MONITORING AGENCY NAME(S) AND ADDRESS(ES) N/A			10. SPONSORING/MONITORING AGENCY REPORT NUMBER	
11. SUPPLEMENTARY NOTES The views expressed in this thesis are those of the author and do not reflect the official policy or position of the Department of Defense or the U.S. Government. IRB Protocol number ___N/A___.				
12a. DISTRIBUTION / AVAILABILITY STATEMENT Approved for public release; distribution is unlimited			12b. DISTRIBUTION CODE	
13. ABSTRACT (maximum 200 words) This thesis evaluates effects of stress on the corrosion behavior for the aluminum magnesium alloy AA5083 in a comprehensive and systematic manner. This study used cyclic polarization and electrochemical impedance spectroscopy to study passive film stability of AA5083-H116, and sought to understand how applied and residual tensile and compressive stresses impact the passive layer film and the material's electrochemistry. Sample plates of AA5083 were sensitized to different levels to promote the formation of intergranular $\beta$ phase (Al <sub>3</sub> Mg <sub>2</sub> ). The corrosion response of these sensitized plates was measured after laser peening and during the application of an elastic tensile stress. The corrosion response of these materials was sensitive to the application of a tensile stress. As sensitization increased, the material surface became more electrochemically active, but the stability of the passive oxide film also increased. The passive film stability was reduced by the applied tensile stress while the degree of passivity was slightly increased. No clear correlation between laser peening and surface corrosion chemistry was observed.				
14. SUBJECT TERMS Aluminum-magnesium alloy, AA5083-H116, corrosion, cyclic polarization, electrical impedance spectroscopy, EIS, sensitization, laser peening, four-point bend apparatus, 1 molar NaCl, electrochemistry, U.S. Navy, DoD, Aluminum Alloy, corrosion, electrochemical analysis, current density, electrochemical electrodes, electrochemistry			15. NUMBER OF PAGES 147	
			16. PRICE CODE	
17. SECURITY CLASSIFICATION OF REPORT Unclassified	18. SECURITY CLASSIFICATION OF THIS PAGE Unclassified	19. SECURITY CLASSIFICATION OF ABSTRACT Unclassified	20. LIMITATION OF ABSTRACT UU	

THIS PAGE INTENTIONALLY LEFT BLANK

**Approved for public release; distribution is unlimited**

**THE EFFECTS OF APPLIED STRESS AND SENSITIZATION ON THE  
PASSIVE FILM STABILITY OF AL-MG ALLOYS**

Jennifer S. Fleming  
Lieutenant, United States Navy  
B.S., United States Naval Academy, 2006

Submitted in partial fulfillment of the  
requirements for the degree of

**MASTER OF SCIENCE IN MECHANICAL ENGINEERING**

from the

**NAVAL POSTGRADUATE SCHOOL  
June 2013**

Author: Jennifer S. Fleming

Approved by: Luke N. Brewer, PhD  
Thesis Advisor

Joseph C. Farmer, PhD  
Second Reader

Knox T. Millsaps, PhD  
Chair, Department of Mechanical and Aerospace Engineering

THIS PAGE INTENTIONALLY LEFT BLANK

## ABSTRACT

This thesis evaluates effects of stress on the corrosion behavior for the aluminum magnesium alloy AA5083 in a comprehensive and systematic manner. This study used cyclic polarization and electrochemical impedance spectroscopy to study passive film stability of AA5083-H116, and sought to understand how applied and residual tensile and compressive stresses impact the passive layer film and the material's electrochemistry. Sample plates of AA5083 were sensitized to different levels to promote the formation of intergranular  $\beta$  phase ( $\text{Al}_3\text{Mg}_2$ ). The corrosion response of these sensitized plates was measured after laser peening and during the application of an elastic tensile stress. The corrosion response of these materials was sensitive to the application of a tensile stress. As sensitization increased, the material surface became more electrochemically active, but the stability of the passive oxide film also increased. The passive film stability was reduced by the applied tensile stress while the degree of passivity was slightly increased. No clear correlation between laser peening and surface corrosion chemistry was observed.

THIS PAGE INTENTIONALLY LEFT BLANK

# TABLE OF CONTENTS

<b>I.</b>	<b>INTRODUCTION.....</b>	<b>1</b>
<b>A.</b>	<b>MOTIVATION .....</b>	<b>3</b>
<b>B.</b>	<b>BACKGROUND .....</b>	<b>7</b>
<b>C.</b>	<b>CORROSION.....</b>	<b>13</b>
	1. Pourbaix Diagrams .....	13
	2. Types of Corrosion.....	17
	3. Prevention and Mitigation .....	20
<b>D.</b>	<b>ELECTROCHEMISTRY OF THE AL-MG SYSTEM .....</b>	<b>21</b>
	1. Basic Electrochemical Reactions of the Al-Mg System .....	22
	2. Cyclic Polarization and Electrical Impedance Spectroscopy.....	25
	3. Basic Resistor-Capacitor Model .....	33
<b>E.</b>	<b>OBJECTIVES .....</b>	<b>38</b>
	1. Confirm Effects of Sensitization on Electrochemistry of Corrosion for AA5083-H116.....	38
	2. Assess the Effects of Elastic Stress on Electrochemistry of Corrosion for AA5083-H116.....	38
	3. Assess the Effects of Laser Peening on Electrochemistry of Corrosion for AA5083-H116.....	39
<b>II.</b>	<b>EXPERIMENTAL METHODS .....</b>	<b>41</b>
<b>A.</b>	<b>MATERIAL PROCESSING: FABRICATION AND APPLIED STRESSES OF TEST SAMPLES .....</b>	<b>41</b>
<b>B.</b>	<b>SAMPLE DISTRIBUTION AND SET-UP .....</b>	<b>41</b>
	1. Sensitized Batch .....	41
	<i>a. Control – Bend and Laser Peened Samples.....</i>	<i>41</i>
	<i>b. Bend Samples .....</i>	<i>42</i>
	<i>c. Sensitized Samples. ....</i>	<i>45</i>
	<i>d. Sensitized Bend Samples.....</i>	<i>46</i>
	2. Laser Peened Batch.....	46
	<i>a. Control Laser Peened Sample. ....</i>	<i>46</i>
	<i>b. Laser Peened Samples .....</i>	<i>47</i>
	3. Sample Summary .....	48
<b>C.</b>	<b>ELECTROCHEMICAL CELL SETUP AND GAMRY FRAMEWORK™ SETUP.....</b>	<b>48</b>
<b>III.</b>	<b>RESULTS .....</b>	<b>55</b>
<b>A.</b>	<b>CONTROL SAMPLES .....</b>	<b>61</b>
<b>B.</b>	<b>SENSITIZED SAMPLES.....</b>	<b>63</b>
	1. Sensitized Samples, 175°C for 24/48/72/96/156 Hours, Duration of Sensitization Comparison .....	63
	2. Sensitized Samples in Applied Tension.....	68
	<i>a. Sensitized Samples, 175°C for 156 Hours, 150 MPa Applied Tension.....</i>	<i>68</i>

	<i>b.</i>	<i>Sensitized Samples, 200°C for 336 Hours, 150 MPa Applied Tension.....</i>	<i>70</i>
	<i>c.</i>	<i>Sensitized Samples, 175°C for 156 Hours and 200°C for 336 Hours, 150 MPa Applied Tension .....</i>	<i>72</i>
	<i>d.</i>	<i>Summary.....</i>	<i>74</i>
	<b>C.</b>	<b>LASER PEENED SAMPLES .....</b>	<b>77</b>
<b>IV.</b>		<b>DISCUSSION .....</b>	<b>81</b>
<b>V.</b>		<b>CONCLUSIONS.....</b>	<b>85</b>
	<b>1.</b>	<b>Confirm Effects of Sensitization on Electrochemistry of Corrosion for AA5083-H116.....</b>	<b>85</b>
	<b>2.</b>	<b>Assess the Effects of Elastic Stress on Electrochemistry of Corrosion for AA5083-H116.....</b>	<b>85</b>
	<b>3.</b>	<b>Assess the Effects of Laser Peening on Electrochemistry of Corrosion for AA5083-H116.....</b>	<b>85</b>
<b>VI.</b>		<b>APPENDIX.....</b>	<b>87</b>
	<b>A.</b>	<b>MATLAB CODE – CYCLIC POLARIZATION CURVES.....</b>	<b>87</b>
	<b>B.</b>	<b>MATLAB CODE – ELECTRICAL IMPEDANCE SPECTROSCOPY: BODE AND NYQUIST PLOTS .....</b>	<b>91</b>
	<b>C.</b>	<b>SAMPLE CONDITIONS.....</b>	<b>96</b>
	<b>D.</b>	<b>CYCLIC POLARIZATION DATA .....</b>	<b>97</b>
	<b>1.</b>	<b>Supplemental Cyclic Polarization Comparison Charts for Sensitized Samples .....</b>	<b>100</b>
	<b>2.</b>	<b>Supplemental Cyclic Polarization Comparison Charts for Laser Peened Samples .....</b>	<b>104</b>
	<b>E.</b>	<b>ELECTRICAL IMPEDENCE SPECTROSCOPY DATA.....</b>	<b>107</b>
	<b>1.</b>	<b>Supplemental Electrical Impedance Spectroscopy Comparison Charts for Sensitized Samples .....</b>	<b>111</b>
	<b>2.</b>	<b>Supplemental Electrical Impedance Spectroscopy Comparison Charts for Laser Peened Samples .....</b>	<b>113</b>
	<b>F.</b>	<b>MODEL IMPEDENCE EDITOR DATA.....</b>	<b>114</b>
	<b>G.</b>	<b>SUMMARY TABLE DATA SCANS 1–3 EIS AND CP.....</b>	<b>118</b>
		<b>LIST OF REFERENCES.....</b>	<b>121</b>
		<b>INITIAL DISTRIBUTION LIST .....</b>	<b>127</b>

## LIST OF FIGURES

Figure 1.	Cracks on the deck hull of a CG-47 class guided missile cruiser caused by sensitized conditions. From R. Schwarting et al., <i>Manufacturing Techniques and Process Challenges with CG47 Class Ship Aluminum Superstructures Modernization and Repairs</i> [9].....	4
Figure 2.	LCS-1 (above) - Lockheed Martin's design of aluminum superstructure and steel hull; LCS-2 (below) - General Dynamics' design of an all-aluminum alloy hull. From <i>LCS: The USA's Littoral Combat Ships</i> [10].....	7
Figure 3.	Binary Al-Mg Phase Diagram. After <i>ASM International 2009</i> [2]. .....	9
Figure 4.	Schematic representing the mechanical process of sensitization and stress on Al-Mg alloys, primarily of $\beta$ phase migration of Al-Mg alloys and the process of IGSCC initiation. From <i>The Role of Stress in the Corrosion Cracking of Aluminum Alloys</i> [20]. .....	10
Figure 5.	Example of grain structure due to rolling direction. This is a composite micrograph displaying grain structure of a 38mm (1.5 in.) aluminum alloy 7075-T6 plate. From <i>ASM International 1999</i> [24].....	11
Figure 6.	Marcel Pourbaix derived diagrams for pure aluminum and its common passive oxide layers: hydrargillite, $\text{Al}_2\text{O}_3 \cdot 3\text{H}_2\text{O}$ (left) and böhmite, $\text{Al}_2\text{O}_3 \cdot \text{H}_2\text{O}$ (right) at 25°C in solution. After <i>Atlas of Electrochemical Equilibria in Aqueous Solutions 1974</i> [29].....	14
Figure 7.	Pourbaix diagram for pure Mg and a common passive oxide layer, magnesium hydroxide, $\text{Mg}(\text{OH})_2$ at 25°C in solution. After <i>Atlas of Electrochemical Equilibria in Aqueous Solutions 1974</i> [30]. .....	15
Figure 8.	Al-Mg Pourbaix diagram overlay, specifically for the passive layers of hydrargillite, $\text{Al}_2\text{O}_3 \cdot \text{H}_2\text{O}$ and $\text{Mg}(\text{OH})_2$ (left), and böhmite, $\text{Al}_2\text{O}_3 \cdot \text{H}_2\text{O}$ and $\text{Mg}(\text{OH})_2$ (right) at 25°C in solution, modified individual images of aluminum and magnesium passive layer film formation. After <i>Atlas of Electrochemical Equilibria in Aqueous Solutions 1974</i> [31] .....	16
Figure 9.	A summary of $\beta$ phase polarization experiments in chloride solutions; $E_{OC}$ is the open circuit potential, $E_{BD}$ indicates the breakdown potential, and $E_{CORR}$ indicates the corrosion potential. The AA5083-H116 corrodes freely in near-neutral chloride solutions; the $\beta$ phase is polarized above its breakdown potential, indicating that it will be selectively dissolved. From <i>The electrochemistry of intermetallic particles and localized corrosion in Al alloys</i> [32].....	17
Figure 10.	Venn diagram representation of the three conditions required in coexistence to initiate and propagate SCC, along with preventative measures.....	19
Figure 11.	Graphical Representation of the Laser Peening Process. From <i>Production Laser Peening of High Strength Metals</i> , Metal Improvement Company [36].....	21

Figure 12.	E-log(i) polarization curve for AA5083-H131 on the L-T plane as a function of sensitization. From <i>Spreading of intergranular corrosion on the surface of sensitized Al-4.4Mg alloys: A general finding</i> [3].	23
Figure 13.	Schematic of $\alpha$ and $\beta$ phase surface area and passive oxide layer thickness, representing the movement of cations and anions through the passive layer film. “X” represents the film thickness, O- represents the movement of oxygen cations, and M+ represents the movement of metal anions.	26
Figure 14.	Schematic of an Al-Mg alloy’s sensitized components in 0.6M NaCl Solution, represented by $\alpha$ (above) and $\beta$ (below) phase passive oxide layer resistor capacitor circuit setup.	27
Figure 15.	Example of a cyclic polarization scan of AA5083-H116, showing cathodic reduction, anodic oxidation, and pitting hysteresis loop without passive layer Film breakdown, for scan 2 of sample 19.	29
Figure 16.	Basic equipment overview and set-up for CP and EIS data collection. From <i>Cyclic Potentiodynamic Polarization Scans</i> [41].	32
Figure 17.	Basic R/C Circuit Model Set-Up for EIS. From <i>Cyclic Potentiodynamic Polarization Scans</i> [41].	35
Figure 18.	Impedance Model Editor: R/C circuit for AA5083-H116. R1 is the solution resistance, R2 is the polarization resistance, and C3 is the equivalent capacitance.	37
Figure 19.	An example of the Simplex Method impedance fit output provided by Echem Analyst™. Data for sample 28, scan 2.	37
Figure 20.	Four-point bend rig schematic. From ASTM-G39 [48].	43
Figure 21.	Diagram of top view (left) and side view (right) of four-point bend rig, dimensions in inches. From <i>The Role of Stress in the Corrosion Cracking of Aluminum Alloys</i> [20].	43
Figure 22.	Stress-strain data based on displacement and screw turns calculations, After <i>The Role of Stress in the Corrosion Cracking of Aluminum Alloys</i> [20].	44
Figure 23.	An example of samples without laser peening or sensitization in the bend rig (side view).	44
Figure 24.	Generalized schematic of the effect of temperature on Al-Mg alloys. Blue lines indicate the region of sensitization focused within this thesis research, and also indicate that the region of sensitization may be broader than shown. From Kramer et al. in <i>Locally Reversing Sensitization in 5xxx Aluminum Plate</i> [25].	46
Figure 25.	Laser peened samples, samples 7–10 from left to right, with varying intensities of laser peening.	47
Figure 26.	Laser peened samples, samples 11–14 from left to right, with varying intensities of laser peening.	48
Figure 27.	Fisher Scientific™ Accumet™ Engineering Corporation glass body Ag/AgCl reference electrode 13–620–53. From Fisher Scientific’s <i>Fisher Scientific™ Accumet™ Glass Body Ag/AgCl Reference Electrodes – Mercury-Free</i> website [49].	49

Figure 28.	Summary depiction of Gamry Instruments™ Universal Dummy Cell setup for lead connections to the potentiostat. ....	50
Figure 29.	Electrochemical cell setup: reference electrode type 13–620–53, counter electrode Hastelloy C-22, AA5083-H116.....	51
Figure 30.	Bending rig setup: sample in 150 MPa applied to lower edge, with tension along the electrochemically measured surface. ....	51
Figure 31.	Echem Analyst™ Electrochemical Impedance Spectroscopy Bode and Nyquist plot following a typical resistor – resistor/capacitor circuit model using the simplex method, showing $R_S$ , $R_P$ , and $R_S+R_P$ with curve fit data. ....	54
Figure 32.	Cyclic polarization curves: control sample 1, scans 1–3. ....	56
Figure 33.	Echem Analyst™ Bode and Nyquist overlay plot for sample 1, scans 1 and 4. ....	57
Figure 34.	Echem Analyst™ Bode and Nyquist plot for sample 1, scan 3: fits well to simple R/C circuit model and shows exceptional stability of AA5083-H116. ....	62
Figure 35.	Cyclic polarization curves: control samples, scan 3. ....	63
Figure 36.	Cyclic polarization curves: sensitized samples 175°C for 24/48/72/96/156 hours, scan 3. ....	64
Figure 37.	EIS scan 3, $R_P$ as a function of sensitization time for 175°C. ....	65
Figure 38.	CP scan 3, $i_P$ as a function of sensitization time for 175°C. ....	66
Figure 39.	CP scan 3, $\Delta E_{CRIT}$ as a function of sensitization time for 175°C. ....	67
Figure 40.	CP scan 3, $E_{CORR}$ as a function of sensitization time for 175°C. ....	68
Figure 41.	Cyclic polarization curves: control samples, 0 and 150 MPa applied tension, scan 3. ....	69
Figure 42.	Cyclic polarization curves: sensitized samples, 175°C for 156 hours, rolled L and T direction, 0 and 150 MPa applied tension, scan 3. ....	70
Figure 43.	Cyclic polarization curves: sensitized samples, 200°C for 336 hours, 0 and 150 MPa applied tension, scan 3. ....	71
Figure 44.	Cyclic polarization curves: non-sensitized and sensitized samples, 175°C for 156 hours and 200°C for 336 hours, 150 MPa applied tension scan 3, rolled L direction (above), rolled T direction (below). ....	73
Figure 45.	Summary chart explaining shifts in $i_P$ and $\Delta E_{CRIT}$ in regards to material corrosive behavior. ....	74
Figure 46.	Cyclic polarization curves: non-laser peened and laser peened samples 7 and 14, scan 3. ....	78
Figure 47.	EIS various laser peened conditions scan 3 comparison of $R_P$ . ....	79
Figure 48.	CP various laser peened conditions scan 3 comparison of $E_{CORR}$ . ....	79
Figure 49.	Leverage plots for regression model describing $R_P$ as a function of laser peening irradiance, pulse width, and number of passes. ....	80
Figure 50.	Transverse residual stresses as a function of depth in the 1–18–1 and 3–27–2 specimens at the 25 mm test point. From Banazwski (2011) [53]. ....	83
Figure 51.	CP sensitized conditions: 175°C for various durations, scans 2–3 comparison of $\Delta E_{CRIT}$ . ....	100
Figure 52.	CP sensitized conditions: 175°C for various durations, Scans 2–3 comparison of $\Delta E_{RP}$ . ....	100

Figure 53.	CP sensitized conditions: 175°C for various durations, scans 2–3 comparison of $E_{CORR}$ .....	101
Figure 54.	CP sensitized conditions: 175°C for various durations, scans 2–3 comparison of $i_p$ .....	101
Figure 55.	CP sensitized conditions: various sensitized conditions, bending applied, scans 2–3 comparison of $\Delta E_{CRIT}$ .....	102
Figure 56.	CP sensitized conditions: various sensitized conditions, bending applied, scans 2–3 comparison of $\Delta E_{RP}$ .....	102
Figure 57.	CP sensitized conditions: various sensitized conditions, bending applied, scans 2–3 comparison of $E_{CORR}$ .....	103
Figure 58.	CP sensitized conditions: various sensitized conditions, bending applied, scans 2–3 comparison of $i_p$ .....	103
Figure 59.	CP various laser peened conditions scans 2–3 comparison of $\Delta E_{CRIT}$ .....	104
Figure 60.	CP various laser peened conditions scans 2–3 comparison of $\Delta E_{RP}$ .....	105
Figure 61.	CP various laser peened conditions scans 2–3 comparison of $i_p$ .....	106
Figure 62.	EIS sensitized conditions: 175°C for various durations, scans 2–4 comparison of $R_p$ .....	111
Figure 63.	EIS various sensitized conditions, bending applied, scans 2–4 comparison of $R_p$ .....	112
Figure 64.	EIS various laser peened conditions scans 2–3 comparison of $R_p$ .....	113

## LIST OF TABLES

Table 1.	Comparison Chart of important physical properties of AA5083-H116 and hull ABS grade B structural steel. After AUSTIAL's publication <i>Aluminum Hull Structure in Naval Applications</i> [2].....	2
Table 2.	AA5083-H116 material composition list and weight percent. After <i>ASM International 1990</i> [19].....	9
Table 3.	SCE and Ag/AgCl electric potential variations in volts. After Gamry™ Instruments' <i>Reference Electrodes</i> website [50]. ....	49
Table 4.	Gamry Framework™ potentiostat EIS and CP experimental setup parameters. ....	52
Table 5.	Comparative results of EIS scan 1, 2, 3, and 4 for $\Delta R_p < 1000$ ohms. ....	61
Table 6.	EIS and CP scan 3 data, applied tension comparison of samples without sensitization, samples exposed to 175°C for 156 hours, and samples exposed to and 200°C for 336 hours. ....	76
Table 7.	Full sample list with conditions applied. ....	96
Table 8.	CP data for all samples scan 1. ....	97
Table 9.	CP data for all samples scan 2. ....	98
Table 10.	CP data for all samples scan 3. ....	99
Table 11.	EIS data for all samples scan 1. ....	107
Table 12.	EIS data for all samples scan 2. ....	108
Table 13.	EIS data for all samples scan 3. ....	109
Table 14.	EIS data for all samples scan 4. ....	110
Table 15.	Impedance Model Editor data scan 1. ....	114
Table 16.	Impedance Model Editor data scan 2. ....	115
Table 17.	Impedance Model Editor data scan 3. ....	116
Table 18.	Impedance Model Editor data scan 4. ....	117
Table 19.	EIS and CP scan 1 data, applied tension comparison of samples without sensitization, samples exposed to 175°C for 156 hours, and samples exposed to and 200°C for 336 hours. ....	118
Table 20.	EIS and CP scan 2 data, applied tension comparison of samples without sensitization, samples exposed to 175°C for 156 hours, and samples exposed to and 200°C for 336 hours. ....	118
Table 21.	EIS and CP scan 3 data, applied tension comparison of samples without sensitization, samples exposed to 175°C for 156 hours, and samples exposed to and 200°C for 336 hours. ....	119

THIS PAGE INTENTIONALLY LEFT BLANK

## LIST OF ACRONYMS AND ABBREVIATIONS

ASTM	American Society for Testing and Materials
BAE	British Aerospace and Defence Company
CP	cyclic polarization
DoD	Department of Defense
DON	Department of the Navy
$E_{BD}$	breakdown potential
$E_{CORR}$	corrosion potential
$E_{CRIT}$	critical potential
EIS	Electrochemical Impedance Spectroscopy
$E_{OC}$	open circuit potential
$E_{RP}$	repassivation potential
FSW	friction stir weld
$i_{CORR}$	corrosion current density
IGC	intergranular corrosion
IGSCC	intergranular stress corrosion cracking
$i_p$	passive current density
J	imaginary number – square root of negative one
LP	laser peening
NAMLT	nitric acid mass loss test
$R_p$	polarization resistance
$R_s$	solution resistance
SCC	stress corrosion cracking
USN	United States Navy
wt%	weight percent
Z	complex electrochemical impedance
$Z'$	real part of the complex impedance
$Z''$	imaginary part of the complex impedance

THIS PAGE INTENTIONALLY LEFT BLANK

## ACKNOWLEDGMENTS

First, I would like to express my deepest gratitude to my thesis advisor, Dr. Luke Brewer, for not only his esteemed guidance and advice, but for his patience and dedication to me as a student. He is responsible for introducing me to the world of material science two years ago with a relentless spirit of exploration and research, and acts as a role model for all of his students. As one of the most inquisitive people I know, he never settles for “good enough,” and never lets his students do the same. Dr. Brewer, or as I like to call him, XO, always searches for new angles to look at things and constantly employs his students with the drive to succeed. His dedication to research and his student’s progression are unprecedented, and he afforded me the opportunity to participate in research that I was interested in. One could not ask for a better, more patient supervisor.

I would also like to express my truest appreciation of my second reader, Dr. Joseph Farmer, for his clarity and insight in the arena of corrosion. Without his knowledge and expertise, this research would not be successful. His network with Lawrence Livermore National Laboratory and the Metal Improvement Company also contributed to several aspects of this thesis. Dr. Farmer provided me with a very thorough knowledge and insight to corrosion science with a contagious enthusiasm. The educational value of corrosion science he brings to the table is unbounded, and I am truly grateful to have the opportunity to pick his brain. His knowledge passed down to me from him will be carried with me as I return back to the fleet.

I would like to thank the OSD Corrosion Policy and Oversight Office for providing the research institution with the financial backbone of the experimentation. Their funding enabled research in the areas of prevention and mitigation of corrosion. Without their funding, the tools available for the experimentation process in my research could not be complete.

I cannot forget to thank the people responsible tremendous amount of knowledge and leadership that pulses through the hallways of Watkins Hall. Professors, research

associates, lab technicians, and staff alike enabled me to do exactly what I wanted to do. I learned an incredible amount about mechanical engineering in my short time here that I intend to carry forward. My fellow squids (SWOs, EDOs, and nukes alike) made the pain and suffering bearable. Their diverse backgrounds and colorful personalities fed my academic spirit, and they genuinely made life so much more enjoyable. I am truly thankful for all of the people I was blessed to have crossed paths with here at the Naval Postgraduate School.

Beyond research and academics, I have to thank my family (old and new) for their unconditional love and support. I would like to thank my parents, Rick and Carol Sanders, for supporting me through all my personal, educational and career endeavors since I was born. Their sacrifice to give my brother, sister, and me opportunities that they never had will live in my soul forever. Their footprint on my self-being is one that I will never underestimate or underappreciate. I would like to thank my brother for motivating me to work harder by keeping in touch with me and letting me be a part of his advancement as an airman and combat medic. His own personal achievements drive me to be a better person. We are all proud of him. I would like to thank my sister for taking time out for me, to live and stay with me here in Monterey as she pursues her own achievements in academics. She keeps me young. I would like to thank my new Fleming family, as they have provided several encouraging words and prayers over the last year that I have known them.

Last, but not least, I would like to thank my soul mate and newly wedded husband for his incredible amount of support and patience. Two military newlyweds accomplishing work on their master's thesis sounds, to me, like a lot of alone time, late nights, and distance, but not with Will. Sharing this experience with him for our time together here at NPS is truly unique and unforgettable. Will gets me; he appreciates my core values, he understands my humor, and he loves the person I am with all of my flaws. He shows his faith in my intellectual capabilities, even when I'm typing away or studying at 4am. He kept me sane and motivated to continue my research through the duration of this process. We have both grown and learned a lot about life and love with each other, and are only getting stronger.

# I. INTRODUCTION

The structural benefits of using aluminum alloys on naval vessels have been widely recognized throughout the marine industry as a means for improving a ship's efficiency. Reduced fuel expenditures and increased load requirements have become the driving forces for hull design; a lighter hull can reduce the fuel costs required to power the ship through the water and improve a ship's stability by lowering the center of gravity.

Several design factors affect the choice of an engineering material, which include electrochemical, metallurgical, thermodynamic, physical, and chemical aspects [1]. The most common of the marine grade aluminum alloys seen in the U.S. Navy's surface fleet are 5086, 5038, 5456, 5454, 6005, 6061, and 6082 [2]. The most desirable properties of 5000 and 6000 series aluminum alloys are their lightweight characteristics combined with overall strength and limited susceptibility to corrosion, especially in the eyes of budget analysts viewing increasing costs of fuel and corrosion repairs in the United States. Inevitably, reducing power requirements reduces fuel costs and ultimately saves the DoD billions of dollars on order of more than 20% in fuel costs per year [2]. Table 1 is a comparison of the important physical properties of AA5083-H116 with ABS grade B structural steel; note the specific weight of the aluminum alloy is much less than that of steel.

Material Properties	Units	AA5083-H116	ABS Grade B Structural Steel
Specific Weight	g/cm <sup>2</sup>	2.66	7.85
Melthing Point	°C	640	1450
Coefficient of Linear Expansion	10 <sup>-6</sup> °C <sup>-1</sup>	23.8	11.7
Speific Heat	J kg <sup>-1</sup> °C <sup>-1</sup>	960	460
Thermal Conductivity	W m <sup>-1</sup> °C <sup>-1</sup>	120	50
Proof Stress	0.2 PS, MPa	215	235
Tensile Stress	UST, MPa	305	400
% Elongation	%	10	40
Elastic Modulus	GPa	70	210
Notes	Minimum values displayed		

Table 1. Comparison Chart of important physical properties of AA5083-H116 and hull ABS grade B structural steel. After AUSTIAL's publication *Aluminum Hull Structure in Naval Applications* [2].

Marine grade aluminum alloys are a desirable material choice when competing demands exist for a lightweight, strong, and corrosion resistant material. In particular, this thesis will evaluate the use of aluminum alloy AA5083-H116, which is a non-heat treatable alloy with good corrosion resistance, weldability, and strength [3]. This alloy is commonly used in welded pressure vessels, marine structures, auto aircraft cryogenics, drilling rigs, TV towers, transportation equipment, and missile components. The 5000 series marine grade aluminum alloys used in shipbuilding have a relatively good strength when compared to pure aluminum, as the addition of magnesium, in general, reinforces the alloy and fashions a stronger metal, but it can also be the cause of stress corrosion cracking (SCC) observed on many ships. The 5000 series aluminum alloys are generally resistant to corrosion. The addition of Mg, however, when exposed to elevated temperature conditions, sensitizes the alloy and proves to be largest drawback of this material. As a result, shipboard operators, sailors, and contractors have seen the devastating effects of sensitization, stress corrosion cracking, intergranular cracking, and other forms of corrosion that overwhelm this material over time.

## A. MOTIVATION

The U.S. navy fleet consists of 283 ships, 249 of which are actively commissioned [4]. As recently as 2009, Department of Defense (DoD) spends \$880 million per year on corrosion alone annually on Navy ships, at approximately \$3.1 million per year per ship and the number ever increasing as service life extends with increasing maintenance requirements [4], [5]. As recently as 2012, the Department of the Navy (DON) spent \$7 billion annually (25% of the DON's budget) on aviation, ships, ground vehicles and facilities, with \$3.1B dedicated solely to ships [5]. There is much information and research to be gathered in the area of corrosion prevention and mitigation from previous ships with aluminum superstructures that can be applied to today and tomorrow's Navy.

Guided missile destroyers (DDG), guided cruisers (CG) and guided missile frigates (FFG) have all suffered in the Navy's past with corrosion in aluminum superstructures and hulls. An early generation of the Arleigh Burke Class of guided missile destroyers proved valuable in "lessons learned" for the U.S. Navy after building an aluminum superstructure with a steel hull in 1975 aboard the USS Belknap and again in 1982 aboard Royal Navy warships when fires burned down their superstructures in combat [6]. These ships also proved susceptible to cracking. In 1987, it was believed that aluminum cracked at much lower stresses than steel, and the belief was that aluminum alloys did not have the inherent strength that steel did and would thus require significantly more maintenance than with steel [6]. Prior to DDG-51, all U.S. surface combatants from 1947 onward had aluminum in their deckhouses [6]. During this period, it cost the Navy approximately \$445,000 thousand to repair each ship [6]. The ultimate cause in 1987 was determined to be a design flaw and was not thought of as a materials problem at the time. The Navy eventually reverted back to all-steel superstructures and hulls for DDG-51 Arleigh Burke class [6]. The CG-47 class guided missile cruiser was constructed with aluminum alloys to meet stability and naval architectural requirements in hull design. The CG-47 class has experienced significant superstructure cracking that can be divided into two general categories: fatigue cracking brought about by stress concentration and stress corrosion cracking brought about by material degradation and sensitization of the

aluminum alloys, the consequences of which can be seen in Figure 1. These superstructure cracking problems catalyzed the start of the CG-47 Class Aluminum Superstructure Task Force in the U.S. Navy to study various alternatives to eliminate superstructure cracking issues and was coordinated by the Commander, Naval Sea (NAVSEA) Systems command, Naval Systems Engineering Directorate (SEA05), and Surface Warfare (SEA21) [7]. Great efforts were made in assessing cost, schedule, and risk implications for wholesale superstructure replacement versus sectional replacement of the superstructure during shipyard repair availabilities as directed by the Chief of Naval Operations [7]. This class of ship was and is the driver of problem solving for aluminum superstructure repair and prevention [7]. In 1994, the FFG-7 class suffered several issues with superstructure welding. The superstructure was reported as suffering from extensive cracking in this class of ship, and the cause was determined to be a combination of high design stress coupled with poor quality welding [8]. Cracks spread across the 02 level weather deck in the middle of the superstructure, where stresses proved detrimental [8]. Several shipboard alterations proved unsuccessful in efforts to repair the cracks, and more stringent quality assurance measures and welding procedures were implemented [8].

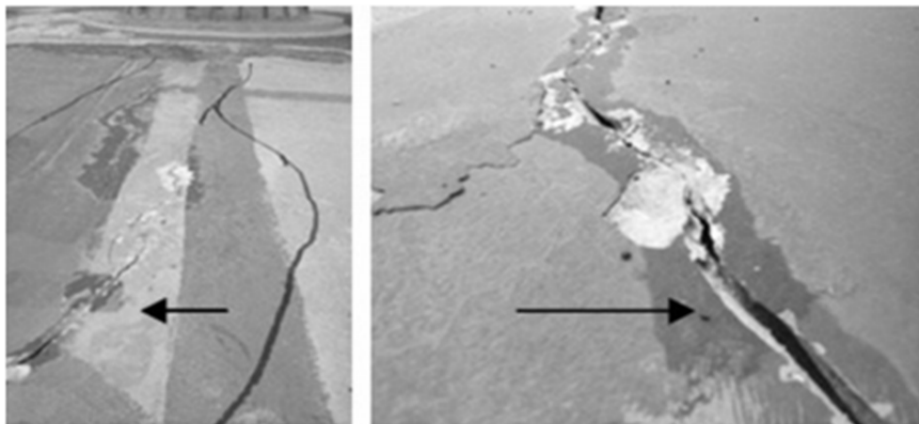


Figure 1. Cracks on the deck hull of a CG-47 class guided missile cruiser caused by sensitized conditions. From R. Schwarting et al., *Manufacturing Techniques and Process Challenges with CG47 Class Ship Aluminum Superstructures Modernization and Repairs* (From [9]).

The challenges associated with aluminum superstructures must be solved for the present and future navy as well as for the past. As the navy progresses with new ships, like the littoral combat ship (LCS), the requirement to solve these problems becomes evident. As the DON aims to replace 30 FFG-7 Oliver Hazard Perry class frigates and 14 MCM Avenger class mine countermeasure vessels, and 12 MHC-51 Osprey Class coastal mine hunters in an effort to fulfill the Navy's surface combatant force transformation strategy, the DON is forced to ensure that the LCS program maintains a cost affordable life cycle. This budgetary requirement is driven by the reduction in manpower in the navy, an increase in operational tempo, and with the emphasis on multi-functional ships [10]. With only the 4th of 52 LCS class ships built, and shipbuilding reportedly behind schedule, the task at hand is growing. LCS-1 (commissioned in 2006) and similarly LCS-2 (commissioned in 2008) are already reporting several discovered cracks and problems with galvanic corrosion in the hull and superstructure and already require interim repairs [11]. These problems can be seen as an opportunity for improvement and prevention breakthroughs on these ships that require less financial expenditure and manpower than the daily painting rigor, minor overhauls required every 5–10 years, and major overhauls every 10–20 years. Both LCS variants must address the corrosion and fatigue cracking issues associated with the use of aluminum structures: Lockheed Martin's design of an aluminum superstructure and steel hull and General Dynamics' design of an all-aluminum structure with steel reinforcements and stiffening [4]. SCC has been identified as one of the primary problems, increasing repair requirements for sensitized materials [9]. As mentioned earlier, with no defined fatigue limit, aluminum and its alloys are susceptible to fatigue.

Marine grade aluminum alloys have several properties that are ideal for shipboard use. They exhibit a high strength to weight ratio with one third the density of steel [12]. Marine grade aluminum alloys provide excellent corrosion resistance [13], as they form a naturally passive oxide layer preventing further oxidation [12]. These metals are easily weldable and machinable; they are available for a diverse selection of functional products with high thermal and electrical conductivity, but are non-magnetic [14]. When the structure using these materials reaches its total life cycle, aluminum alloys prove to be

easily recycled [14], [15]. Because of marine grade aluminum alloy's properties, the opportunity exists for the DON and DoD to increase their capabilities at sea. These alloys, by being lightweight, increase fuel savings and ship range. Secondary and tertiary effects of lightweight ship designs are increased payloads, higher speeds, better maneuverability, improved stability, and less maintenance [14]. These factors add up to reduce the total ownership costs and acquisition costs [14]. Most of the total ownership costs reside in operations and sustainment. Lighter structures result in fuel savings. For instance, a frigate fuel savings will be 71 tons per voyage with an annual cost savings of 1,278,000 over an all-steel design [14]. For a 25 year life-cycle, fuel cost savings alone would be 32 million dollars; there is no need to paint 5000 series aluminum, and in the end, there is a higher residual value at the end of life scrapping, as nearly 75% of aluminum made in the past is used today [16]. Nearly 90% of cost to fabricate a hull structure is labor, but only 1% of total ship cost is materials, and aluminum reduces labor costs by machinability to produce diverse forms such as sheet and plate extrusions, castings, and forgings, which enable part consolidation and design simplification [14].



Figure 2. LCS-1 (above) - Lockheed Martin's design of aluminum superstructure and steel hull; LCS-2 (below) - General Dynamics' design of an all-aluminum alloy hull. From *LCS: The USA's Littoral Combat Ships* (From [10]).

## **B. BACKGROUND**

The International Alloy Designation System is the most widely accepted naming convention for aluminum alloys. In particular, the 5000 series are alloyed with magnesium and are used in many marine applications. In aerospace and aircraft applications, typically 7000, 6000, 5000 or 2000 series aluminum alloys are used because of their high strength and relatively low susceptibility to corrosion [17]. Marine alloys for boat and shipbuilding are 5000 and 6000 series aluminum for salt water sensitive applications [17]. Temper designations include the following a cast or wrought designation number with a dash, a letter, and one to three digit number following the letter: F is as fabricated with no special control performed to the heat treatment or strain hardening after the shaping process; O is annealed which is the lowest strength and highest ductility temper. H is strain hardened and only applied to wrought products, which are used for products that have been strengthened by strain hardening, with or without subsequent heat treatment and is followed by two more numbers; W is solution

heat treated and seldom encountered due to its instability as a temper treated alloy; T is solution heat treated for products strengthened by heat treatment with or without subsequent strain hardening [16]. The first digit for H temper strain hardening codes represent the strain hardening process applied; H typically indicates a wrought product in alloys containing over a nominal 4% of magnesium [16]. For wrought aluminum alloys, H1 is strain hardened only with no annealing, while H2 is strain hardened with partial annealing, H3 is strain hardened and stabilized, while H4 is strain hardened and lacquered or painted. The second digit denotes the degree of hardness or level of strain hardening and is based on the minimum ultimate tensile strength obtained and the third digit is a variation of the two digit temper [16]. AA5083 is the most popular base metal for shipbuilding in the U.S as a highly available, excellent strength, corrosion resistance, formability and weldable alloy. In summary, AA5083-H116 is 5000 series aluminum wrought alloy used in many practical marine applications. It is a low density, high strength, corrosion resistant alloy with strain hardening applied without annealing and the first degree of hardness. It also has an ease of fabrication and diversity of form. Several articles go as far as to say that aluminum alloys are so corrosion resistant that they do not require painting [18], which is not the case.

The composition of AA5083 is nominally Al (92.4–95.6 wt%, 66.46–67.21 at%). (Table 2). Using this information, we can discern the applicable areas of the binary phase diagram for Al-Mg alloys in Figure 3. At this magnesium concentration, this system has more than one phase in equilibrium at room temperature. The red lines in this diagram indicate the Al-Mg composition range in which AA5083-H116 aluminum alloy is found using atomic percent (at%). AA5083-H116 at room temperature is in the  $\alpha+\beta$  two phase region. Although other elements are present in AA5083, the stress corrosion crack behavior is driven by the interplay between aluminum and magnesium.

Component	Wt. %
Al	92.4 - 95.6
Cr	0.05 - 0.25
Cu	Max 0.1
Fe	Max 0.4
Mg	4 - 4.9
Mn	0.4 - 1
Si	Max 0.4
Ti	Max 0.15
Zn	Max 0.25

Table 2. AA5083-H116 material composition list and weight percent. After *ASM International 1990* (After [19]).

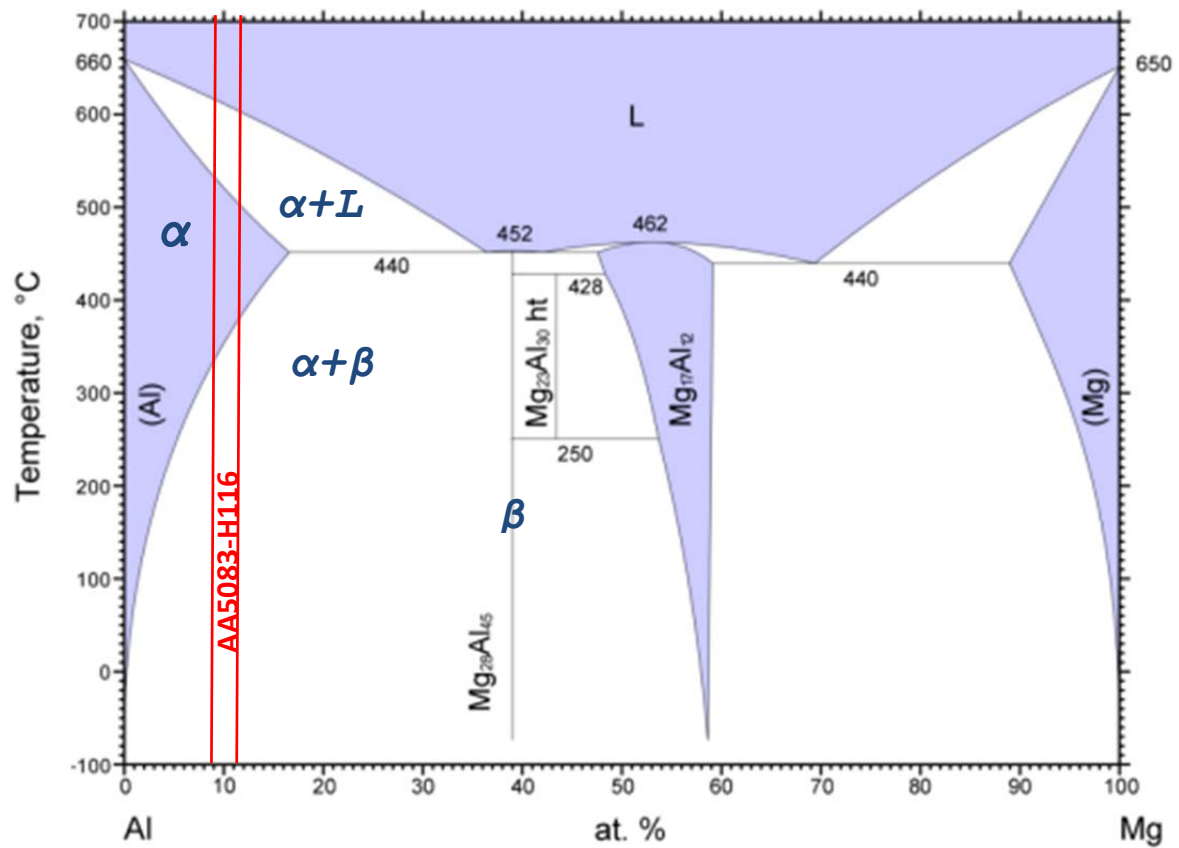


Figure 3. Binary Al-Mg Phase Diagram. After *ASM International 2009* (After [2]).

The effects of composition on the properties of Al-Mg alloys are significant. For 5000 series aluminum, exposure to relatively high temperatures causes the magnesium atoms to migrate toward the grain boundaries, resulting in precipitation of  $\text{Al}_3\text{Mg}_2$ , or  $\beta$ , phase. This process is termed grain boundary sensitization and is the central cause behind intergranular stress corrosion cracking (IGSCC). While studies have demonstrated that 5000 series aluminum alloys, because of their spontaneously formed passive oxide layer, are resistant to corrosion, further investigations have shown that microstructural changes can, in fact, negatively impact corrosion performance [9]. The microstructural changes caused by sensitization are important to discuss, as the material becomes susceptible to intergranular stress corrosion cracking, or IGSCC, by tensile stress as shown in Figure 4. In this figure, the effects of both intergranular stress corrosion and pitting associated with other intermetallics are represented.

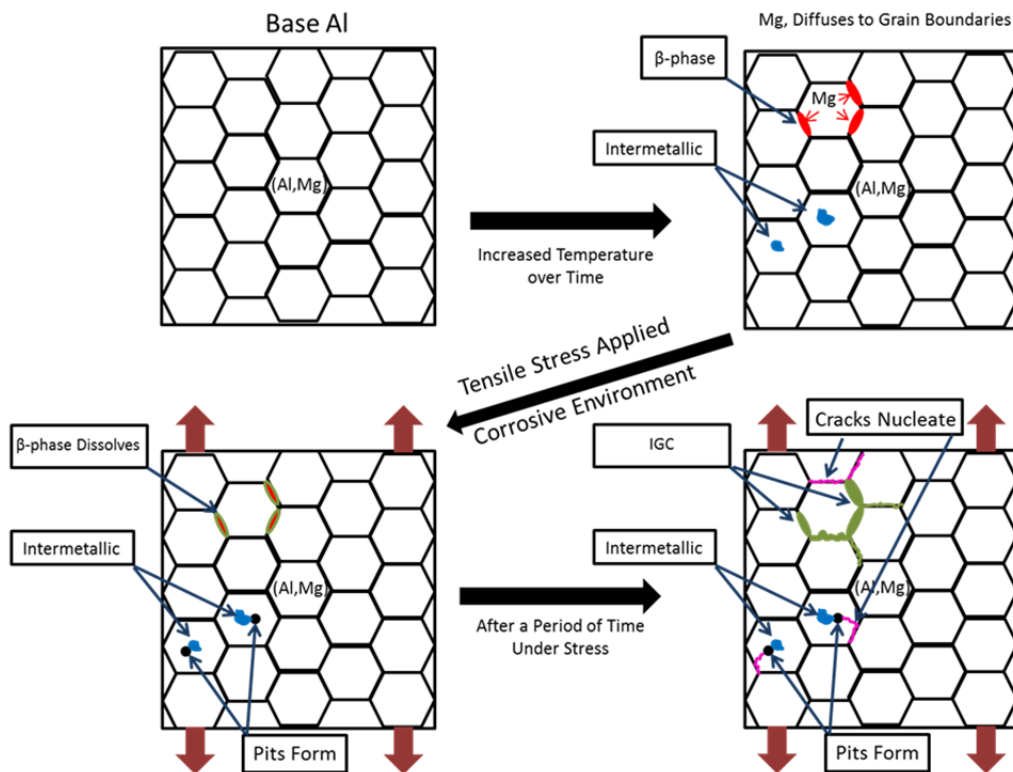


Figure 4. Schematic representing the mechanical process of sensitization and stress on Al-Mg alloys, primarily of  $\beta$  phase migration of Al-Mg alloys and the process of IGSCC initiation. From *The Role of Stress in the Corrosion Cracking of Aluminum Alloys* (From [20]).

An important factor when studying the physical aspects of aluminum alloys is microstructural anisotropy. This anisotropy is created by the rolling of the material during processing. The grain structure directions are significant. “L” is the longitudinal direction, “T” is the transverse direction, and “S” is the short transverse direction. Observations of material behavior based on rolling directions show that fatigue strengths may be significantly lower in the S direction than in the T direction; for example, AA5083-H113 plate, the fatigue strengths of the S direction are significantly lower [21]. The S direction endurance limit is approximately 76 MPa (11 ksi) compared to 134 MPa (19.5 ksi) for L directions [21]. AA5083-H116 is specifically rolled to prevent  $\beta$  phase grain boundary precipitation and improve the resistance of standard AA5083 to intergranular corrosion (IGC) and SCC [22], [23]. Figure 5 is provided for rolling direction clarity.

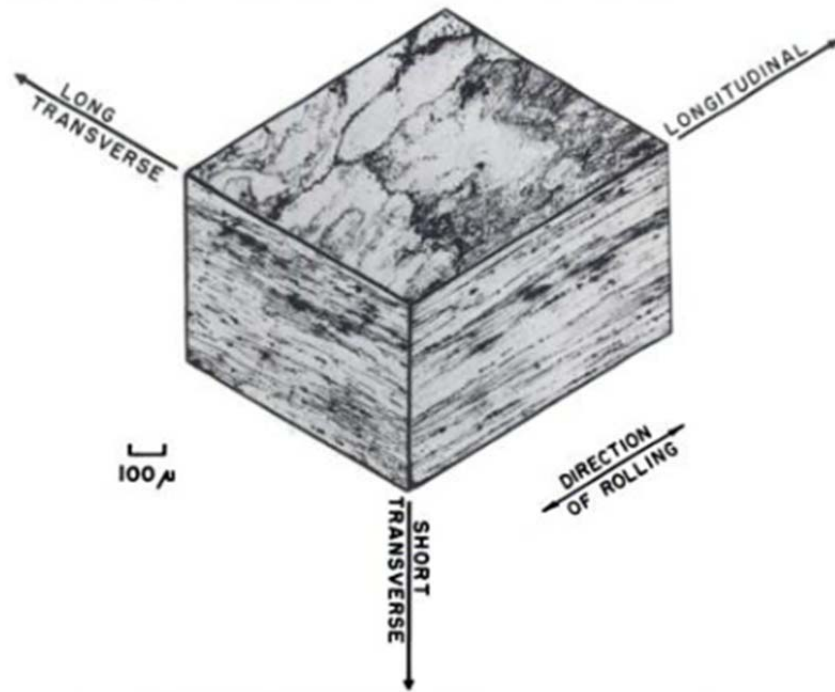


Figure 5. Example of grain structure due to rolling direction. This is a composite micrograph displaying grain structure of a 38mm (1.5 in.) aluminum alloy 7075-T6 plate. From *ASM International 1999* (From [24]).

Grain boundary sensitization of Al-Mg alloys is a key reason for failure. Several previous studies have shown that the sensitization of Al-Mg alloys causes weakening of the material. The deterioration of mechanical properties is directly related to the level of susceptibility to intergranular corrosion or cracking, and can be attributed to grain boundary precipitation of magnesium-rich particles. In addition, Al-Mg alloys suffer a loss in tensile and hardness properties due to the softening caused by the decrease in Mg solute solid solution concentration with increasing sensitization over time and temperature by recrystallization [13], [15]. The preferential precipitation of  $\text{Al}_2\text{Mg}_3$  along the grain boundaries is the main cause of IGC and SCC susceptibility [13]. The degree of  $\beta$  precipitation on grain boundaries is a function of sensitization time and temperature [15]. The critical temperature Oguocha et al. found at which AA5083-H116 is the most susceptible to IGC is between 150 and 200°C [15]. At 200°C, the precipitation rate of the  $\beta$  phase alloy decreased, as the solubility of magnesium in aluminum is increased [15]. Jain et al. conducted an experiment that used sensitized conditions 100°C at 3, 7, 14, and 30 days [3]. They studied the potentiostatic current versus time that detected transient pitting activity, and they found that the breakdown potential of the  $\beta$  phase, using 0.6 M NaCl, is at least 200 mV lower than the open circuit potential ( $E_{OC}$ ), and applied potentials in the range between the two breakdown potentials trigger intergranular corrosion via attack of the  $\beta$  phase precipitates at the grain boundaries [3]. Searles and Buchheit found the sensitization range to be from 50 to 200°C [13]. The open circuit potential in Searles' et al. discussion found the  $\beta$  phase precipitate of  $\text{Al}_2\text{Mg}_3$  to be extremely active (-1.15  $V_{SCE}$ ), and is an indication that the electrochemical activity of the phase that supports the selective dissolution based mechanism for IGSCC [13]. Searles' theory will be explored throughout this research for sensitized AA5083-H116, and the search for an opposing trend in laser peened materials will also be explored. Around approximately 200°C, Al-Mg alloys are thought to return to a solutionized  $\alpha$  structure with a reversal sensitization [25].

## C. CORROSION

### 1. Pourbaix Diagrams

The conventional understanding of SCC involves the periodic fracture of brittle oxide phases that form and reform at the root of a crack [1], [13], [24], [26], [27], [28]. Therefore, a thorough knowledge in the area describing the regions of passivity for the constituents of the Al-Mg alloy is essential for understanding the basics of stress corrosion cracking. Pourbaix describes the phase stability of an alloy in a corrosive environment as a function of applied electrochemical potential and solution pH [29]. We must thermodynamically analyze the corrosive and passive regions in both Al and Mg to provide a prediction of AA5083's behavior.

Aluminum has the tendency to form two types of passive films, both of which are brittle oxide films, in a pH range of  $3 < \text{pH} < 9$  [29]. Seawater and sodium chloride solutions exist in this range. In Figure 6, the two diagrams represent aluminum with an assumed passive layer film for hydrargillite and böhmite. The red line indicates the pH for this study (as is true for the following Pourbaix diagrams). In the first case, aluminum is predicted to form a hydrargillite film between the pH values of 4 to 9. At very acidic, or low, pH values of 4, the aluminum undergoes active dissolution at a trivalent aluminum cation; at alkaline pH with values greater than 9, the aluminum undergoes dissolution at an aluminate oxyanion [29]. In our case, the corrosive region for the pH we are evaluating appears to be böhmite.

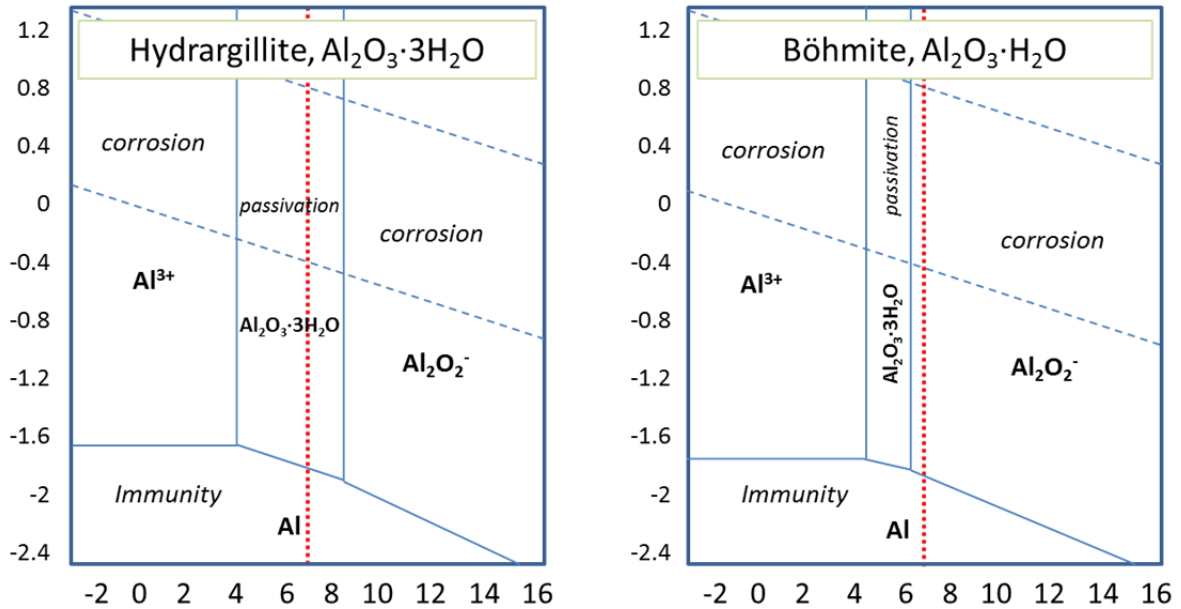


Figure 6. Marcel Pourbaix derived diagrams for pure aluminum and its common passive oxide layers: hydrargillite,  $\text{Al}_2\text{O}_3 \cdot 3\text{H}_2\text{O}$  (left) and böhmite,  $\text{Al}_2\text{O}_3 \cdot \text{H}_2\text{O}$  (right) at  $25^\circ\text{C}$  in solution. After *Atlas of Electrochemical Equilibria in Aqueous Solutions 1974* (From [29]).

It is also important to examine the Pourbaix diagram for Mg, since it significantly impacts the electrochemistry of an Al-Mg alloy. In a similar range of pH as pure Al, pure Mg forms magnesium hydroxide as a passive layer film for a pure metal. For pH values of 0 to 8 magnesium will corrode, while for a pH greater than 11, an oxide layer forms and does not overlap with the salt water and sodium chloride pH range [29]. By this alone, we see that Mg has no protective layer in the range of pH for salt water. The composite Al-Mg Pourbaix diagram is central in understanding why, for SCC in Al-Mg alloys, magnesium movement toward the grain boundaries may cause intergranular stress corrosion cracking by corroding the grain boundaries where the  $\beta$  phase exists, instead of passivating and protecting the alloy. Here, we see the region in which we are operating in is corrosive for magnesium.

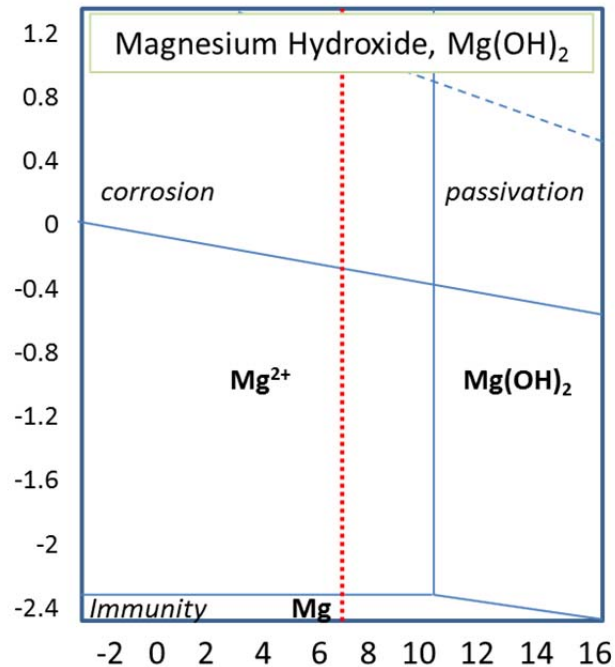


Figure 7. Pourbaix diagram for pure Mg and a common passive oxide layer, magnesium hydroxide,  $\text{Mg}(\text{OH})_2$  at  $25^\circ\text{C}$  in solution. After *Atlas of Electrochemical Equilibria in Aqueous Solutions 1974* (After [30]).

An attempt to overlay the Al and Mg Pourbaix diagrams can provide a rough estimate of the corrosive and passive regions in which we would see in reality of an Al-Mg alloy. Unfortunately, a diagram does not exist specifically for the  $\beta$  phase. However, this overlay shows the potentially corrosive region of both elements, and subsequently the  $\beta$  phase particles, as shown in Figure 8. Consequently, both combinations of the passive layer film formations show that the region in which this study is performed is, in fact, corrosive, but has a greater possibility of forming a passive layer film when assuming hydrargillite film for aluminum. Realistically, a third, more involved corrosion of specifically the  $\beta$  phase is most likely what is occurring in this research in the area of sensitized materials.

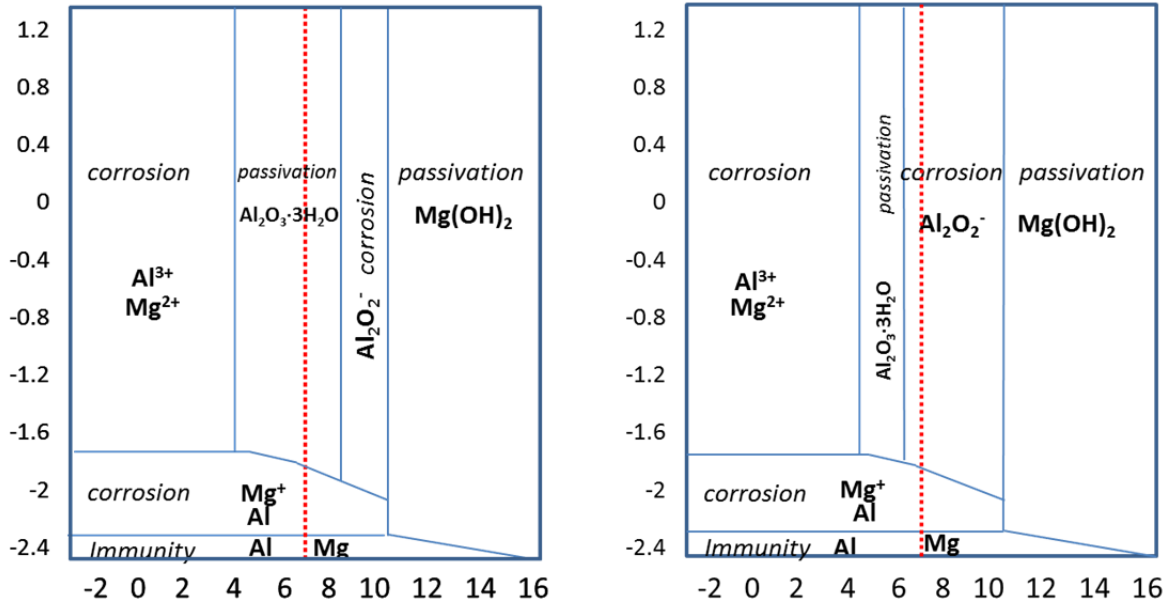


Figure 8. Al-Mg Pourbaix diagram overlay, specifically for the passive layers of hydrargillite,  $\text{Al}_2\text{O}_3 \cdot \text{H}_2\text{O}$  and  $\text{Mg}(\text{OH})_2$  (left), and böhmite,  $\text{Al}_2\text{O}_3 \cdot \text{H}_2\text{O}$  and  $\text{Mg}(\text{OH})_2$  (right) at  $25^\circ\text{C}$  in solution, modified individual images of aluminum and magnesium passive layer film formation. After *Atlas of Electrochemical Equilibria in Aqueous Solutions 1974* (After [31]).

Birbilis et al. did an extensive survey of the corrosion potentials, pitting potentials, and electrochemical characteristics for intermetallic particles commonly present in aluminum based alloys [12]. When AA5083-H116 corrodes freely in near neutral chloride solutions, the  $\beta$  phase is polarized above its breakdown potential, indicating that it will be selectively dissolved, as shown in Figure 9 [32]. They found that corrosion potentials and pitting potentials vary over a wide range for various intermetallics, and that the electrochemical behavior is more detailed than simple noble or active classification based on corrosion potential or estimated from intermetallic composition, like the method of Pourbaix diagram overlays [12]. The values of the breakdown potential for the  $\beta$  phase are much lower than for the alloy AA5083, and indicate that the  $\beta$  phase precipitate dissolves more vigorously at the corrosion potential of standard AA5083 in chloride solutions [12].

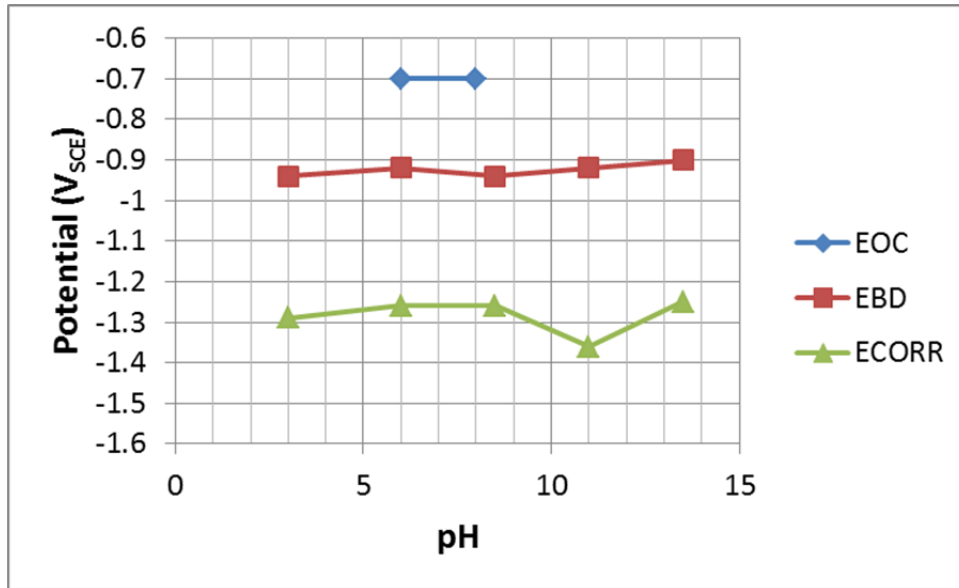


Figure 9. A summary of  $\beta$  phase polarization experiments in chloride solutions;  $E_{OC}$  is the open circuit potential,  $E_{BD}$  indicates the breakdown potential, and  $E_{CORR}$  indicates the corrosion potential. The AA5083-H116 corrodes freely in near-neutral chloride solutions; the  $\beta$  phase is polarized above its breakdown potential, indicating that it will be selectively dissolved. From *The electrochemistry of intermetallic particles and localized corrosion in Al alloys* (From [32]).

## 2. Types of Corrosion

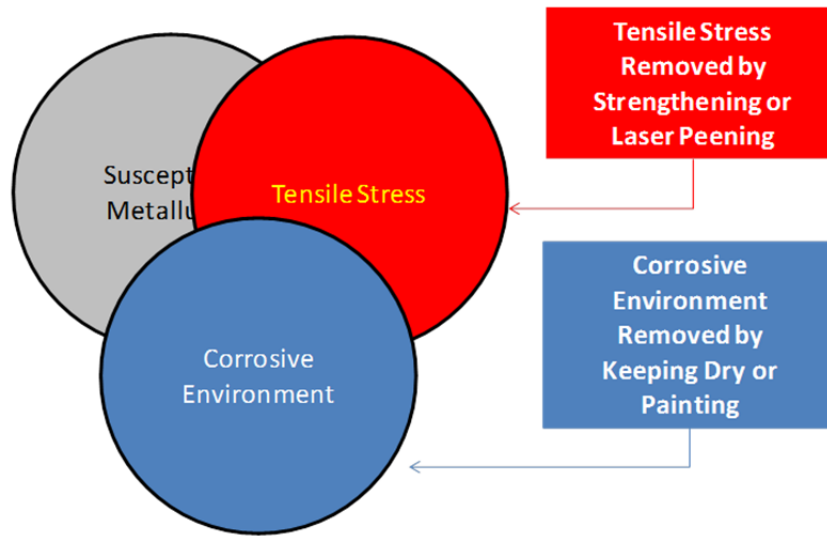
Several types of corrosion exist, to include pitting corrosion, crevice corrosion, IGC, SCC, and IGSCC. Each type of corrosion has a unique way of attacking the base metal, but some types require more external conditions than others. Pitting and crevice corrosion have specific mechanisms that differentiate them from other types of corrosion, but can help instigate or act as a catalyst in corrosion mechanisms related to SCC. Pitting is an extremely localized attack that result in holes or pits in the metal, and can be described as a cavity with the surface diameter about the same as or less than the depth. Unfortunately, it is one of the most destructive forms of corrosion as it causes equipment to fail because of perforation with a small percent of weight loss to the entire structure. It is also a catalyst to SCC and ICSCC. Pit initiation is generally believed to begin by rupture or breakdown of the passive film on a metal surface [12]. It is dependent upon the electrochemical stability of the passive layer film, and in the case of aluminum alloys, it

is influenced by the intermetallic particles that exhibit different surface film characteristics to the matrix, which may be either anodic or cathodic relative to the matrix [12]. Pitting many times becomes the initiation site for crevice corrosion, intergranular corrosion, and stress corrosion cracking.

Another form of corrosion commonly observed in aluminum alloys is crevice corrosion. Intensive localized corrosion frequently occurs within crevices and shielded areas on metal surfaces exposed to corrosives, and are usually associated with small volumes of stagnant solution caused by holes, plates, lap joints, surface deposits, gasket coverings, and crevices under bolts and rivets; it is also known as a deposit attack in which the deposit acts like a shield and creates a stagnant condition [1]. The mechanism for crevice corrosion can be visualized as the crevice acting as the anode and the free surface acting as the cathode.

IGC, SCC, and IGSCC are very closely related. IGC is important to understanding the mechanism affecting sensitized Al-Mg alloys. Grain boundaries tend to be more reactive in nature than the grain itself. Localized attack at or near grain boundaries is called intergranular corrosion. This concentrated attack causes the grains to fall out and ultimately disintegrates the alloy. This is a very common problem for Al-Mg alloys and is depicted in Figure 4, and can be further explained by SCC [1]. Three conditions must be met simultaneously in order for SCC to occur. A susceptible material must be present, the material must be exposed to a corrosive environment, and a tensile stress must be present on the material [33], [34]. Figure 10 is a schematic of the three factors influencing SCC, and indicates that without these three conditions, SCC will not occur.

### Three Factors Influencing SCC



### Removing Any of Three Factors Prevents SCC

Figure 10. Venn diagram representation of the three conditions required in coexistence to initiate and propagate SCC, along with preventative measures.

In regard to environments known to encourage SCC, electrolytes with halide anions cause SCC in many Fe- and Ni-based alloys, as well as in other alloy systems. SCC can initiate from a surface flaw, such as a corrosion pit or scratch, which can pre-exist due to poor manufacturing practices, or initiate at locations where high stress concentrations exist and serve as a stress riser, [33], [34]. The critical flaw size can be calculated from the threshold stress intensity factor for stress corrosion cracking. The propagation of SCC involves three stages, to include crack initiation or incubation, propagation, and failure. Fractures experienced during SCC are related to the formation of a brittle phase at the crack tip. Propagation occurs during the periodic rupture of this brittle phase. Since the brittle phase is an oxide that can be predicted with the corresponding Pourbaix diagrams, SCC can be correlated with specific combinations of pH and electric potential. Various crack propagation models exist, to include the film rupture model and the slip-dissolution-repassivation model. SCC is further accelerated with increased tensile stress, increased temperature, increased applied potential, increased halide anion concentration, increased levels of dissolved oxygen, and other pH factors.

For aluminum alloys, corrosive environments include NaCl-H<sub>2</sub>O<sub>2</sub> solutions, NaCl solutions, seawater, air, and water vapor [1]. For this study, we will examine NaCl solutions for aluminum alloy AA5083-H116.

Once initiated, a crack will grow by SCC when the applied stress intensity factor for mode I,  $K_I$ , is equal to or larger than the SCC resistance parameter,  $K_{ISCC}$ .  $K_{ISCC}$  is a material and environment dependent property, which can be obtained through fracture mechanics testing of the materials in the specified environment. SCC models require knowledge of the stress intensity factor  $K_I$  as a function of the corrosive environment. The stress intensity factor  $K_I$  is defined as a function of stress ( $\sigma$ ) and crack depth ( $a$ ), in which  $\beta$  is a factor dependent on the shape or geometry of the crack and the configuration of the structural component and  $\sigma$  is the tensile stress. In most cases of practical importance, closed-form solutions are not available for evaluating  $K_I$  since the stress  $\sigma$  may be non-uniformly distributed, and since the geometry factor  $\beta$  is a function of crack size.

$$K_I(a, \sigma) = \beta\sigma\sqrt{\pi a} \quad (1)$$

### 3. Prevention and Mitigation

SCC can be mitigated by removing one of the three factors. Preventative measures include removing the corrosive environment by painting or coating the metal to prevent exposure to the corrosive environment, or introducing inhibitor ions to induce galvanic corrosion. Another means of preventing include using a material not susceptible to SCC, like steel. Alcoa's mitigation specifications include the following requirements: material selection to prevent SCC includes choosing a plate with greater than 3% Mg, which must be certified to ASTM B928 standards, and if service temperatures exceed 65°C (150°F), an alloy with less than 3% Mg should be chosen [14]. Also, recent research has shown that removing residual stresses in areas experiencing corrosion fatigue can be achieved through shot peening or laser peening [28].

Improved forms of prevention include shot peening and laser peening, both of which attempt to eliminate the tensile stress applied to the aluminum alloy. Various levels of compressive stress can be introduced into a metal surface. The process of laser peening

involves the application of a high amplitude shock wave into a material surface using a high energy pulsed laser, thus achieving a cold working effect produced by the wave [35]. Laser peening increases the resistance of materials to surface-related failures, such as fatigue, fretting, and SCC, by creating a deep compressive residual surface stress [35]. This method has been conducted on titanium alloys, steel, aluminum alloys, and nickel based super alloys [35]. The laser peening process is shown conceptually in Figure 11.

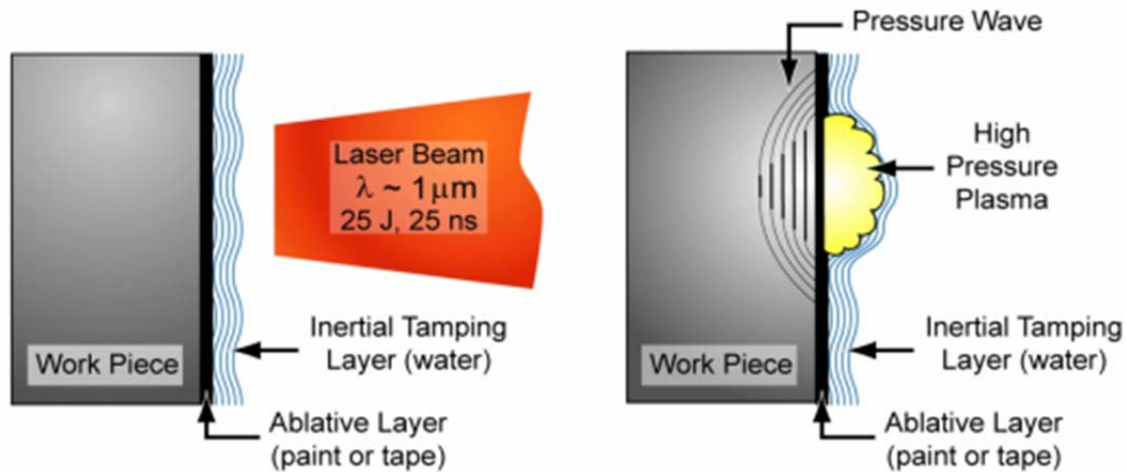


Figure 11. Graphical Representation of the Laser Peening Process.  
From *Production Laser Peening of High Strength Metals*,  
Metal Improvement Company (From [36]).

#### D. ELECTROCHEMISTRY OF THE AL-MG SYSTEM

Previous work done by recognized research in the field of corrosion science and material science prove to be a good baseline for the start of this research. Searles et al. used an anodic polarization scan with a stabilizing open circuit potential measurement to allow the system to stabilize [13]. The polarization tests were conducted in aerated and deaerated 3.5% NaCl solution at ambient temperature, and their samples were polished prior to testing [13]. The OCP of the  $\beta$  phase prepared in bulk was found to be very active (-1.15 V<sub>SCE</sub>) and is an indication that the electrochemical activity of the phase. The corrosion potential is very active, but the phase is spontaneously passive; passivity breaks down at -0.92V<sub>SCE</sub> (significantly lower than the pitting potential of standard AA5083, and

in agreement with research done by Birbilis et al. [12] [13]. They claim their polarization characteristics are reproducible in replicate experiments [13]. Since values of corrosion potential for AA5083 are given and much more positive than the breakdown potential for the  $\beta$  phase, the  $\beta$  precipitates will dissolve vigorously at the corrosion potential in chloride solutions for AA5083 [13].

On the contrary, Jain et al. discovered that the critical breakdown potential in 0.6M NaCl solution for AA5083 is most likely related to the spreading of IGC amongst  $\beta$  phase by a feedback process instead of isolating pitting in susceptible  $\beta$  phase sites [3]. They also found that at low nitric acid mass loss test (NAML) levels,  $\beta$  phase attack is random, whereas in the case of high NAML levels, a coordinated attack of proximate  $\beta$  phase particles exists [3]. IGC spreading occurs for highly sensitized conditions only because of a larger network of nearly continuous  $\beta$  phase covered grain boundaries in close radial proximity, which can be seen for NAML values of 49 mg/cm<sup>2</sup> [3]. According to Jain et al., a sharp difference in the local corrosion rate is observed at an applied potential above the threshold; also, at increasing molarity of NaCl, a lower applied potential increases the probability of spreading of IGC [3]. They find that the difference in breakdown potentials of non-sensitized AA5083 and anodically active  $\beta$  phase in 0.6 M NaCl solutions is nearly 200 mV;  $\beta$  phase preferentially precipitates along some grain boundaries after thermal exposure which makes them more active than the alloy matrix [3]. Highly sensitized alloys exhibit higher anodic currents, which they found in both anodic polarization curves and potentiostatic experiments [3].

## **1. Basic Electrochemical Reactions of the Al-Mg System**

In the case of a pit initiation at a discrete susceptible site on a grain boundary in an Al-Mg alloy, Mg<sup>2+</sup>, Al<sup>3+</sup>, and H<sup>+</sup> cations generate during the process and accumulate inside and over the pit [3]. Cl<sup>-</sup> and H<sup>+</sup> ions damage the surface surrounding the  $\beta$  phase precipitates, which results in a significant drop in the breakdown potential for sensitized conditions [3]. Figure 12 shows their dramatic shift in breakdown potential. In this study, we hope to confirm this understanding of the effects of sensitization on AA5083, and expand upon the research in a way that proves laser peening has the

opposite effect. We must assume the basics of tafel kinetics, and that Butler-Volmer kinetics must apply.

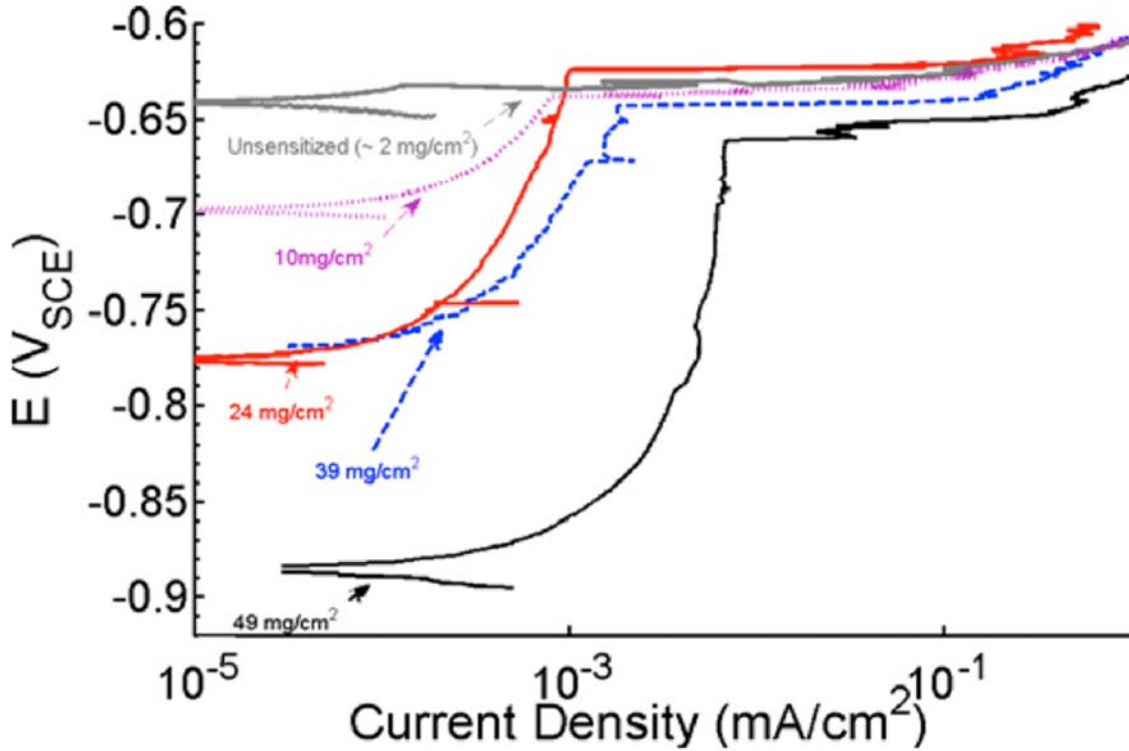
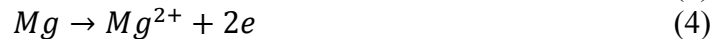


Figure 12. E-log(i) polarization curve for AA5083-H131 on the L-T plane as a function of sensitization. From *Spreading of intergranular corrosion on the surface of sensitized Al-4.4Mg alloys: A general finding* (From [3]).

Aluminum and NaCl release  $H_2$ . Here we see electron production and consumption by the most basic principles of corrosion. For metals, the rate of oxidation is equal to the rate of production [1]. The general form for an anodic reaction, which is the anodic dissolution of a metal to an ion, is as follows [1].



For Al-Mg alloys, the corresponding anodic dissolution reactions are:

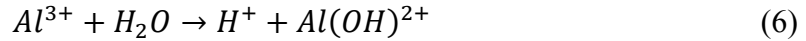


As seen from the Pourbaix diagram, the anodic dissolution for aluminum occurs at a pH below 3, but for magnesium, occurs at a pH between 0 and 8. The anodic

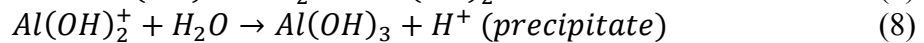
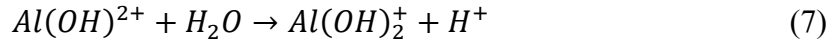
oxidation of aluminum at near-neutral pH ( $6.5 < \text{pH} < 7.5$ ), results in the formation of the aluminum oxide film, hydrargillite, or  $\text{Al}_2\text{O}_3$  (Figure 6). Since water and seawater are neutral, and the medium is exposed to the atmosphere, it contains dissolved oxygen, and listed below are the cathodic reactions that are expected. It is important to understand the formation of the aluminum oxide and its chemistry. Since seawater and sodium chloride solution are neutral in nature, and the medium is exposed to an air saturated atmosphere in most naval applications, it contains dissolved oxygen and the following cathodic reduction reaction is expected, as the solution is neutral to slightly alkaline:



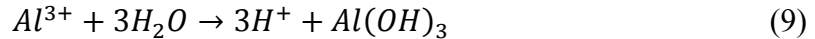
Anodic dissolution of the aluminum alloy undergoes hydrolysis:



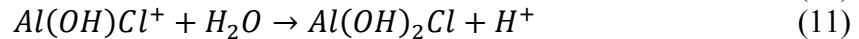
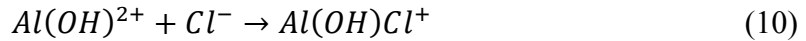
The hydrolysis reaction produces hydrogen cations, which acidify the local environment. For the case of trivalent aluminum, three protons are generated before precipitation occurs.



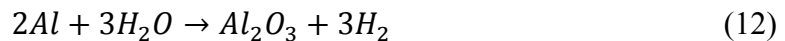
The overall reaction is then:



The aluminum hydroxy ions may complex with chloride anions, as illustrated with divalent species:



In addition to forming a film of aluminum hydroxide as shown in the above reaction, it is also possible to form a film of aluminum oxide. The overall reaction for passivation consistent with the electrochemical reactions shown by Pourbaix in Figure 7 is:

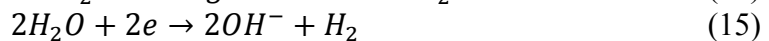


The  $\text{Al}_2\text{O}_3$  can be hydrated as shown by Pourbaix, forming  $\text{Al}_2\text{O}_3 \cdot \text{H}_2\text{O}$  and  $\text{Al}_2\text{O}_3 \cdot 3\text{H}_2\text{O}$ .

The anodic dissolution of magnesium produces Mg ions and is a rate determining factor when studying magnesium as a pure, or primary, metal:



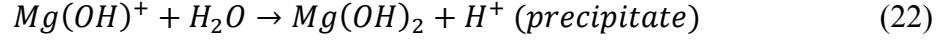
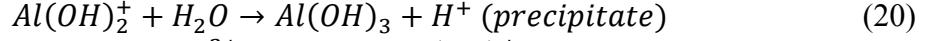
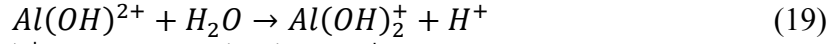
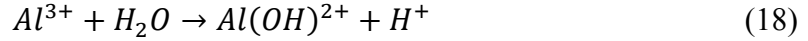
Chemical hydrogen evolution reaction, leading to the corrosion reaction consistent with the electrochemical reactions shown by Pourbaix in Figure 7 is:



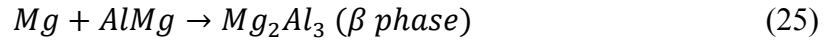
The anodic dissolution reaction is:



The hydrolysis reactions of dissolved metal cations is:



Few literary articles are available on the specific topic of  $\beta$  phase oxide layers, but the formation of  $\beta$  phase particles and its oxide layer are addressed thoroughly in works by Anders Andreasen [37]. Based on diffraction mechanism techniques, the theory suggests that the dehydrogenation of  $MgH_2$  forms the following basic system, to form the  $\beta$  phase particles in hydrogen:



Because oxygen exists in the scope of this thesis, for the  $\beta$  phase particles, we expect to possibly see a thermally formed oxide layer that some predict are  $Al_2O_3$ ,  $MgAl_2O_4$  (spinel), or a combination of both, with  $Al_2O_3$  dominating the formation of passive layer oxides [37], [38].

## 2. Cyclic Polarization and Electrical Impedance Spectroscopy

Cyclic Potentiodynamic polarization (CP) and electrochemical impedance spectroscopy (EIS) are two electrochemical methods used to measure several factors in charge transfer kinetics and to assess various environmental and corrosive effects on metals. Particularly, for aluminum, studies have been performed to evaluate residual stresses, sensitization, and other aspects. Figures 13 and 14 are generalized schematics of the resistor capacitor circuit representation,  $\alpha$  and  $\beta$  phase oxide layer surface area and thickness, and cation and anion movement through the oxide layer, respectively. We do not expect to see the same behavior in the samples that are sensitized as we expect for the control samples, nor do we expect the same behavior for bent samples. The control samples only exhibit behavior presented by  $\alpha$  phase in response to the 0.6M NaCl aqueous solution. We expect the sensitized samples, however, exhibit behavior of a combination of  $\alpha$  and  $\beta$  phase response.

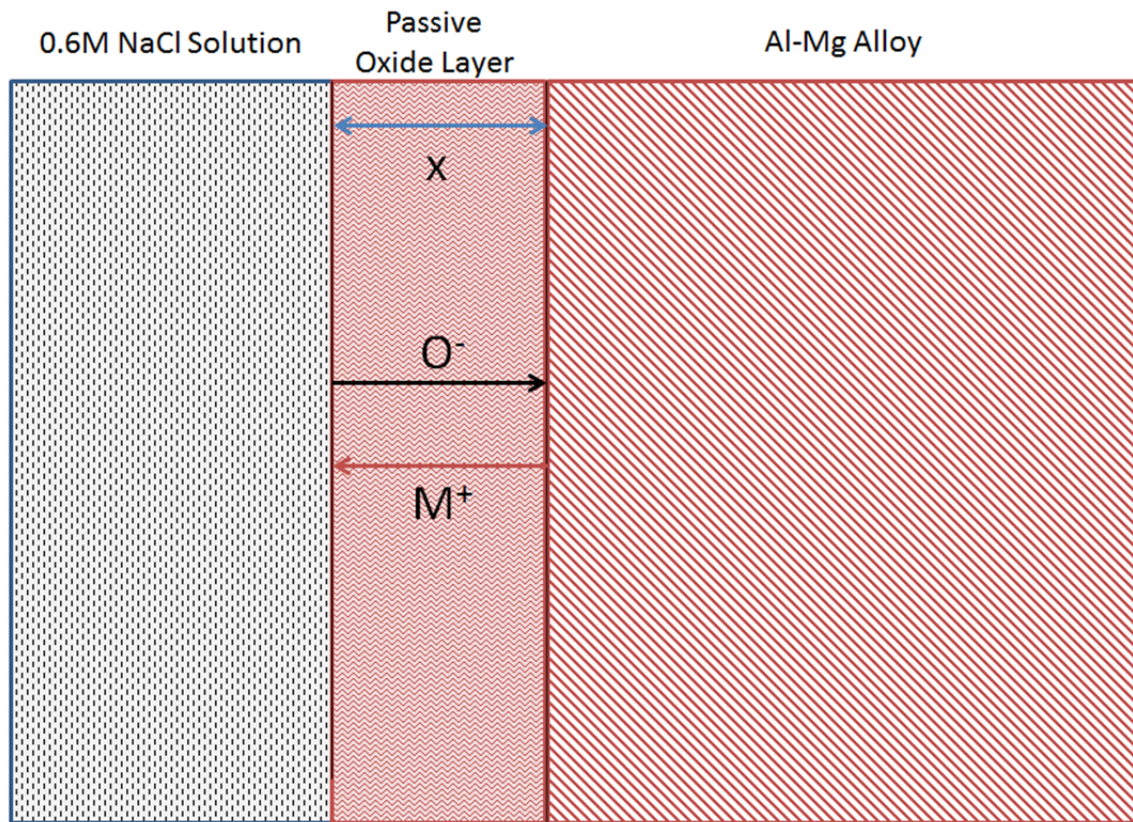


Figure 13. Schematic of  $\alpha$  and  $\beta$  phase surface area and passive oxide layer thickness, representing the movement of cations and anions through the passive layer film. “X” represents the film thickness, O<sup>-</sup> represents the movement of oxygen cations, and M<sup>+</sup> represents the movement of metal anions.

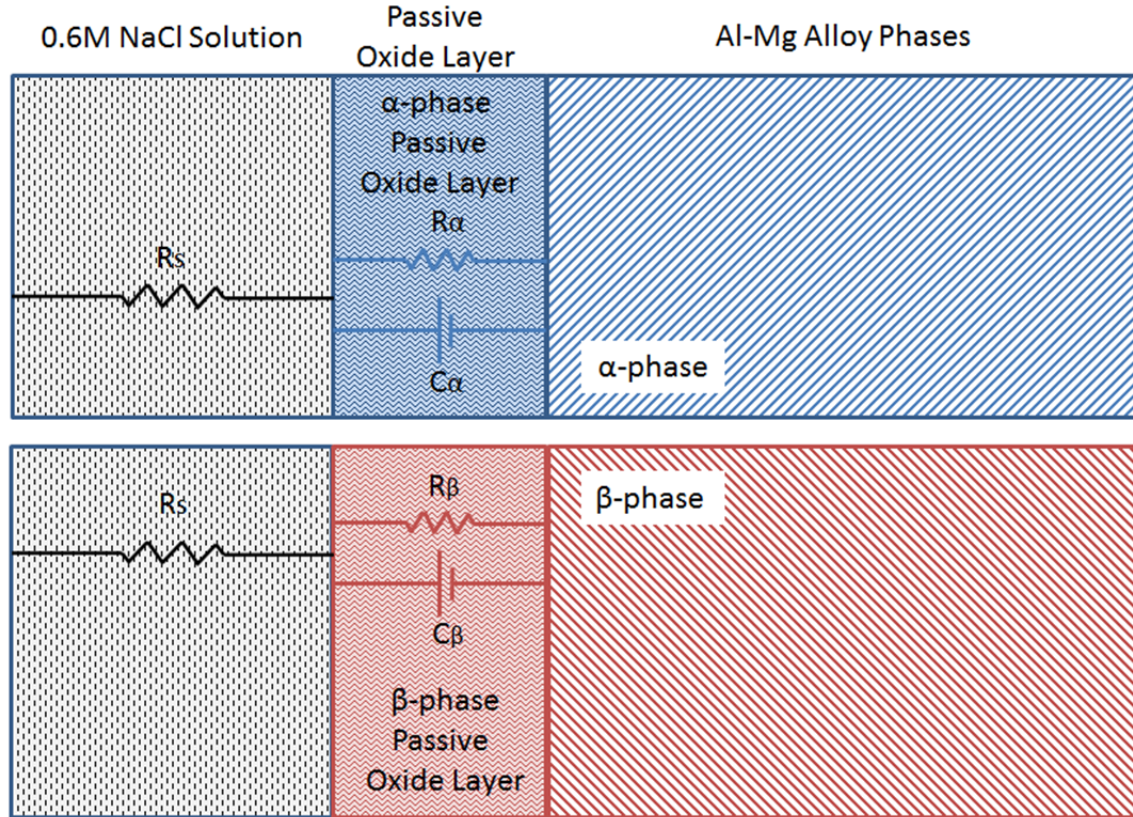


Figure 14. Schematic of an Al-Mg alloy's sensitized components in 0.6M NaCl Solution, represented by  $\alpha$  (above) and  $\beta$  (below) phase passive oxide layer resistor capacitor circuit setup.

We can quantify the sensitization effects by simple methods from resistors and capacitors:

$$R_{\beta} = \frac{c_{\beta} d_{\beta}}{A_{\beta}} \quad (26)$$

$$\frac{1}{R_{oxide}} = \frac{1}{R_{\alpha}} + \frac{1}{R_{\beta}} \quad (27)$$

We expect laser peened samples to enhance passive layer film resistance.

Spontaneous breakdown of the passive film and localized corrosion require that the open-circuit corrosion potential exceed the critical potential:

$$E_{CORR} \geq E_{CRIT} \quad (28)$$

$E_{CORR}$  is the corrosion potential, while the breakdown or critical potential are represented interchangeably by  $E_{BD}$  or  $E_{CRIT}$ . The repassivation potential, or  $E_{RP}$ , is where the material begins to repassivate. Using the CP curve data enabled comparison between the samples'  $\Delta E_{RP}$ ,  $\Delta E_{CRIT}$ ,  $E_{CORR}$ , and passivation current density ( $i_p$ ). By

comparing the data obtained in these curves and data points, one can determine if a physical application (such as sensitization) drives a certain parameter (such as  $E_{CORR}$ ) up or down. This shift is important in understanding electrochemical effects that applied conditions have on the Al-Mg alloy. Figure 15 is an example of the response expected from Al-Mg alloys, and shows a very distinct  $E_{CORR}$ ,  $i_{CORR}$  (corrosive current density)  $E_{CRIT}$ ,  $i_p$ , and  $E_{RP}$ . It very clearly shows a cathodic reduction of the material until it reaches  $E_{CORR}$ , where the material experiences an anodic oxidation reaction. The potential reaches the critical potential in which the passive oxide layer film breaks down. The voltage drives the material to respond in the form of what is known as a positive hysteresis loop in which the material depends on its current and past environment, associated with an irreversible thermodynamic change. Figure 15 shows a different expected result if a mill oxide layer is present. A mill oxide layer exists, impeding the expected performance of AA5083-H116 material response and does not illustrate the breakdown potential. These two figures show very different responses for the same material.

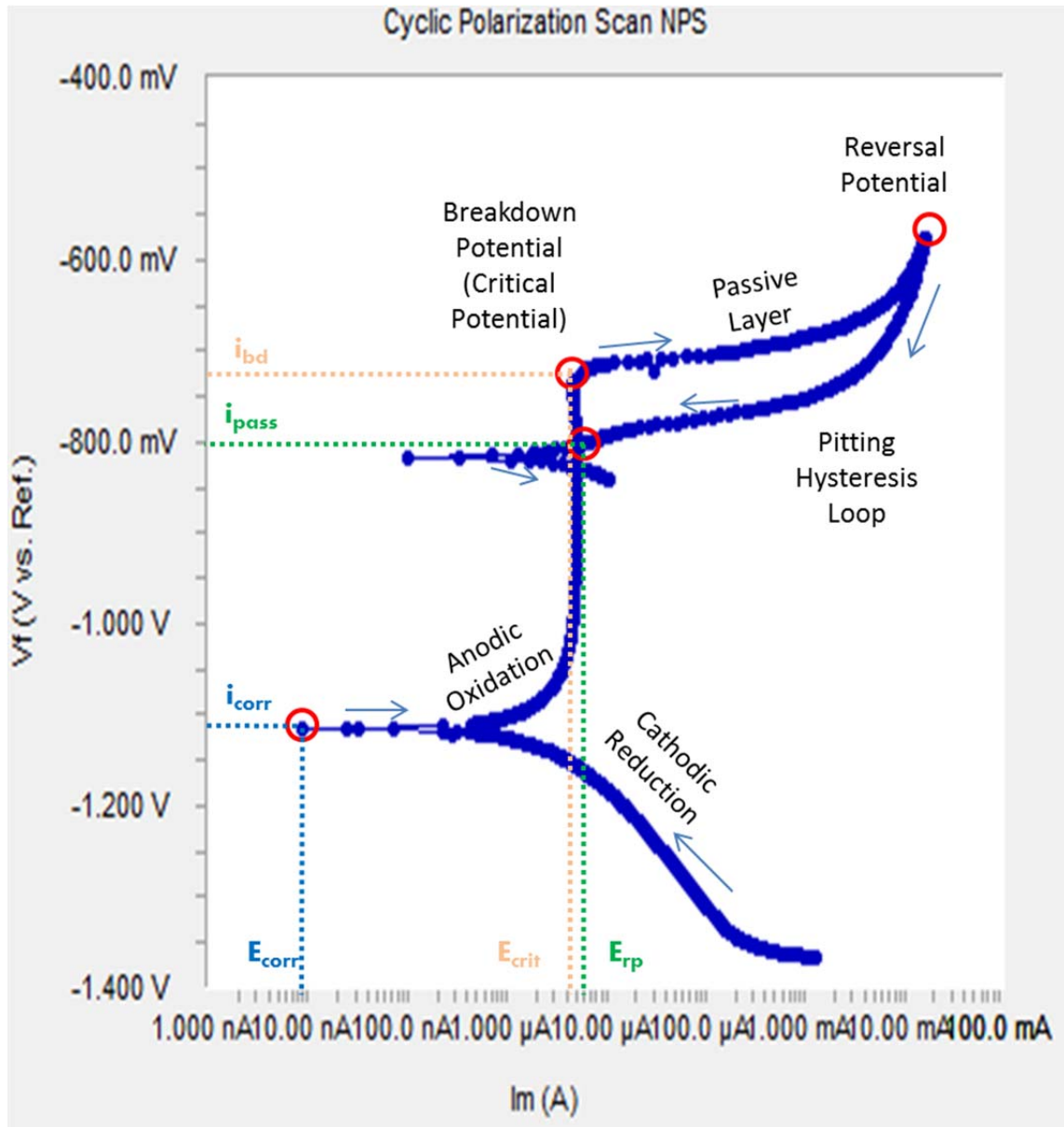


Figure 15. Example of a cyclic polarization scan of AA5083-H116, showing cathodic reduction, anodic oxidation, and pitting hysteresis loop without passive layer Film breakdown, for scan 2 of sample 19.

The resistance to localized corrosion is quantified through measurement of the  $E_{OC}$  or  $E_{CORR}$ ,  $E_{CRIT}$  or  $E_{BD}$ , and,  $E_{RP}$ . The greater the difference between the open-circuit corrosion potential and the repassivation potential,  $\Delta E_{RP}$ , the more resistant a material is to modes of localized corrosion such as pitting and crevice corrosion. In integrated corrosion models, general corrosion is invoked when  $E_{CORR}$  is less than  $E_{CRIT}$ , and

localized corrosion is invoked when  $E_{CORR}$  exceeds  $E_{CRIT}$  [39]. The data provided in this publication are sufficient to establish when general and localized corrosion occur, and the rates of general corrosion are when general corrosion is invoked. Note that these data only apply for the environments explored during testing. CP is used as a means of measuring the  $E_{CRIT}$  of corrosion resistant materials, relative to  $E_{CORR}$ . In the published scientific literature, different bases exist for determining the critical potential from electrochemical measurements. The critical potential is frequently defined as the point where the passive current density increases during the forward (anodic) scan to a level between 1 to 10  $\mu\text{A}/\text{cm}^2$  ( $10^{-6}$  to  $10^{-5}$   $\text{A}/\text{cm}^2$ ). Alternative definitions of the repassivation potential are used. One definition is the point during the reverse (cathodic) scan where the current density drops to a level indicative of passivity, which is *assumed* to be between 0.1 to 1  $\mu\text{A}/\text{cm}^2$  ( $10^{-6}$  to  $10^{-7}$   $\text{A}/\text{cm}^2$ ). An alternative definition is the point where the forward and reverse scans intersect, a point where the current density being measured during the reverse scan drops to a level *known* to be indicative of passivity. In this study, we will use the point where the forward and reverse scans intersect and are known, as shown in Figure 15. Definitions of the threshold and repassivation potentials vary from investigator to investigator. Gruss et al. define the repassivation potential as the point where the current density drops to  $10^{-6}$  to  $10^{-7}$   $\text{A}/\text{cm}^2$  [40]. Scully et al. define the threshold potential for crevice corrosion of Alloy C-22 as the point during the scan of electrochemical potential in the forward direction where the current density increases to a level of  $10^{-6}$  to  $10^{-5}$   $\text{A}/\text{cm}^2$  [3]. Using a current density criterion for repassivation of  $10^{-5}$   $\text{A}/\text{cm}^2$ , repassivation potentials were determined to be slightly above, but relatively close to the open-circuit corrosion potential [3]. The chloride anion promotes passive film breakdown, while the nitrate serves as an inhibitor. The potential is scanned in the positive (anodic) direction from a level slightly more negative than the corrosion potential (cathodic limit), to a reversal potential ( $E_{REV}$ ) near that required for oxygen evolution (anodic level). During the positive scan, anodic oxidation peaks may be observed that have been correlated with the oxidation at the alloy surface of the passive layer film, as well as current excursions that are usually associated with breakdown of the passive film. During the negative (cathodic) scan, a hysteresis loop will be observed in

cases where passivity has been lost. As the scan continues, the current density may eventually decrease to a level equivalent to that experienced during the positive scan, and indicative of reformation of the passive film. The potential at which this occurs is known as the repassivation potential, or  $E_{RP}$ . Numerical corrections for the reference electrode junction potential have been estimated, and have been found to be insignificant [27].

The determination of passive film characteristics is valuable and can be found with EIS. EIS has been used to investigate the integrity of the passive film formed on aluminum. The surfaces of some samples in this experiment are completely modified by laser peening. Increases and decreases in the amplitude of the complex impedance at low frequency (below 1,000 Hz) are correlated with increased modification of the surface by laser peening, which appears to cause the formation of a passive film with finer oxide crystallites, thereby increasing the resistance of the passive film, along with the corrosion resistance. The EIS data obtained in this thesis attempts to show unambiguously that LP can improve the passivity and corrosion resistance of complex Al-Mg alloys. A more complete understanding of the large changes in the EIS data with laser peening modification requires the development of mathematical models, which will be discussed in forthcoming sections of the paper.

Several studies have encompassed a wide range of the corrosion of metals and the study of the oxide layer film breakdown [39]. Many models are represented in their complexity, and research has found that a relatively simple impedance model that is conceptually consistent with SEM observations of the interface is capable of fitting the EIS data very well, with parameters reflecting changes in passivity as samples transition from the as received condition to the laser peened state. From research, we know that the passive film formed on different materials, such as as-received Ni-Al bronze alloys, consist of at least two distinct types, with each type covering a specific metallurgical phase in the underlying polycrystalline alloy. The morphology of the surface suggests discrete regions covered with different types of oxide, in which we can hypothesize is the same for Al-Mg alloys.

A potentiostat is fully equipped to apply the necessary potential and measure the resulting current. With three electrodes, data can be obtained for various metals in

various solutions for both CP and EIS. First, a corroding material, or working electrode to be evaluated as the material of interest, acts as the working electrode (WE). Next, a counter electrode (CE) is needed from an inert material, like graphite or platinum. Finally, a stable reference electrode (RE) is needed. Figure 16 is a schematic of a potentiostat with the abovementioned electrodes required.

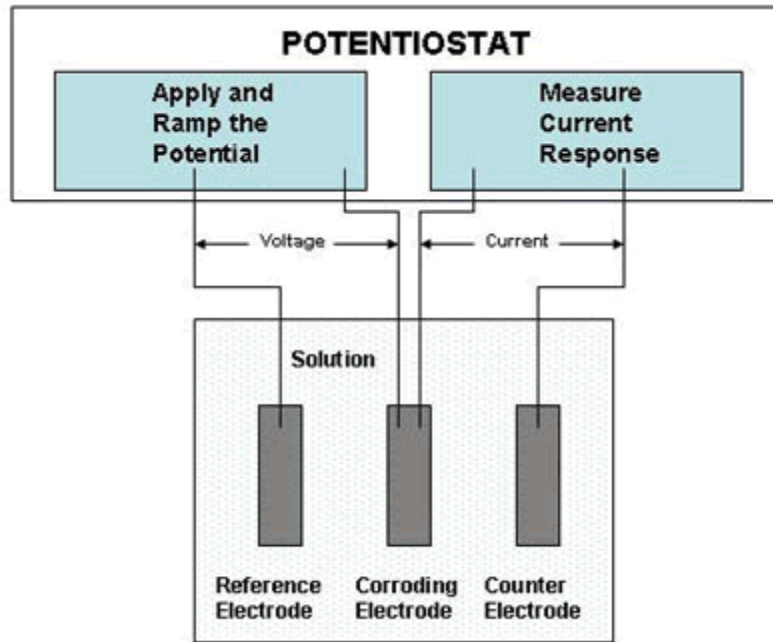


Figure 16. Basic equipment overview and set-up for CP and EIS data collection. From *Cyclic Potentiodynamic Polarization Scans* (From [41]).

Cyclic Potentiodynamic Polarization scan, or CP scan, techniques screen alloys in terms of their risk of suffering localized corrosion in the form of pitting or crevice corrosion. A CP scan consists of a measurement of an induced voltage and frequency, and quite simple in nature. A computer controls the rates and increase/decrease of electric potential, and reads current measurements. The technique for a CP scan forces a material to leave its steady-state corrosion rate to at a constant voltage scan rate and observes how the current responds as the voltage force is applied and removed at a constant voltage scan rate. The material under observation is AA5083-H116 aluminum alloy, and the corrosive environment is 0.6M NaCl, which promotes corrosion in a neutral and natural environment that imitates the environment at sea. The applied electric potential is the

force. CP scans compare electric potential against a logarithmic plot of current. Some sources plot Volts in the x-direction and Current Density ( $\mu\text{A}/\text{cm}^2$ ) in the y-direction; others plot current density in the x-direction and volts in the y-direction. Regardless, both ways of displaying these plots read similarly and are interpreted similarly. Some scans will display voltage in reference to the type of electrode used. Most commonly seen is  $V_{\text{SCE}}$ , but this experiment is using a silver/silver-chloride reference electrode. The electric potential is ramped at a continuous slow rate and compared relative to a reference electrode using a potentiostat. The forward scan is increased first at a constant rate in the anodic direction. At a chosen voltage, the scan is reversed in the opposing direction at a maximum current or voltage. At this point, the scan is reversed and progresses at the same rate in the cathodic or active direction. Finally the scan is terminated at another chosen voltage, typically the starting corrosion potential or some voltage active with respect to the corrosion potential. Interpretation of CP scans can prove to be challenging. Several features are used for interpretation, to include pitting potential, corrosion potential, breakdown potential, repassivation potential, positive hysteresis loops between forward and reverse portions of the scan, and the associated current densities near corrosion potential.

### **3. Basic Resistor-Capacitor Model**

Electrochemical impedance spectroscopy, also known as AC impedance, is a computer controlled laboratory based technique and models corrosion systems. A low amplitude alternating current or electric potential wave is imposed of a DC potential (the corrosion potential with zero imposed current). The frequency is varied from 10 mHz to 1 MHz in one experiment with 5–10 steps per decade of frequency. Corrosion usually drives the measured current to be out of phase with the input voltage; by dividing the input voltage by the output current furnishes the impedance, and the variation of impedance is what is used for interpretation. EIS is the frequency dependent, complex valued proportionality factor between the applied potential or current and the response current or potential in an electrochemical cell, which becomes the impedance when the perturbation and response are related linearly. The goal is to measure impedances as a function of frequency and analyze the resulting spectrum to estimate corrosion rates and

mechanisms that might give rise to the spectra [42], [43], [44]. The approach of using EIS is that the corrosion of alloys and other related conductive materials is a basic electrochemical degradation process governed by kinetics and thermodynamics. The chemistry is often difficult to interpret in complex and poorly characterized systems that are encountered in daily situations, such as shipbuilding and operation at sea. Analogous circuit elements enable the corrosion practitioner to bridge gaps in knowledge, which enables the use of EIS to estimate the corrosion rates and corrosion mechanisms in these systems. Application of this technique is used in areas estimating corrosion rates, estimating corrosion inhibitor functionality, and examining coatings on metal surfaces. It is also used in battery research. Here, we will be using this method to estimate the resistances of the passive layer oxide of the same material under different conditions. Specific circuit elements are used to represent an electrochemical cell setup. Basic elements include a resistor, capacitor, and inductor. A basic R/C model can easily represent the electrochemical cell and electron movement, but it is important to remember that a model cannot identically predict every component involving moving ions and molecules. Passive alloys, like aluminum in salt water, can be modeled by Figure 17 as a parallel combination of a resistor and capacitor in series, along with another resistor that models the solution resistance.  $R_p$  provides a value for polarization resistance, which theoretically should be inversely proportional to the corrosion rate. The capacitor provides a value for the capacitance that exists across the interface between the alloy and the environment. Aluminum alloys tend to be very passive and corrosion resistant as mentioned earlier, and thus have a passive oxide layer or a mill oxide layer, with higher resistances on the first scan when not polished.

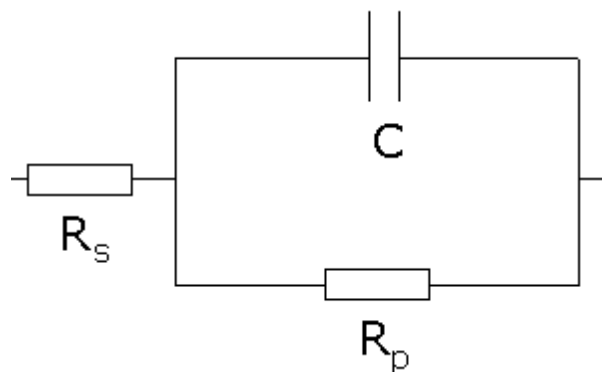


Figure 17. Basic R/C Circuit Model Set-Up for EIS. From *Cyclic Potentiodynamic Polarization Scans* (From [41]).

The Bode and Nyquist plots are very similar in the data represented; they are plots of similar information in different formats. The Bode plot shows the impedance magnitude and phase angle against the frequency, while the Nyquist plot represents real and imaginary parts. A basic impedance model is given in Chapter II and discussed in greater detail in Figure 31. Multiple RC (parallel combinations of R and C) time constants may not have 1:1 correspondence to corrosion process. Possible interference may be the distributed processes on the surface (e.g., transmission line), the diffusion process between the surface and bulk fluid, and additional surface reactions affected at low frequency. Electrochemical cell geometry and electrode placement also have a large effect on the results. Heterogeneously distributed surface reactions, surface roughness and scratches also play a large role. Some are a result of poor experimental design and others are a part of the physics of the system that cannot be avoided. A method to account for some of the influences is by using the constant phase element in place of capacitance. As previously discussed, the circuit elements made to model electrochemical impedance spectra are combinations of resistances, capacitances, and inductors. Fitting was done with a simplex-type optimization program that determined model parameters by seeking out the minimum in the sum-of-squares surface (minimum in error between prediction and observation). Supporting discussions of EIS and its application can be found in the published literature [45], [46]. The following equations are the impedance equations for the elements [47]:

$$\text{Resistor: } Z = R \tag{29}$$

$$\text{Capacitor: } Z = -\frac{1}{j\omega C} \quad (30)$$

$$\text{Inductor: } Z = j\omega L \quad (31)$$

Using the same RC circuit as in Figure 18, we can model by the following equation for overall impedance,  $Z$ :

$$Z = R_s + \frac{1}{\left(\frac{1}{R_p} - j\omega C\right)} \quad (32)$$

The goal for building a circuit is to curve fit the circuit data to the measured spectra and a good fit is interpreted as a good model. For the work presented, a basic RC circuit is used.

The Bode format plot data is given by the following equation:

$$(Z - R_s) = \frac{R_p^2}{1 + \omega^2 R_p^2 C^2} \quad (33)$$

For Nyquist format data, which is the same information as the Bode plot but represented differently,

$$Z - R_s = \frac{R_p}{1 + \omega^2 R_p^2 C^2} + \frac{j\omega R_p^2 C}{1 + \omega^2 R_p^2 C^2} \quad (34)$$

To fit experimental Bode and Nyquist plot data from the EIS scans to fit an RC circuit model, we use the Simplex Method modeling tool in Echem Analyst™. This method calculates errors between model and data.  $R_1$  represents the solution resistance, or  $R_s$ .  $R_2$  represents the *modeled* surface resistance and models aluminum oxide film and is denoted by  $R_{P2}$  ( $R_{P1}$  is the *experimental* value directly from the Bode plot). It is also known as the charge transfer resistance in tafel kinetics.  $C_3$  represents the oxide film capacitance and double layer capacitance, which is much less than one. Using the Simplex Method in Echem Analyst™, a simple R/C circuit is used to model the solution resistance and passive layer film polarization resistance. Figure 18 is the model used for these series of experiments, while Figure 19 shows an example of the output results for the model fit editor.

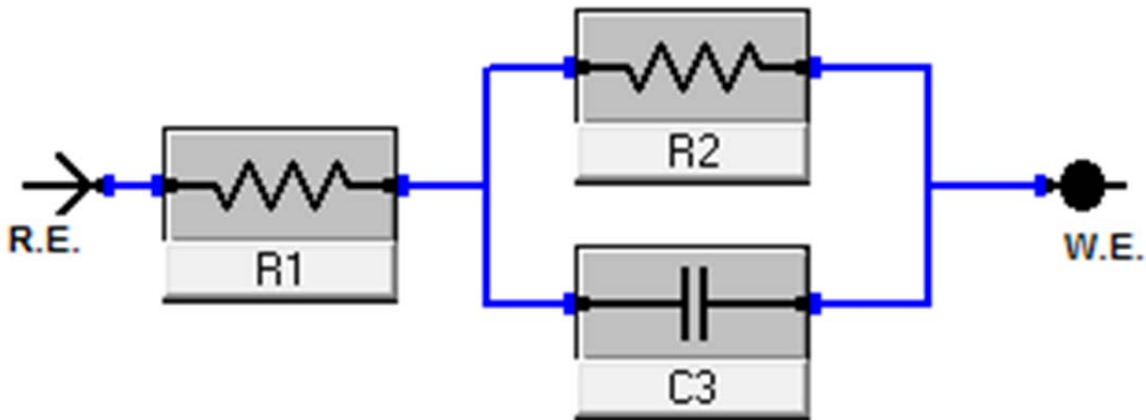


Figure 18. Impedance Model Editor: R/C circuit for AA5083-H116. R1 is the solution resistance, R2 is the polarization resistance, and C3 is the equivalent capacitance.

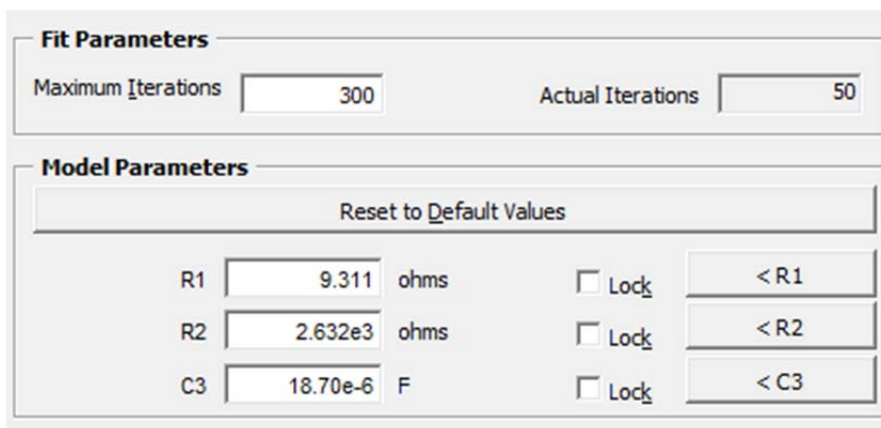


Figure 19. An example of the Simplex Method impedance fit output provided by Echem Analyst™. Data for sample 28, scan 2.

A predetermined potential discussed earlier on the equipment is used to drive corrosion. The cell is set up as an air-saturated or aerated cell, as the solution is continuously exposed to air, but not circulated or bubbled. Additional controls for aerating the solution or controlling the temperature were not used in this experiment. Figure 38 is an example of the electrochemical cell setup and Figure 39 shows the cell setup on a bend rig.

## **E. OBJECTIVES**

The purpose of this thesis is to determine the role of mechanical stress on the electrochemistry of corrosion for AA5083-H116. The stresses are imposed by laser peening (a compressive stress accompanied by plastic deformation) and by purely elastic, tension through four-point bending. While previous work has examined the effects of grain boundary sensitization on corrosion and stress corrosion cracking of Al-Mg alloys, the direct effects of mechanical stress, specifically laser peening, on the corrosion chemistry, itself, have been minimally addressed. The ultimate goal is to assess the possible roles that mechanical stress might play in either causing stress corrosion cracking (residual stresses from welding) or in mitigating stress corrosion cracking (peening processes such laser peening).

### **1. Confirm Effects of Sensitization on Electrochemistry of Corrosion for AA5083-H116**

We will use cyclic polarization (CP) and electrochemical impedance spectroscopy (EIS) to measure the change in corrosion electrochemistry as a function of grain boundary sensitization level. These measurements will replicate and build upon similar studies in the literature and will provide a baseline for assessing the effects of stress on corrosion chemistry.

### **2. Assess the Effects of Elastic Stress on Electrochemistry of Corrosion for AA5083-H116**

We will assess the effects of elastic stress on the electrochemistry of corrosion for AA5083-H116. These measurements will require the development a miniature electrochemical cell that can be applied to the surface of a corrosion specimen. This miniature cell will then be used to measure the cyclic polarization and EIS responses of the surface of AA5083-H116 specimens in a four-point pending apparatus. The corrosion responses will be measured while the sample is subjected to pure, elastic tension.

**3. Assess the Effects of Laser Peening on Electrochemistry of Corrosion for AA5083-H116**

We will assess the effects of laser peening on the electrochemistry of corrosion for AA5083-H116. The same miniature electrochemical cell will be applied to the surfaces laser peened specimens. The laser peening will be varied by controlling the irradiance, the pulse width, and the number of passes. The corrosion responses will be measured to determine the effects of compressive residual stress and work hardening on the corrosion response.

THIS PAGE INTENTIONALLY LEFT BLANK

## II. EXPERIMENTAL METHODS

### A. MATERIAL PROCESSING: FABRICATION AND APPLIED STRESSES OF TEST SAMPLES

Each sample used was aluminum alloy AA5083 with H116 heat treatment and of the following composition: Mg 4.7, Mn 0.9, Fe 0.20, Si 0.10, Cr 0.08, Zn 0.03, Cu 0.03, and Ti 0 as certified by the American Bureau of Shipping [28]. Aluminum samples used for the control samples, sensitized samples, and bending samples originated from the same batch of aluminum alloy. Each sample was cut by a band saw from a larger plate, and had the following dimensional parameters: 25.4mm (2in) wide, 139.7 mm (5.5in) long and 0.28 mm (0.011 in.) thick. The control samples did not have any sensitization, laser peening, or bending applied to them. The laser peened samples originated from a separate batch of material, and thus have a different control sample for consistency in the event that there is a difference in composition or impurities in manufacturing between batches.

### B. SAMPLE DISTRIBUTION AND SET-UP

Each sample had different applied conditions. Sample numbers and their conditions are listed in the Appendix, Table 7.

#### 1. Sensitized Batch

##### *a. Control – Bend and Laser Peened Samples*

The control samples were simple plates cut from a stock of plate material. Two samples are done for consistency. Sample 1 was evaluated in the transverse direction, or “T” direction, and sample 2 in the rolling direction, or “L” direction. Theoretically, there should be no difference in the electrochemistry of these samples, as there are no other physical differences between them. Duplicate scans of both samples were conducted for statistical analysis.

***b. Bend Samples***

Two samples without laser peening, friction stir welding, or sensitization were evaluated on a bend apparatus. The four point bending apparatus was made of 316 stainless-steel, which has a much higher elastic modulus and corrosion resistant capability that enabled the electrochemical experiments to be run without contaminating the results, and bent the aluminum to 50% of the ultimate yield strength in a manner that would not bend the steel. The apparatus was designed in accordance with ASTM-G39, using #10 stainless steel screws with 32 threads per inch. Samples were put into the bend rig, with the exposed side of the sample in tension.

Each sample was exposed to an applied stress by the bend apparatus of 150 MPa (21.8 ksi). Figure 20 shows the ASTM-G39 standard for setting up a four-point bend sample. Figure 21 show the dimensions of the bend rig built by students at the Naval Postgraduate School in Monterey, CA, which adhere to the ASTM-G39 standards. Figure 22 shows the applied stress based on the number of screw turns in the bend apparatus; the green line correlates to approximately 150 MPa (21.8 ksi) and is desired, which is approximately 1.6 turns as noted by the red line. Sample 3 was cut in such a way that the transverse direction is parallel to the longest side of the aluminum coupon; the bending is applied in such a way that “stretches” the elongated grains. Sample 4, however, is cut in such a way that the rolling direction is parallel to the longest side of the aluminum coupon, and the bending was applied in such a way that the grains tend to want to “split” instead of “stretch.” The expected outcome for these samples is that the electrochemistry of the sample bent along the short transverse direction, sample 4, would have a significantly different electrochemistry from sample 3. Both of these samples would also tend to have a varied outcome compared to the control samples as well.

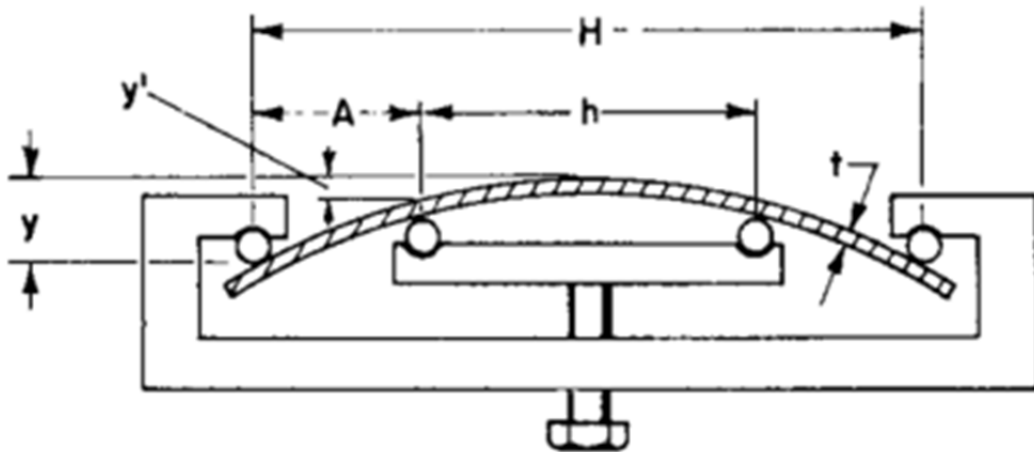


Figure 20. Four-point bend rig schematic. From ASTM-G39 (From [48]).

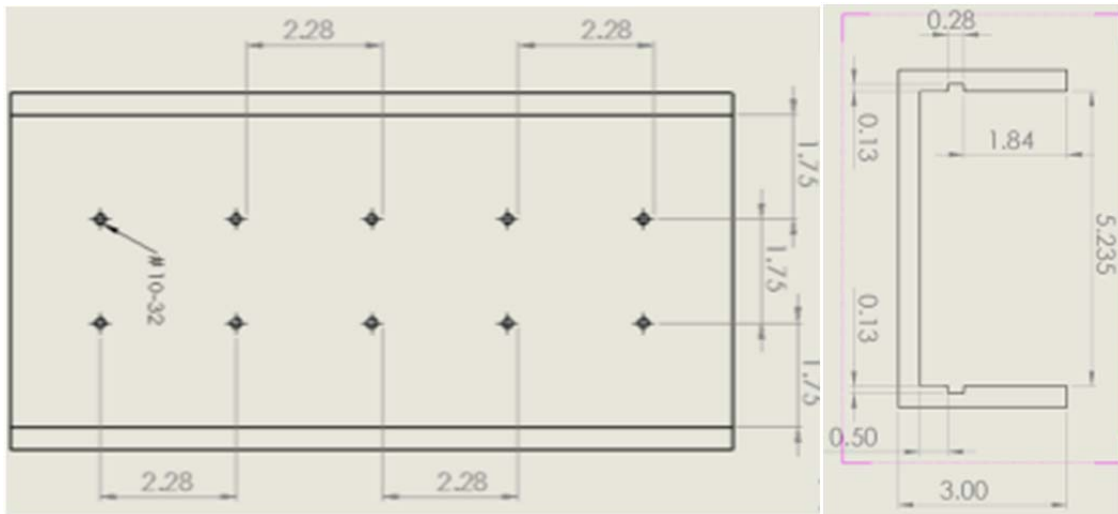


Figure 21. Diagram of top view (left) and side view (right) of four-point bend rig, dimensions in inches. From *The Role of Stress in the Corrosion Cracking of Aluminum Alloys* (From [20]).

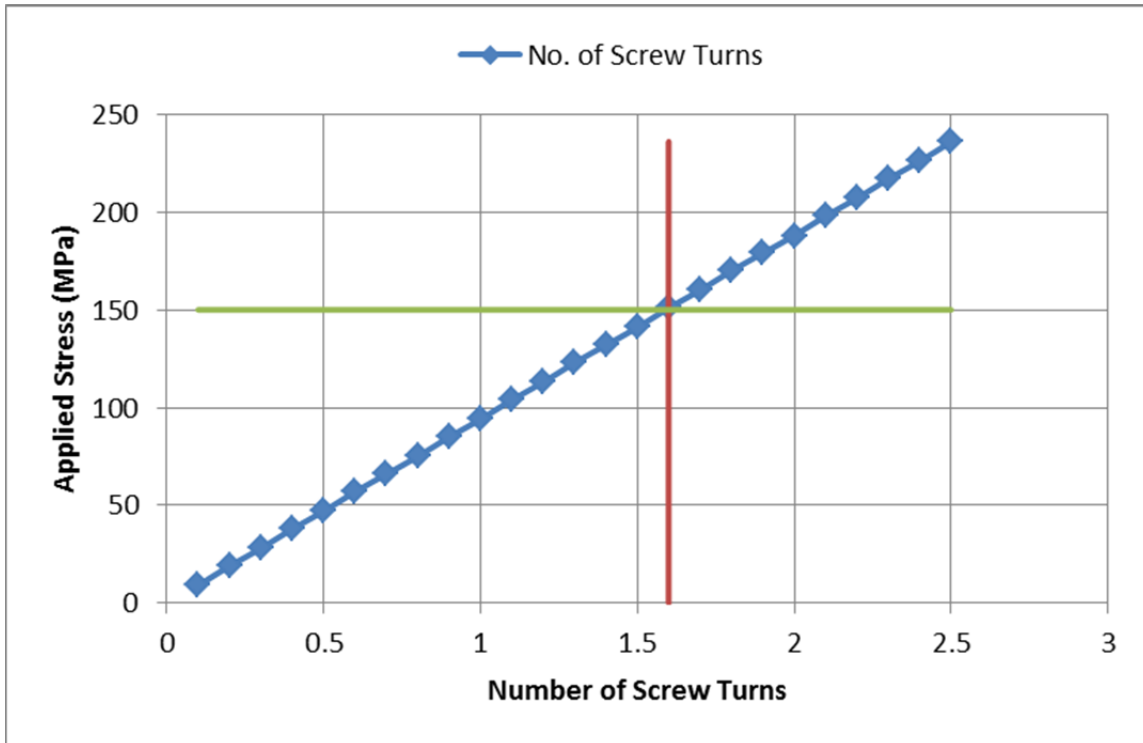


Figure 22. Stress-strain data based on displacement and screw turns calculations, After *The Role of Stress in the Corrosion Cracking of Aluminum Alloys* (From [20]).

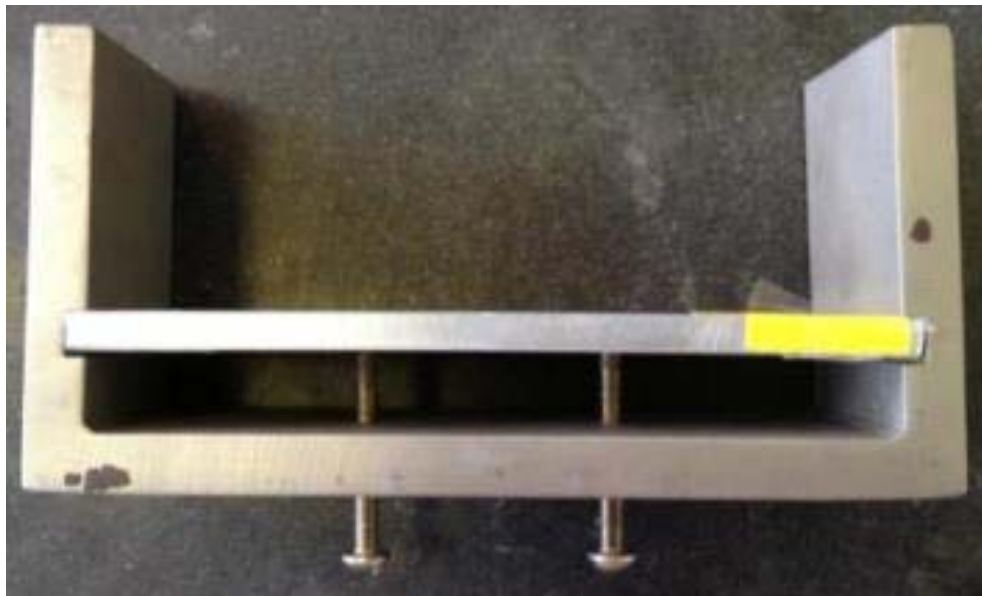


Figure 23. An example of samples without laser peening or sensitization in the bend rig (side view).

*c. Sensitized Samples.*

Samples were sensitized at either 175°C (347°F) or 200°C (392°F) for varying amounts of time, to include 24, 48, 72, 96, 156, and 336 hours based on previously conducted research by Jain et al., Searles et al., and Oguocha [3], [13], [15], [26], [32]. Figure 24 shows the region of stability and sensitization for aluminum alloys based on weight percent, which aids in the understanding of the region of temperatures chosen. The samples are cut identically to samples 1 and 2. From previous experiments, it has been determined that sensitization drastically changes the electrochemistry of an Al-Mg alloy [3], [13], [25], [32]. The samples exposed to 175°C are known to be susceptible to IGC, as discovered by Oguocha [15]. Emily Cormack's thesis research also quantified Al-Mg alloy's degree of sensitization through mass loss test, and confirmed that 175°C is an extremely unstable temperature for the  $\beta$  phase particles in the alloy [26]. However, once the alloy is sensitized to 200°C and higher, the alloy displays a return to its original, non-sensitized behavior [25]. Thus, for this experiment, sensitization temperatures of 175 and 200°C are used.



sample should resemble very similar electrochemistry to the control samples of the sensitized batch. Sample 6 is the control sample for all the laser peened samples. Sample 5 is the same, but data is taken on the weld and thus compared separately.

**b. Laser Peened Samples**

The laser peened samples were all friction stir welded through the middle of the base plate, similarly to samples 5 and 6 above, for experiments outside of this research; the ends of each coupon have undisturbed laser peening applied to them in which the electrochemical data is taken from. Laser peened samples were peened by Metal Improvement Company (MIC) in Livermore, CA. Samples were peened on both sides of the plate and are 2 inches wide, 6 inches long originating from master friction stir welded plates. Variations include differences in laser power, pulse duration, and number of passes. Samples 7–10 withstand an irradiance of  $1 \text{ GW/cm}^2$  while 11–14 have an irradiance of  $3 \text{ GW/cm}^2$ . Samples 7, 8, 11, and 12 had a laser pulse width of 18 ns, while samples 9, 10, 13, and 14 have a longer laser pulse width of 27 ns. Samples 7, 9, 11, and 13 only had 1 pass while the rest of the samples had 2 passes. The samples were denoted by irradiance-pulse width-number of passes; for instance, sample 7 has an irradiance of  $1 \text{ GW/cm}^2$ , a pulse width of 18 ns, and 1 pass, so it is denoted as 1–18–1. It seems that the more intense laser peening a sample undergoes, the more residual stress the sample experiences. Figures 25 and 26 show the samples side-by-side to emphasize the difference on the physical appearance of the grid after laser peening conditions were applied.

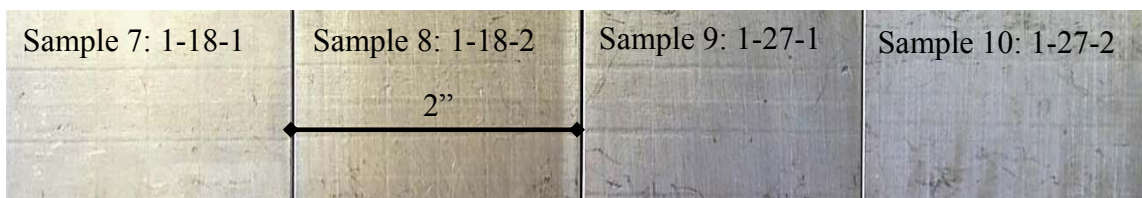


Figure 25. Laser peened samples, samples 7–10 from left to right, with varying intensities of laser peening.

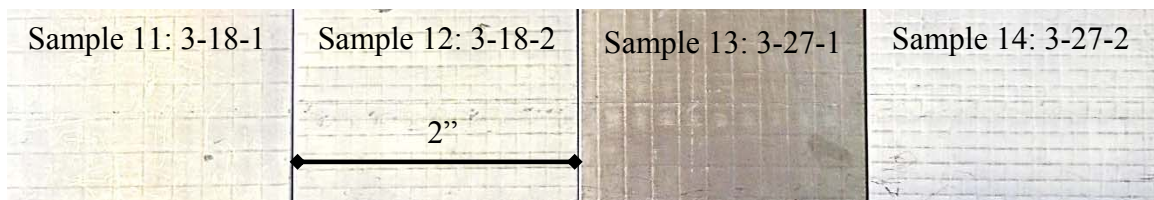


Figure 26. Laser peened samples, samples 11–14 from left to right, with varying intensities of laser peening.

### 3. Sample Summary

Table 7 in the Appendix shows a list of all the samples and duplicates with each of their individual conditions identified. Again, note that samples 1, 2, and 6 are control samples. Samples 3 and 4 are bend samples with no other external effects added. Sample 5 is identical to sample 6 except the experiment is analyzed on the weld itself. Samples 7 through 14 are laser peened. Samples 15 through 30 are sensitized at various temperatures, durations, and bending conditions.

#### C. ELECTROCHEMICAL CELL SETUP AND GAMRY FRAMEWORK™ SETUP

The potentiostat was set up using Gamry Instruments series G300 Potentiostat with the following resources. In all instances, the working electrode (WE) is the aluminum sample undergoing electrochemical reactions. A Fisher Scientific™ Accumet™ glass body Ag/AgCl mercury free standard reference cell was used in this experiment as the reference electrode (RE) (Figure 27). It operates between temperatures of -5°C to 110°C (23°F to 230°F) and has a pH range of 0 to 14 pH; this experiment set is conducted at ambient temperatures ranging from 20 to 25°C (68 to 77°F) and a pH from 6 to 7. The solution used for this experiment is 0.6 M NaCl, or 3.5 wt% NaCl solute solution with a measured pH of 6.52 at 23.6°C using an Accumet™ Basic AB15 Plus pH meter from Fisher Scientific™. The RE used a standard reference pin connector to connect to the potentiostat with an 8  $\mu\text{L/hr}$  flowrate [49]. Serial number SN4201180P 9 was used and provided by the Naval Postgraduate School. Differences exist between different types of reference electrodes. Commonly used nomenclature in material and corrosion science is voltage versus  $E_{\text{OC}}$ . This quantity is generally compared to the RE, in

which typically a Saturated Calomel Reference Electrode (SCE) is used, and it has been cited as the world's most commonly used electrode [50]. The Ag/AgCl RE is simpler in construction than the SCE and has a very similar potential, as seen in Table 3. A Hastelloy C-22 rod was used as the counter electrode (CE) for the experimental setup. Other basic equipment included alligator clips, 2-sided tape to ensure a proper seal between the solution and WE, and a non-conductive container to hold the CE and RE with an exposed area on the bottom surface for the solution to be in contact with the WE.

Reference Electrode	E vs. SCE
Saturated Calomel (SCE)	0
Silver/Silver Chloride (Ag/AgCl)	-0.042

Table 3. SCE and Ag/AgCl electric potential variations in volts. After Gamry™ Instruments' *Reference Electrodes* website (After [50]).



Figure 27. Fisher Scientific™ AccuMet™ Engineering Corporation glass body Ag/AgCl reference electrode 13-620-53. From Fisher Scientific's *Fisher Scientific™ AccuMet™ Glass Body Ag/AgCl Reference Electrodes—Mercury-Free* website (From[49]).

The basic procedure consisted of proper lab cleanliness and careful electrochemical cell setup. The use of Gamry Framework™ and Echem Analyst™ software was essential. First, the equipment and samples were washed with distilled water and dried. Note that due to the nature of the experiment, especially with laser peening, the samples were *not* polished so as to not disturb, or essentially alter the laser peening process by removing residual stress. The non-conductive container is mounted to the base metal using double-sided tape to ensure a proper seal. The tape allows exposure to an area large enough for the solution to touch the WE, in this case, an exposed surface area of 0.317 cm<sup>2</sup>, and must be properly placed so as to avoid leakage of the solution.

The CE was attached to an alligator clip classified by its red identifier; the WE was attached to a green alligator clip; the RE was attached to a white connector. The WE was grounded by a black alligator clip. The RE and CE are mounted to the non-conductive container by non-conductive clamps; the RE must be free at the tip and must not touch the base metal or any other surface; while the CE must not touch the base metal. The 0.6M NaCl solution was poured into the container, ensuring the entire surface of the solution was exposed to air as a free surface, not impeded by clamps or other experimental items. The WE, CE, and RE leads from the alligator clips were attached to the potentiostat via associated cabling. A summary of the leads and their respective locations are shown on the simulated “dummy” circuit in Figure 28. An example of the actual cell setup is presented in Figure 29. Figure 30 shows the electrochemical cell in a bend rig.

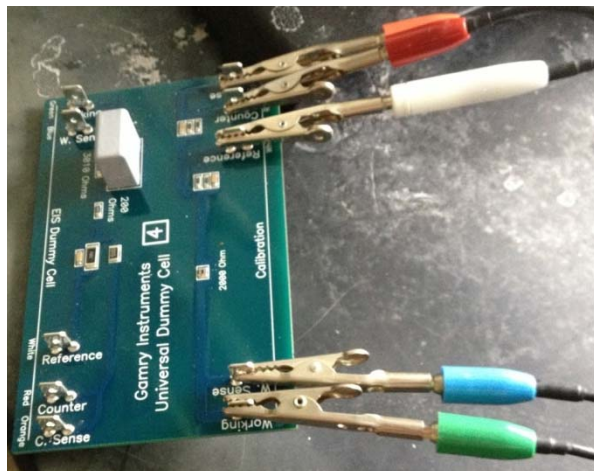


Figure 28. Summary depiction of Gamry Instruments™ Universal Dummy Cell setup for lead connections to the potentiostat.

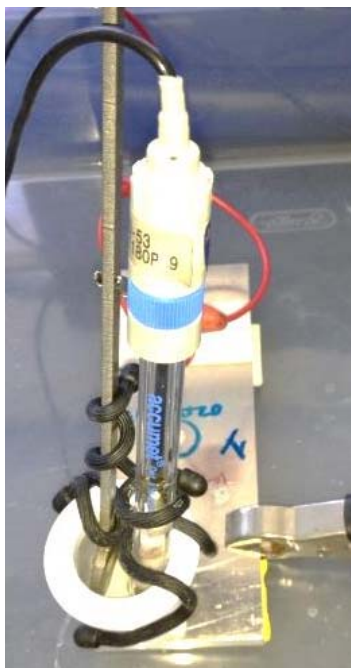


Figure 29. Electrochemical cell setup: reference electrode type 13-620-53, counter electrode Hastelloy C-22, AA5083-H116.

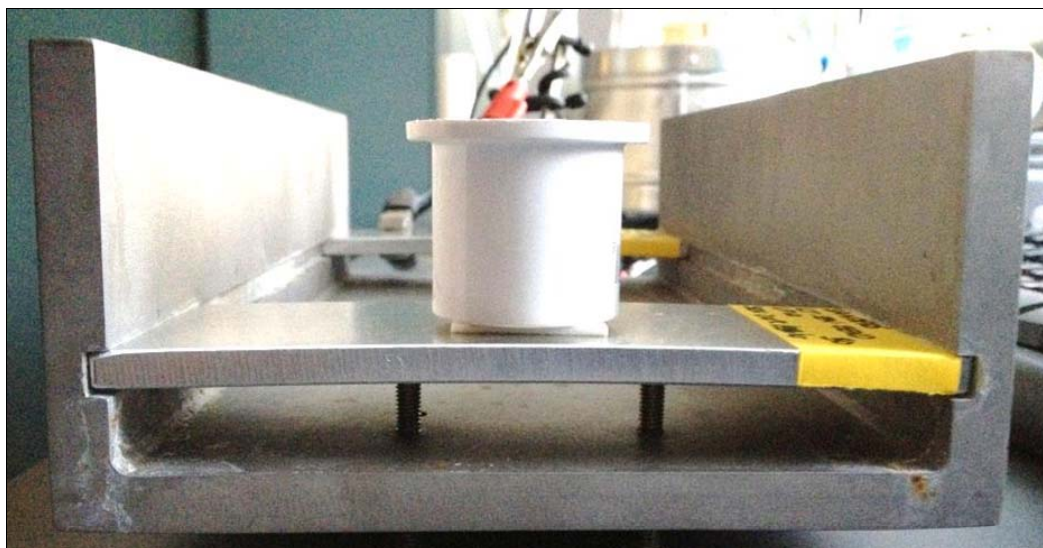


Figure 30. Bending rig setup: sample in 150 MPa applied to lower edge, with tension along the electrochemically measured surface.

Upon the completion of the electrochemical cell setup, Gamry Framework<sup>TM</sup> software was used for the potentiostatic EIS experiment, which was performed under the following settings summarized in Table 4, which were the actual experimental parameters

for EIS used in Gamry Framework™ and recorded in Echem Analyst™. EIS scans were used to determine system stability and determine  $R_p$  values. Upon completion of the first EIS scan, we continued with the first CP scan. The CP data acquired  $E_{CORR}$ ,  $E_{RP}$ ,  $E_{CRIT}$ , and  $i_p$ . The CP parameters are also summarized in Table 4. Note that the Final E is set to -0.5V to match the starting parameter, but the system can be monitored to stop manually any time after  $E_{RP}$  has been reached. The initial delay for both systems ensures that the system is stable enough to take a reading, and is set to 300 seconds or 1mV/s.

EIS Experimental Setup				CP Experimental Setup			
DC Voltage	0	V	vs EOC	Initial E	-0.5	V	vs EOC
AC Voltage	5	mV rms		Final E	-0.5	V	vs EOC
Initial Frequency	300000	oHz		Apex E	1.2	V	vs EOC
Final Frequency	0.1	Hz		Forward Scan	1	mV/s	
Points/Decade	10			Reverse Scan	1.5	mV/s	
Area	0.3167	cm <sup>2</sup>		Apex I	50	mA/cm <sup>2</sup>	
Conditioning Time	300	s		Sample Period	1	s	
Conditioning E	0	V		Sample Area	0.3167	cm <sup>2</sup>	
Initial Delay Time	300	s		Density	3	gm/cm <sup>3</sup>	
Initial Delay Stab	1	mV/s		Eqiv. Wt	1		
Open Circuit	-0.8087	V		Conditioning Time	60	s	
				Conditioning E	0	V	
				Initial Delay Time	300	s	
				Initial Delay Stab	1	mV/s	
				Open Circuit	-0.8716	V	

Table 4. Gamry Framework™ potentiostat EIS and CP experimental setup parameters.

It is important to mention the sequence of EIS and CP scans, as it helps to understand the behavior of the system. After the first CP scan was conducted, the second EIS scan was performed under identical conditions consecutively and without moving or disturbing the system. Immediately following this step, the second CP scan was performed without time delay in between scans, and with identical conditions to CP scan 1. Then, EIS scan 3 was performed, followed by CP scan 3 with conditions as before. Finally, EIS scan 4 was conducted. For clarification, the scans were performed in the following order: EIS scan 1, CP scan 1, EIS scan 2, CP scan 2, EIS scan 3, CP scan 3, and EIS scan 4 with identical conditions and without time delay between scans except for

as designed in the parameter setup in Table 4. Note that this sequence builds and breaks down the passive layer film with each CP scan (roughly 25 minutes per scan), and the system does not remain in place long enough to study a more permanent passive layer film.

Complex impedance is determined by both real and imaginary parts, and can be related through the phase angle. Series-parallel combinations of circuit elements defined the overall impedance of a standard three-electrode cell used in this corrosion analysis. The data obtained in these experiments was analyzed with both Bode and Nyquist plots, which reveal important information about the solution resistance. EIS data enables comparisons between the solution resistance ( $R_S$ ), polarization resistance ( $R_P$ ), and interfacial capacitance or double layer capacitance ( $C$ ) between the surface of the corroding material and the fluid. This further confirmed or rejected information obtained by the CP curve data. Figure 31 outlines the data spectrum for  $R_P$ ,  $R_S$ , and  $R_S+R_P$ .

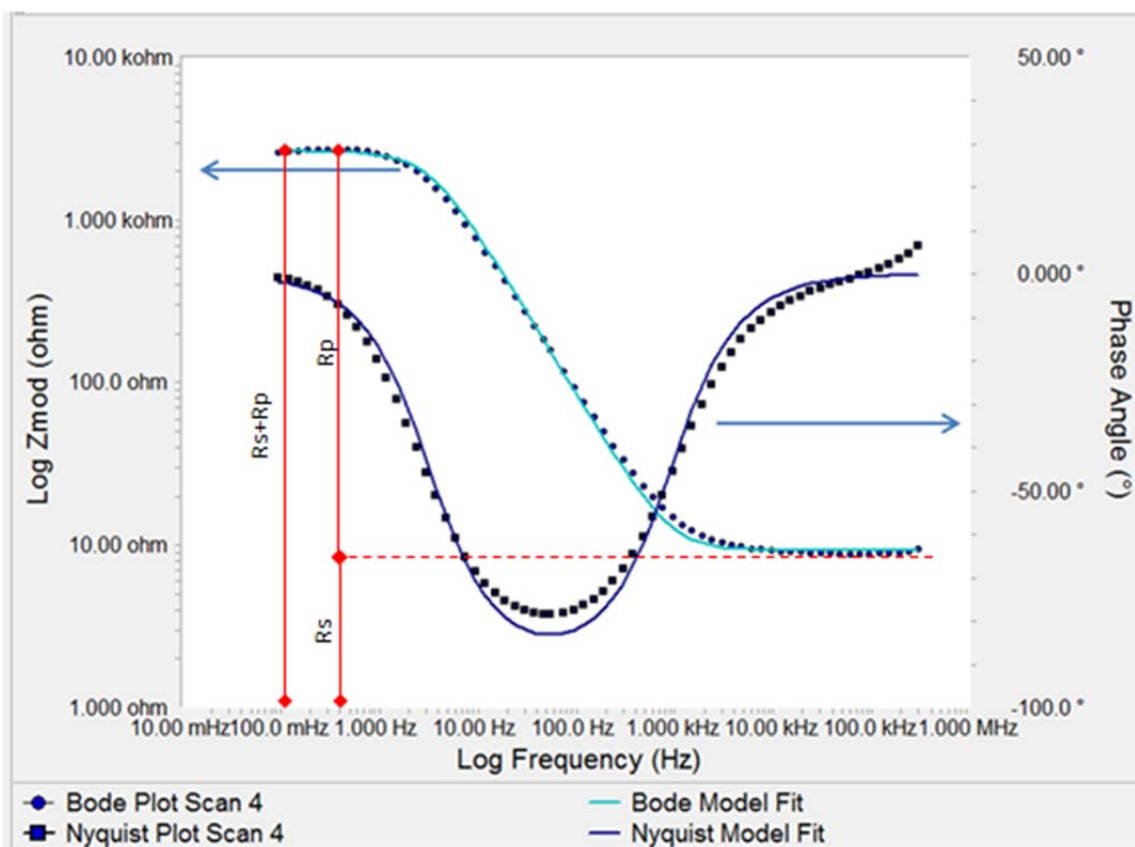


Figure 31. Echem Analyst™ Electrochemical Impedance Spectroscopy Bode and Nyquist plot following a typical resistor – resistor/capacitor circuit model using the simplex method, showing  $R_S$ ,  $R_P$ , and  $R_S + R_P$  with curve fit data.

### III. RESULTS

The cyclic polarization data showed a general progression for all samples. The full table of data for every sample is located in the Appendix, VI.D. The same is true for EIS scans, and those can be found in the Appendix, VI.E. Since the samples were not polished prior to testing, the first scan for EIS and CP appears to have removed the mill oxide layer on the material. The second and third scans represent a typical aluminum corrosion response with a clearly visible corrosion potential and corrosive current density, a breakdown potential and a repassivation potential. We discovered a pattern for most of the samples, which behaved in an unstable fashion for the first EIS scan. The R/C circuit model used for this experiment was not well-fit to any first scan EIS curves. This implies that there are more resistive layers and capacitances impeding or interfering with the applied voltage on the sample. These are examples of the range of differences experienced between the first CP scans of all the AA5083-H116 samples used in this experiment. Some reflect what may be a mill-oxide layer interfering with the unexpectedly wide range of results in the first scans.

Figure 32 shows the variance between CP scans. Scan 1, in blue, does not show a breakdown potential throughout the scan. Scans 2 (green) and 3 (red) do show a clear breakdown potential. The scans also shift. Notice that  $E_{CORR}$  for scan 2 is much less than scan 1. The same is true for scan 3 where  $E_{CORR}$  here is much less than scan 2.  $\Delta E_{CRIT}$  ( $E_{CRIT}-E_{CORR}$ ) is much greater for scan 3 than scan 2. This implies that the stability of the oxide layer is better. Scan 1 appears to dissolve a mill layer oxide while scans 2 and 3 have developed a protection by building the aluminum oxide layer.  $\Delta E_{RP}$  is also much greater for scan 3 than scan 2. These trends between scans are seen in every sample, regardless of the conditions applied. In this particular sample, we see several shifts in breakdown potential, passive current density, corrosion potential, and polarization resistance from scan-to-scan.

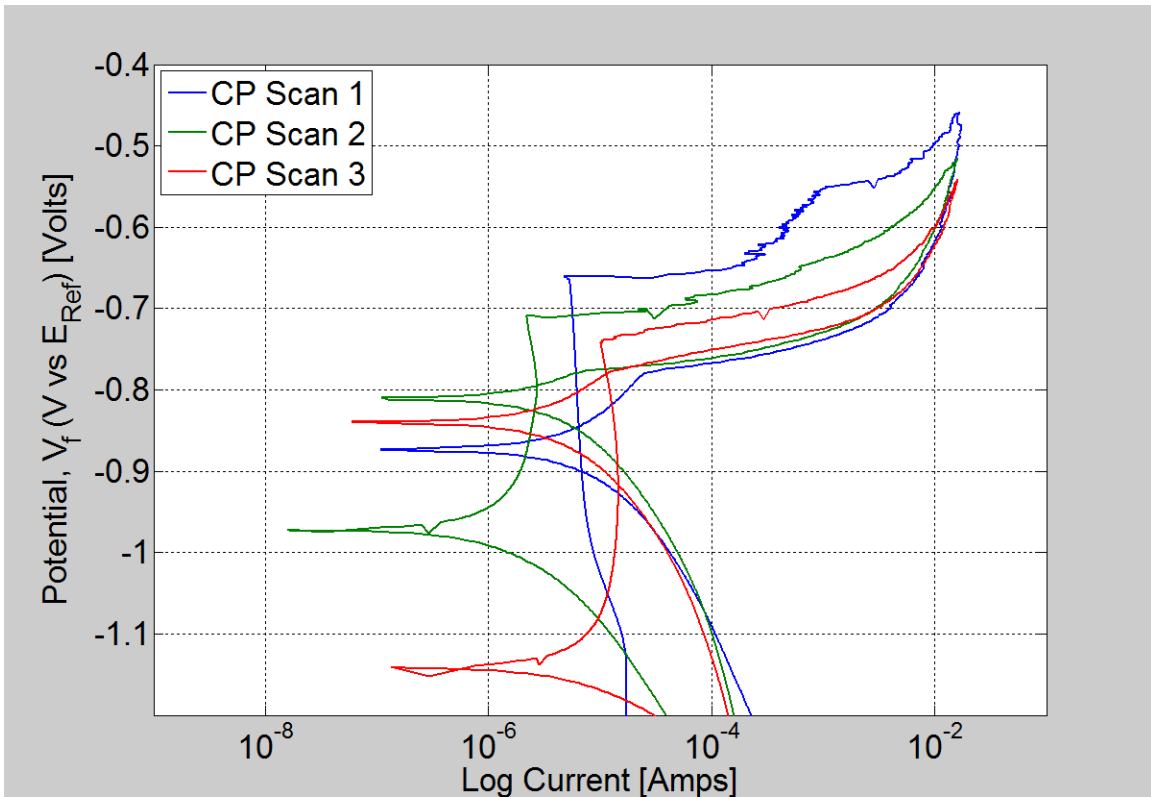


Figure 32. Cyclic polarization curves: control sample 1, scans 1–3.

Figure 33 is an example of the drastic change between scan 1 and scan 4 for EIS. Note the unsteady behavior of scan 1. Each progressive scan is closer to following the basic R/C circuit simplex model fit, represented by the solid line. The value of this plot is to show how widely spread the data proves to be from scan to scan and to emphasize why CP scan 1 data is ignored for the remainder of this work. The dotted lines represent actual data points (red data points for scan 1, blue data points for scan 4, “+” markers for phase angle points, and “•” markers for  $Z_{\text{mod}}$ ) while solid lines indicate the simplex model fit curves. Again, this behavior of increasing stability was similar for all of the samples in their progression, regardless of their condition.

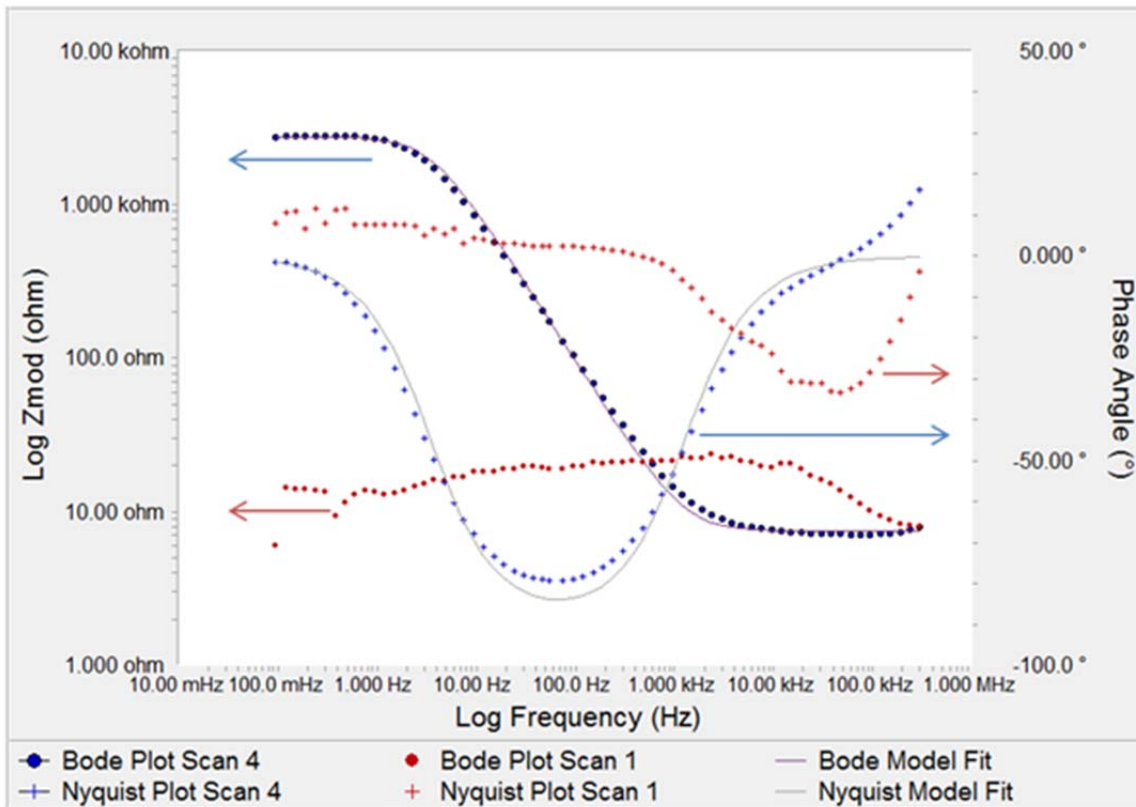


Figure 33. Echem Analyst™ Bode and Nyquist overlay plot for sample 1, scans 1 and 4.

An important note on the routine of this experiment is that the passive layer is developed as the experiments are conducted. In other words, as each scan is performed on the sample, the electrochemical voltage is driven in such a way that for each cyclic polarization curve, a passive layer film forms for each scan and is broken down as the scan progresses. The experiment does not attempt to measure effects of stress on an already existent passive layer film. Instead, it measures the effects of stress as the passive layer film is developed, broken down, and developed again as scans progress. On the second and third scans, the film forms a more predicted oxide film. The CP and EIS scans reflect this. EIS scans before and after CP scan 1 are different because the surface oxide film has changed. It is reflected as higher impedance. Another important observation made on nearly every sample is that the initial cyclic polarization scan output did not reveal a breakdown potential as mentioned earlier in section III.A. This can be seen in Figure 41. However, the second and third CP scans showed a positive hysteresis loop

with a well-defined breakdown potential. The fact that each sample indicated a similar response implies that the experiments and scans are consistent in. This also indicates that the Al-Mg alloy is extremely unstable prior to developing a passive layer film. This is reinforced by the Bode and Nyquist plots as well, and further again by a resistor/capacitor circuit model.

In Tafel kinetics, we see that the  $\beta$  phase is less noble than  $\alpha$  phase for Al-Mg alloys. Corresponding shifts in passive film is less protective so if  $I$  increases,  $R$  should decrease. Since a definite breakdown potential does not exist for scan 1 in all cases, a passive layer film does not exist on the surface for the first CP scan. For the second and third scans,  $E_{CORR}$  seems to shift down, and the material becomes less noble. If  $E_{RP} = E_{CORR}$ , the material is active. If the CP curve is smooth where a breakdown potential should exist, yet does not reflect a repassivation potential, we are looking at an anodic electrochemical reaction. If the breakdown potential has a sharp transition, there exists an oxide layer. If  $E_{RP}$  is greater than  $E_{CRIT}$ , a film breakdown does not exist and the material behaves in a passive nature, regardless of the applied voltage. If  $E_{CRIT}$  is greater than  $E_{RP}$ , and  $E_{RP}$  is greater than  $E_{CORR}$ , there is limited passivity. As  $i_p$  increases, resistance impedance decreases and we can assume that the passive film provides less protection. As  $i_p$  decreases,  $E_{RP}$  increases, and the passive film is more protective. We expect third case to be true for laser peened AA5083-H116; we expect the second case to hold true for sensitized AA5083-H116. A desire for the laser peened samples is to see a higher  $\Delta E_{CRIT}$  and  $\Delta E_{RP}$ ; we expect the contrary for sensitized samples. The mixed potential theory states that the more  $\beta$  particles make the material behave less nobly. It appears that  $i_p$  trends up by a factor of 2 from an as received sample to sensitized sample, and by a factor of 3 by laser peening. This is assuming the only shift is due to  $\beta$  phase and  $\alpha$  phase particles.

$R_p$  measures the quality of the oxide layer. We expect that stretching the surface by placing the sample in tension gives the passive layer oxide layer more area to grow. The potential region of stability improves with laser peening, which are defined by boundaries of the Pourbaix diagrams. From sensitization to sensitization with bending and applied tensile stress, the range of thermochemical stability, or  $\Delta E_{RP}$ , may be

decreased due to applied tension to the samples. There is an intact passive oxide film. Sensitizing drives  $\Delta E_{RP}$  and  $\Delta E_{CRIT}$  up while bending drives  $\Delta E_{RP}$  and  $\Delta E_{CRIT}$  down. The noise experienced may be a result of  $E_{CORR}$ , as the Al-Mg alloy, in general, is very unstable in NaCl solutions. Ions in solution give current higher voltage with more ion flow. Sensitized drives the resistance up significantly, while tension drives resistance up even higher.  $I_p$  is a good estimate of passive film quality. As passive current density decreases, resistance increases on the film that is present and thermal stability decreases. Passive current density increases as sensitization occurs, to an extent. Particles of the  $\beta$  phase present in the alloy may not be passive at all, and may be less protective than the  $\alpha$  phase oxide layer. The passive film is more conductive and the material is compromised. Characteristics are consistent between  $R_p$  and  $i_p$  for sensitized materials, and bending. The material appears to be enhancing the resistance of the oxide film and making material, essentially, better in passive layer film quality. The behavior for  $\Delta E_{CRIT}$  and  $\Delta E_{RP}$  appear to shift up with sensitization, and down with applied tension in general.

One important note that was discovered during the experiment process is that typically, unpolished samples on the first scan displayed what's observed as a lack of a breakdown potential, indicating a mill oxide layer exists and the protective passive layer oxide does not. This loop is typical behavior for aluminum alloys at room temperature on the first scan for cyclic polarization. Upon running the second scan over the same section of the aluminum coupon without disturbing the equipment, the data displayed the more commonly known corrosion curve for polished samples, which shows a very clear breakdown potential, unlike the first scan that bypasses this region. A third scan was then run over the same data point and again showed very similar behavior as the second scan. In an effort to explain this phenomenon, it is predicted that the material's mill oxide layer exists over the aluminum coupon when not polished. As a result, the first CP scan, because of the induced voltage, breaks up the mill oxide layer. The importance of CP scan 3 is that it probes the oxide formed in CP scan 2. CP scan 2's oxide layer formed as a result of dissolving the assumed mill oxide layer from CP scan 1. All of the non-laser-peened samples displayed this behavior consistently. The laser-peened samples, however,

did not. Thus, the first CP scan data has been ignored for the remainder of this experimental analysis.

From a purely statistical standpoint, three control samples were performed, one rolled in the T direction, one rolled in the L direction, and a FWS batch control sample. Each of these samples had the full scope of experiments performed on them three times. Similarly for laser peening, four laser peened experiments were analyzed three individual times, with irradiance, laser pulse width, and number of passes as parameters.

The equivalent RC circuit model used was found to adequately fit and was conceptually consistent throughout with Bode and Nyquist plots from EIS scans 2–4. The behavior of the system conformed to the simple plots with different parameters for each (Tables 11, 12, 13, and 14). Using the Simplex Method in Echem Analyst™, a simple R/C circuit was modeled and data was acquired for the impedance fit. While straightforward and uncomplicated, the model fit very well for all EIS scans following CP scan 1. EIS scan 1, however, did not fit this model well. The full data sets of EIS Scans 1–4 fitting the impedance model for R1, R2, and C3 can be found in Appendix F. The Impedance Model Editor results confirmed the theory that CP Scan 1 results are far from stable.  $\Delta R_p$  is the difference between R2 found in the model editor to fit a simplex method curve, and  $R_p$  found in the CP scans from experimental data. An estimate of 1000 ohms is used as a gage for the differential as a “good” parameter. For the equation below (36),  $\Delta R$  represents “ $\Delta R_p < 1000$  ohms,” and T represents the word “total.”

$$\Delta R_p = \left| R_{p1_{experimental}} - R_{p2_{model\ fit}} \right| \quad (35)$$

$$\% Scans_{\Delta R} = \frac{\# \text{ of Scans}_{\Delta R}}{\# \text{ of Scans}_T} \times 100\% \quad (36)$$

The smaller  $\Delta R_p$  is, the more likely that the data used from those scans is consistent and reliable. In all cases, for scan 1, only 12% of  $\Delta R_p$  values are within 1000 ohms of each other; several are well outside of 10,000 or even 100,000 ohms of each other for this particular scan (found in the Appendix F). Scan 2 shows that 82.5% of data points are within 1000 ohms while Scan 3 only shows 75% are within 1000 ohms for  $\Delta R_p$ . This implies that scans 2 and 4 for EIS are the most reliable by ways of determining

$R_p$  values for comparison, while scan 1 is very unreliable as the system at this point is unsteady. It also implies that after performing CP scan 1, the data is very reliable, and that CP scan 3 is the most consistent and probably most useful in comparison. Only CP scan 3 data will be used to evaluate trends from this point forward.

Scan 1	Scan 2	Scan 3	Scan 4
12.50	82.50	75.00	85.00

Table 5. Comparative results of EIS scan 1, 2, 3, and 4 for  $\Delta R_p < 1000$  ohms.

Since EIS scan 1 was taken prior to CP scan 1, the electrochemical behavior at that stage for EIS should be reflective of that for CP, and similarly for scans after EIS and CP scans 1. EIS scan 2 is a good indicator that, since the data appears to be consistent and stable, the data output for CP scan 2 should also be very reliable. EIS scan 3 shows a suggestive drop in consistency, and may reflect inconsistent data for CP scan 2. However, EIS scan 4 data is impressively stable, and shows that CP scan 3 should reflect very similarly accurate results. Impedance Model Editor data for scan 1 through 4 are shown in the Appendix (Tables 15 through 18) to compare extreme differences in EIS behavior before and well after a passive layer film has been introduced into the system.

#### A. CONTROL SAMPLES

The control samples were performed several times for consistency and to measure accuracy in the data. Overall, the control samples proved to behave very similarly in nature.

The first scan for EIS proved difficult to analyze and use for determining trends in data. The results were extremely unstable, even with letting the system stabilize according to the desired parameters for the software. The data did not fit the predicted R/C circuit model from Figure 18. The type of data acquired for EIS scan 1 for the control samples and subsequent samples can be found in the Appendix, VI.E. With this data information, we compared  $R_p$ , which is the transition resistance between the electrode and electrolyte. We compared the differences in  $R_p$  also to determine stability.

After running CP scan 2, we again ran EIS Scan 3. Scan 3 showed exceptional stability and confirmed results for subsequent scans. EIS scan 3 for sample 1 is shown in Figure 34. EIS scan 4 is nearly identical.

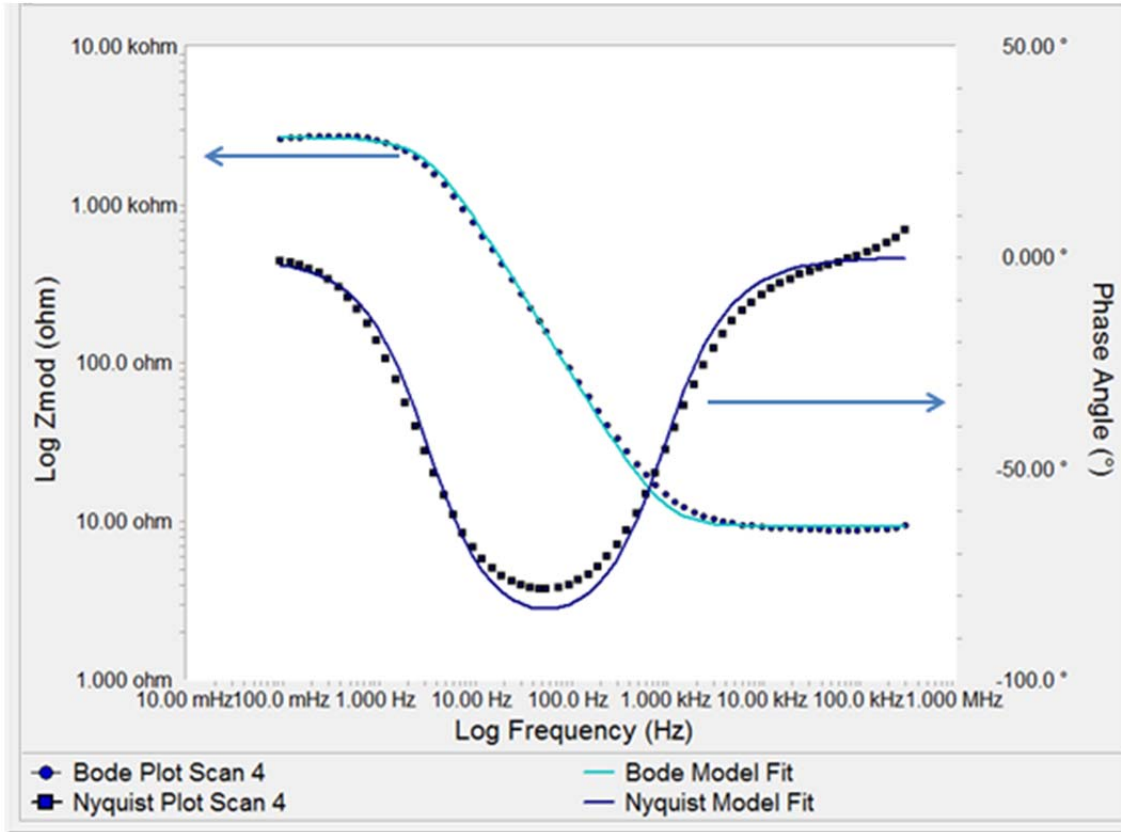


Figure 34. Echem Analyst™ Bode and Nyquist plot for sample 1, scan 3: fits well to simple R/C circuit model and shows exceptional stability of AA5083-H116.

Figure 35 displays CP scan 3 results for 3 control sample scans rolled in different directions and compared to the FSW batch samples; we see a greater divide from  $E_{RP}$  and  $E_{CORR}$ , consistent with Figure 32, and a more consistent  $E_{BD}$  from sample to sample.  $E_{CORR}$  is shifted in the more negative direction even further than seen in CP scan 2. This behavior, again, can be seen in each control sample. Note that the results for CP scan 3 appear more similar than any of the other scan results for the control samples. This indicates that scan 3 is the steadiest scan, and behaves as predicted.

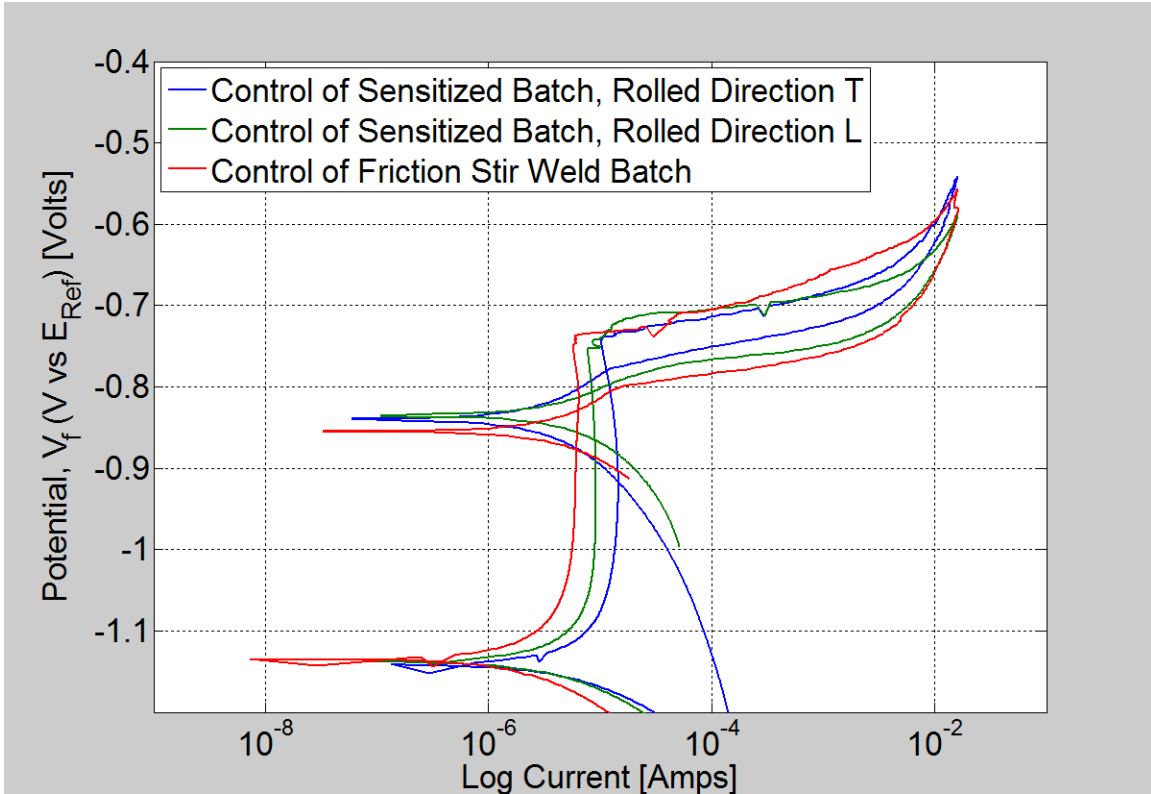


Figure 35. Cyclic polarization curves: control samples, scan 3.

## B. SENSITIZED SAMPLES

### 1. Sensitized Samples, 175°C for 24/48/72/96/156 Hours, Duration of Sensitization Comparison

Figure 36 represents the cyclic polarization scan 3 for sensitized samples exposed to thermal conditions of 175°C for 24, 48, 72, 96, and 156 hours. Physically, we can see in the CP curves a shift to a smaller  $i_p$ , and a generally higher  $E_{CORR}$  and conforming to the previously noted trends. Picking specific trends on this type of chart is difficult, Rather than provide data listed in the Appendix, we decided to compare the results of  $R_p$ ,  $\Delta E_{CRIT}$ ,  $\Delta E_{RP}$ ,  $i_p$ , and  $E_{CORR}$  as a function of sensitization time (Figures 37 through 40). This comparison, especially  $E_{CORR}$ , proves valuable in determining and confirming the effects of sensitization and validating the experimental procedures.

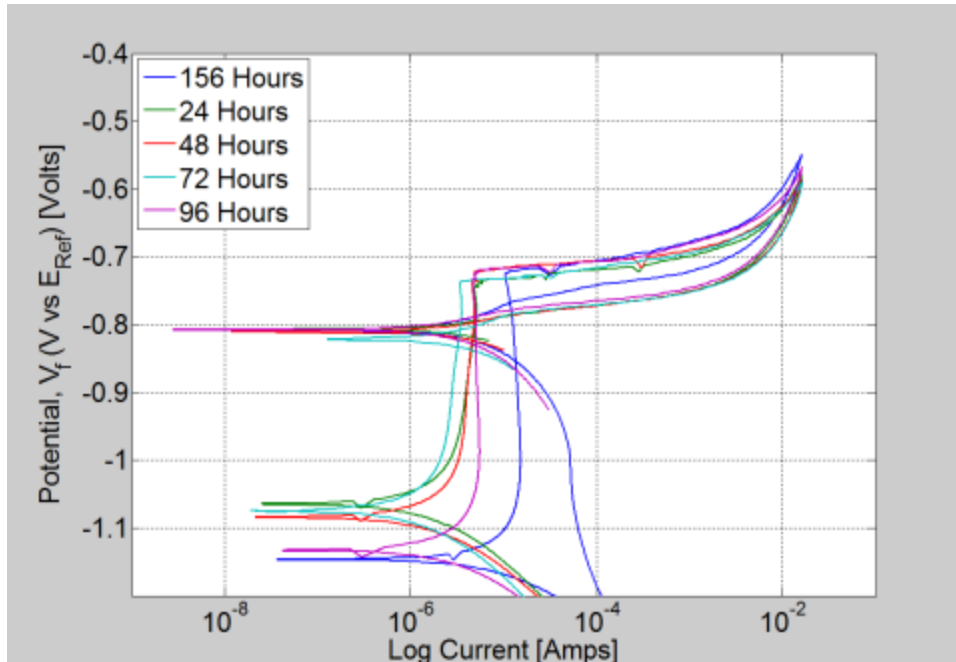


Figure 36. Cyclic polarization curves: sensitized samples 175°C for 24/48/72/96/156 hours, scan 3.

For  $R_p$  as a function of time, we see interesting results. Upon initial sensitization of the material for 24 hours, there is a significant drop in each scan for the polarization resistance.  $R_p$  steadily increases thereafter up to the 96 hour data set. The data is scattered for the 156 hour condition. This implies a larger film resistance develops as the material is sensitized.

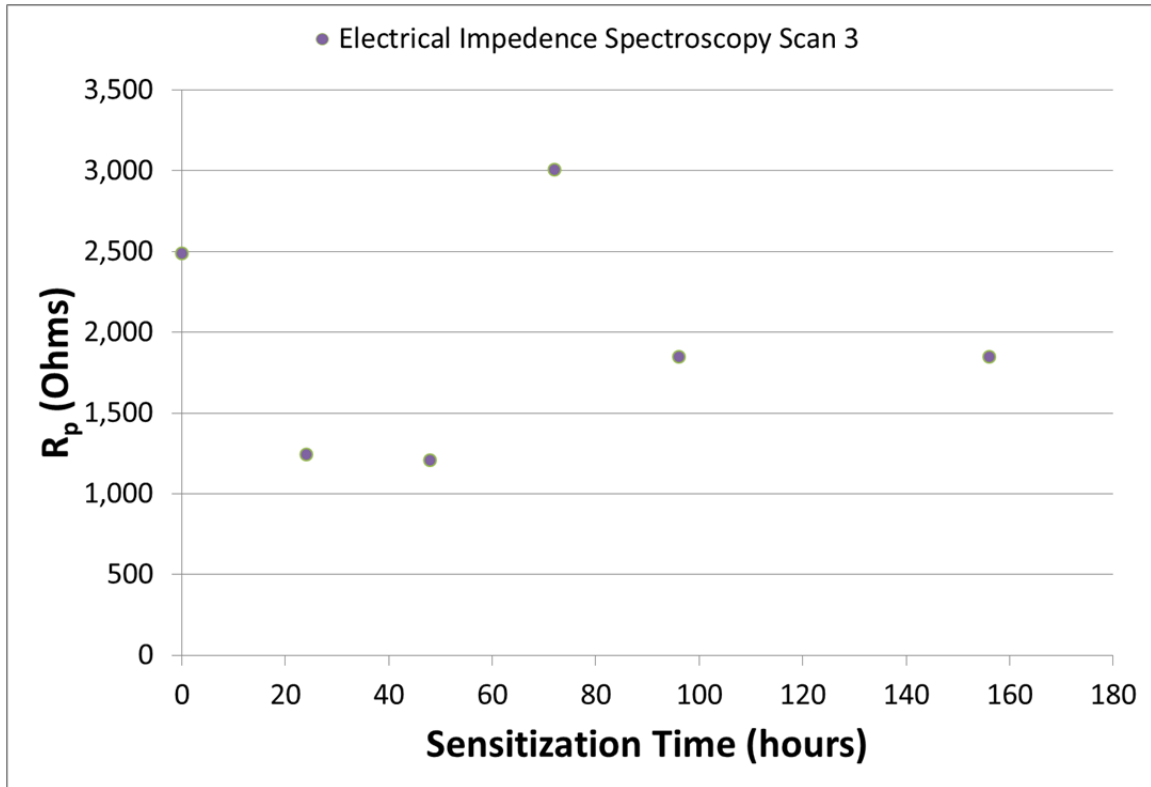


Figure 37. EIS scan 3,  $R_p$  as a function of sensitization time for 175°C.

Higher current densities indicate a positive resistance, making them dissipate power, and correlating better to the R/C circuit. A low current density indicates a more insulating material formed. We see a very general trend in which once the material is sensitized,  $i_p$  drops significantly and continues to drop to the 72 hour condition, and then increases. Figure 38 confirms trends detailed for  $R_p$  in Figure 37. An increase such as in the 156 hour condition may be due to localized breakdown of the passivating films by chloride ions. They induce localized dissolution of the passivating film at weak points, for instance, at the grain boundaries, leading further exposure to the metal and giving a rise to an increase in anodic current.

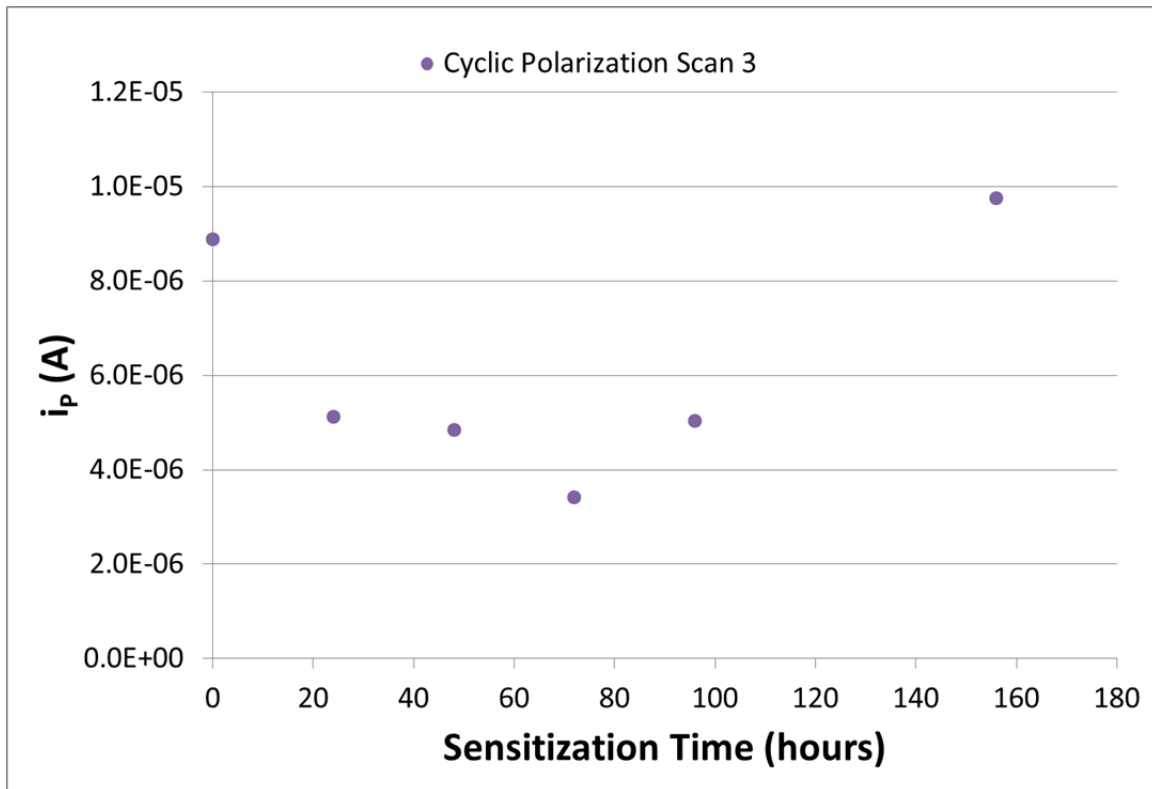


Figure 38. CP scan 3,  $i_p$  as a function of sensitization time for 175°C.

Figure 39 illustrates  $\Delta E_{\text{CRIT}}$  as a function of sensitization time. It is important to note here that CP scan 1 has a much higher  $\Delta E_{\text{CRIT}}$  than scan 2 and 3, but the trend is the same in all scans.  $\Delta E_{\text{CRIT}}$  shifts as  $E_{\text{CORR}}$  shifts. Nearly identical behavior was observed for  $\Delta E_{\text{RP}}$ , Non-sensitized samples display a larger  $\Delta E_{\text{CRIT}}$ , as does the 156 hour condition. The shorter sensitization times, though, have a much lower  $\Delta E_{\text{CRIT}}$ . Comparing  $\Delta E_{\text{RP}}$  has a very similar trend. Note for CP scan 1 for  $\Delta E_{\text{RP}}$ , the differential voltage is negative in nature. The breakdown of the oxide with the initiation of pitting occurs at the breakdown potential and increases rapidly. Inhibitive anions stabilize the passivating oxide film while aggressive anions break down the oxide film. If the ratio of inhibitive to aggressive anions is sufficiently high, the breakdown of the film may be completely suppressed and no critical breakdown potential is observed. As the ratio decreases, the breakdown potential is then observed and becomes more negative. We see this increasingly negative behavior for subsequent sensitized conditions as the material is exposed to its thermal environment for a longer period of time. A higher  $\Delta E_{\text{RP}}$  indicates how much more

resistant the alloy is to corrosion. We see that non sensitized samples are more resistant while sensitized samples generally corrode more based on this data. The 156 hour condition contradicts this.

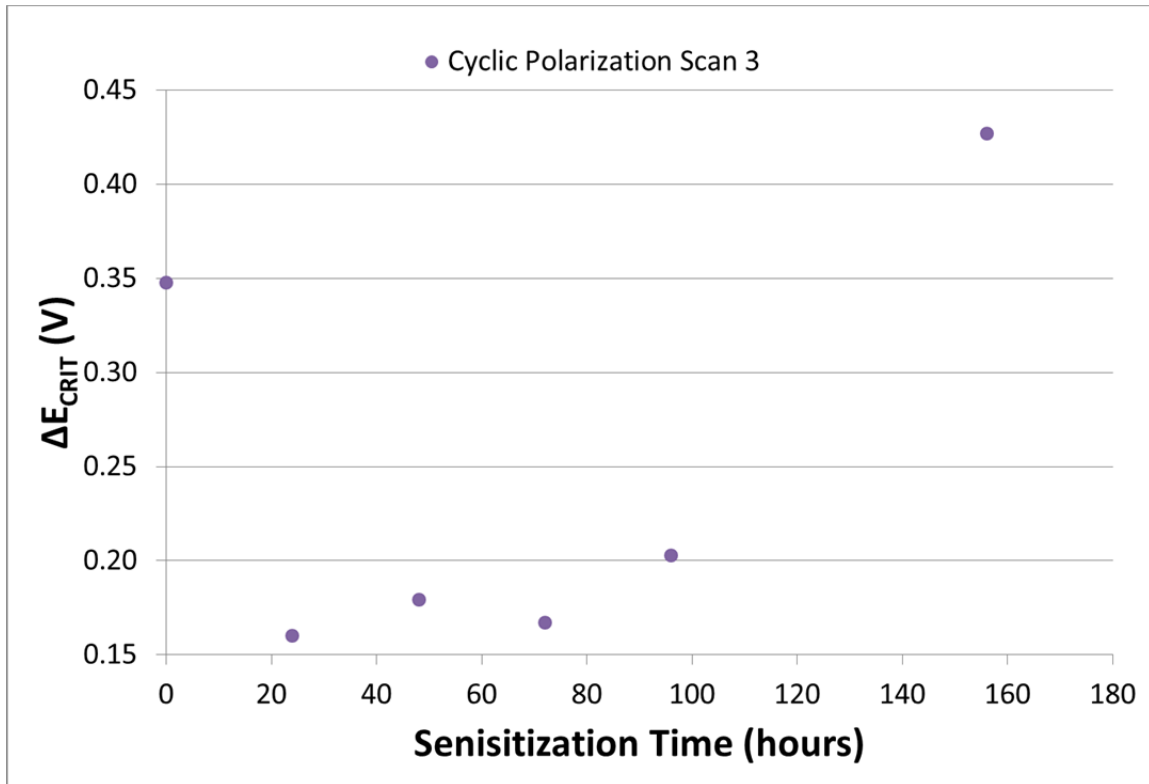


Figure 39. CP scan 3,  $\Delta E_{CRIT}$  as a function of sensitization time for 175°C.

Figure 40 shows a comparison of  $E_{CORR}$  values as a function of sensitization time. It clearly demonstrates that once the material is sensitized,  $E_{CORR}$  shifts negatively. This means that, essentially, the material is easier to corrode as it is sensitized. This widely confirms the analysis from before in which sensitization causes more corrosion [3].

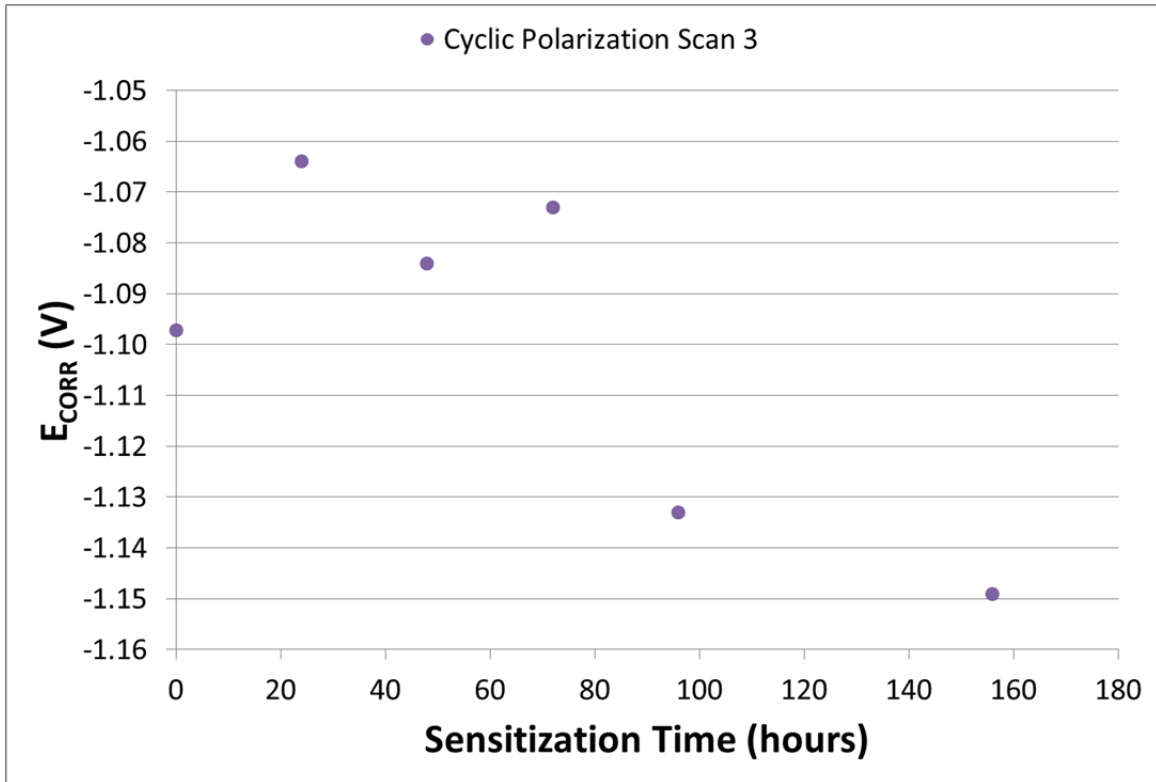


Figure 40. CP scan 3,  $E_{CORR}$  as a function of sensitization time for 175°C.

In a general comparison of all the sensitized samples of 175°C at various times, very distinct trends are observed. It seems the sensitization drives  $E_{CORR}$  to be more negative as sensitization intensity increases, and thus, forces the alloy to behave less nobly as a metal. This observation is seen in Table 53 in the Appendix. For sensitization conditions of 24–72 hours, the  $\Delta E_{RP}$  and  $\Delta E_{CRIT}$  are significantly smaller than the average control samples for this particular batch. At 156 hours of sensitization, which is an extreme condition, the  $\Delta E_{RP}$  and  $\Delta E_{CRIT}$  are driven much higher (Tables 51 and 52).

## 2. Sensitized Samples in Applied Tension

### a. Sensitized Samples, 175°C for 156 Hours, 150 MPa Applied Tension

First we must compare the non-sensitized samples to evaluate the differences we expect to see between bending and non-bending samples. Interestingly enough, for the control samples in scan 3 (Figure 41), there is very little different

between bending and not bending if the samples are not sensitized. This is expected if the premise that Al-Mg alloys are resistant to corrosion is true when not sensitized. We see a slight shift up in  $E_{RP}$  for bending in both directions. We see little correlation between bending in  $E_{CORR}$  except in the sample rolled in the L direction with 150 MPa applied, which shifts in the more positive direction. Scan 2 mimicked this behavior. For the control samples, the corrosion potential appears to shift with the T direction by observation.

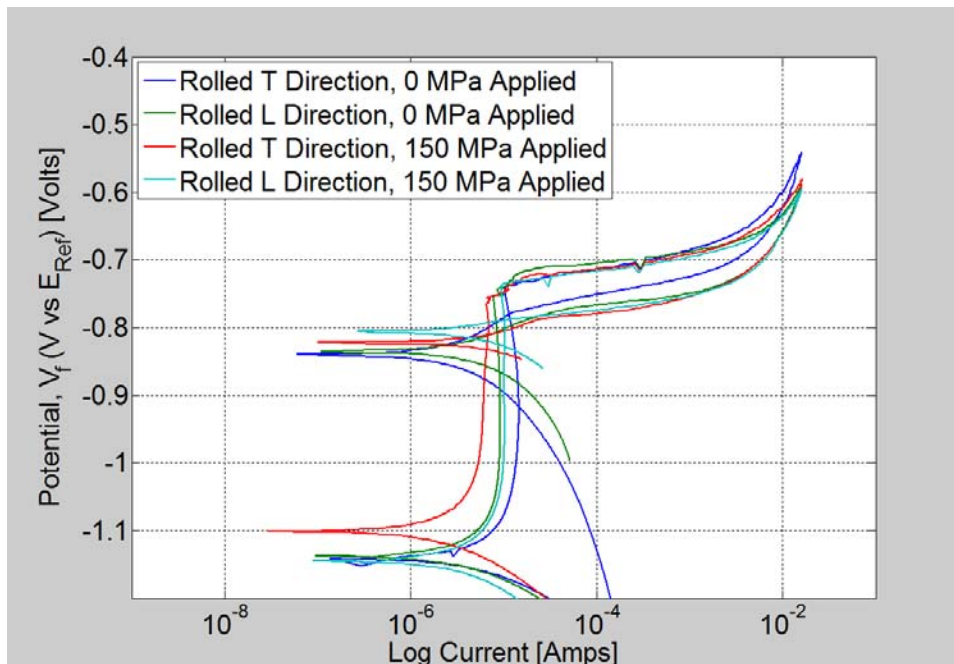


Figure 41. Cyclic polarization curves: control samples, 0 and 150 MPa applied tension, scan 3.

The materials in this section are exposed to 175°C thermal condition for 156 hours. Two rolling conditions exist for these samples, one set rolled in the T direction and the other in the L direction. For this set of samples, two bending conditions exist, one with no applied bending and the other with 150 MPa applied from the bending rig. A combination of rolling direction and bending conditions are compared for this set of data. Scan 2 is shown in Figure 40, while scan 3 is shown in Figure 42. Notice there is a greater differential between  $E_{CORR}$  and  $E_{BD}$  or  $E_{RP}$  in scan 3 than scan 2. Also notice that for scan 2, there is a significant trend with bending, which appears to shift  $E_{CORR}$  in

the more positive (cathodic) direction, while  $i_p$  decreases. We also see that rolling in L direction shifts the  $E_{CORR}$  much higher than rolling in the T direction from the non-bent condition. One possible explanation for this is the passive layer film may be creating a compressed area of the material where the bulk is in tension, but the film is in compression as it grows the oxide layer, making  $E_{CORR}$  less negative. When sensitized, both L and T directions shift, making them more cathodic in nature.

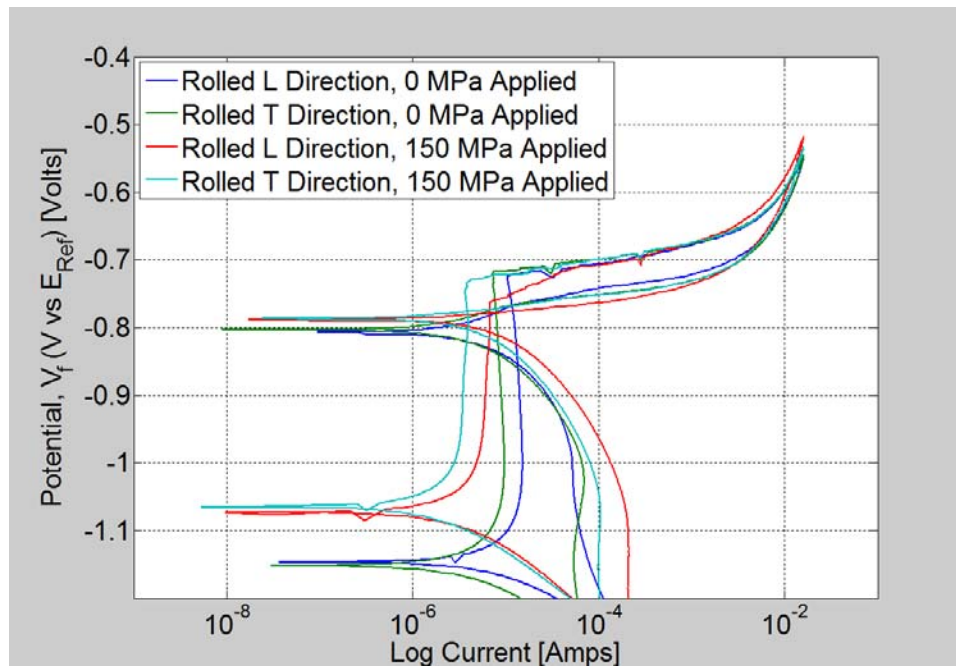


Figure 42. Cyclic polarization curves: sensitized samples, 175°C for 156 hours, rolled L and T direction, 0 and 150 MPa applied tension, scan 3.

***b. Sensitized Samples, 200°C for 336 Hours, 150 MPa Applied Tension***

Similarly to the sample set above, here we have one set of sensitized conditions with different rolling directions and different bending conditions. For this particular set of data, the samples are exposed to 200°C for 336 hours, a condition that is hypothesized to re-solutionize the  $\alpha$  and  $\beta$  phase particles back into the structure, creating again a more stable passive layer film protection. The same rolling conditions exist in the S and T direction as previously stated, and the same bending conditions exist for no applied bending and 150 MPa bending in the bend rig. Figure 43 shows scan 3. The

trends are *not* similar to the 175°C 156 hour sensitized condition; instead, we see that bending shifts  $E_{CORR}$  in the negative direction as expected while shifting  $i_p$  to the right when the sample is bent. Figure 43 is helpful in observing visually the expected effects on aluminum when comparing sensitization, bending, and rolled direction. The sensitized conditions for the three coupons are the same: 200°C for 336 hours. It shows that the sensitized condition without bending has a higher  $E_{CORR}$  than the bent samples do, as expected. Bending conditions drive the  $E_{CORR}$  down. It also shows the rolling direction as a factor, with the sample rolled in the transverse direction being driven down the most, as expected, or rather, rolling in the short-transverse direction drives the corrosion potential back up. Consequently, the breakdown potential is also slightly driven up by bending and further by rolling in the transverse direction and the corrosive current density is driven down as well. This model follows the expected trends.

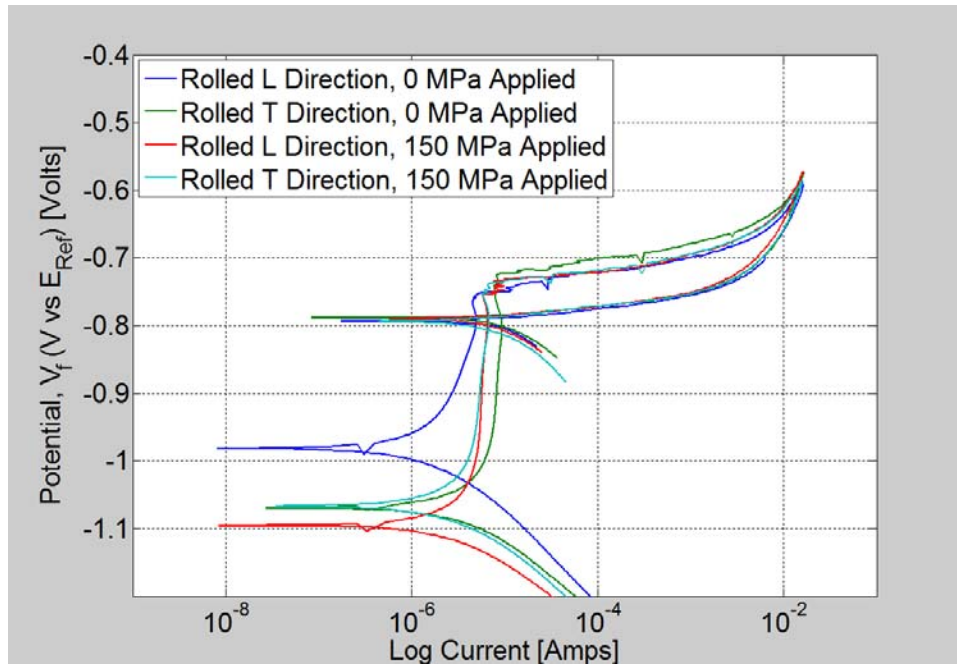


Figure 43. Cyclic polarization curves: sensitized samples, 200°C for 336 hours, 0 and 150 MPa applied tension, scan 3.

*c. Sensitized Samples, 175°C for 156 Hours and 200°C for 336 Hours, 150 MPa Applied Tension*

This set of data is comparing the two extreme sensitization conditions under applied tension to each other and the bent control samples. The cyclic polarization charts here represent the 175°C for 156 hours condition and the 200°C for 336 hours condition. Rolling in the L direction appears to have the most significant effect on scan 3. It drives a larger differential between  $E_{RP}$  and  $E_{CORR}$ . It also drives  $E_{CORR}$  down, meaning the material is more susceptible to corrosion. The T direction rolling seems to have minimal noticeable effect. The same can be said for scan 2, as it mimics the behavior of scan 3. Rolling in the L direction has a higher  $E_{CORR}$  than in the T direction. The effects of the duration that the material is exposed to with applied bending are more severe for the 200°C 336 hour condition in all cases with regard to  $E_{CORR}$ . This is an unexpected result. The same can be said for  $i_p$ .

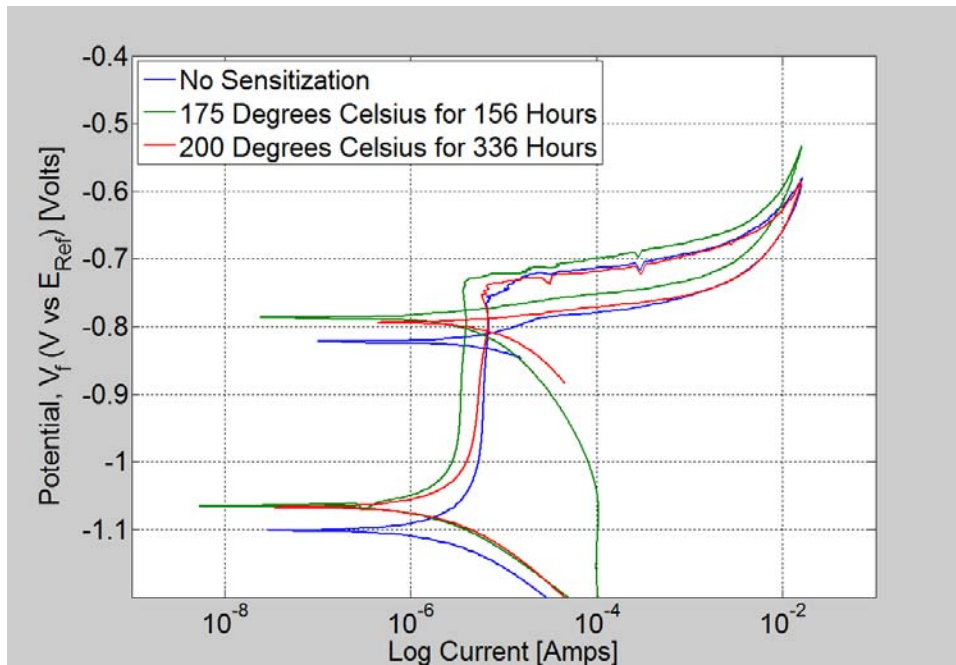
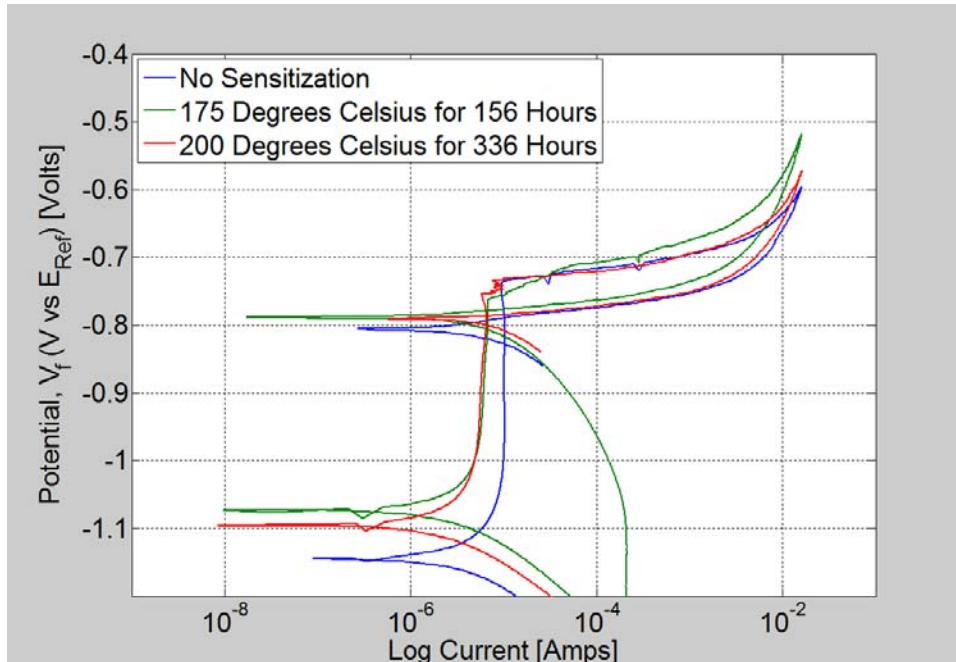


Figure 44. Cyclic polarization curves: non-sensitized and sensitized samples, 175°C for 156 hours and 200°C for 336 hours, 150 MPa applied tension scan 3, rolled L direction (above), rolled T direction (below).

*d. Summary*

To best summarize the data found for bending the sensitized samples, Tables 19-21 in the Appendix are provided for EIS and CP scans 1–3. To enhance the understanding of the behavior of the data, Figure 45 is provided, explaining what shifts in  $i_p$  and  $\Delta E_{CRIT}$  mean. As  $E_{CORR}$  becomes more negative, the material becomes more anodic and  $\Delta E_{CRIT}$  (and  $\Delta E_{RP}$ ) increase. As  $i_p$  increases, the material becomes less effective at stopping corrosion.

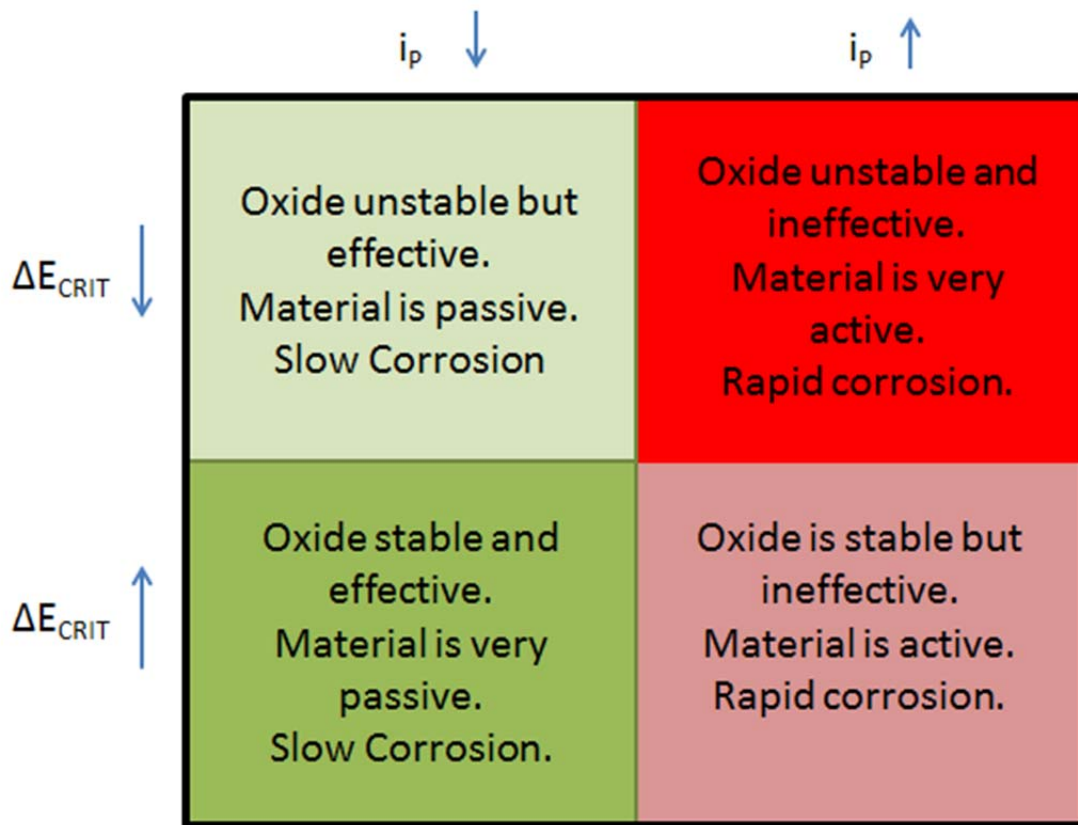


Figure 45. Summary chart explaining shifts in  $i_p$  and  $\Delta E_{CRIT}$  in regards to material corrosive behavior.

Table 6 presents a summary of only EIS and CP scan 3, and an abbreviated version of Table 21 in the Appendix. For  $R_p$ , we see a significant change, in which most cases show a decrease when bent. This makes sense, as one would imagine that bending the sample would tend to expose more of the surface and encourage a more

corrosive behavior. This appears to be the case for non-sensitized and the sensitized condition of 175°C for 156 hours, but not for the more extreme case of 200°C for 336 hours. The 200°C 336 hour condition appeared to behave more like the control samples and behaved more anodically. For the more extreme condition,  $R_p$  is driven down with bending, counter to what was believed to occur. This means the passive layer film may be gone. The polarization resistance drop, in this case, indicates an increase in corrosion current.  $E_{CORR}$  for the 175°C 156 hour condition is more negative and easier to induce corrosion than the 200°C 336 hour condition. Little can be deduced from  $\Delta E_{CRIT}$  or  $\Delta E_{RP}$ , except that bending seems to drive  $\Delta E_{CRIT}$  down for bending in the as received and 175°C 156 hour condition, and bending seems to drive  $\Delta E_{RP}$  up for the 200°C 336 hour condition. Scan 3 shows that bending drives  $E_{CORR}$  down, making the material more corrosive, for the 200°C 336 hour condition. The opposite is true for the 175°C 156 hour condition, confirming results from scan 2 and further implying that sensitization varies with time in which must be carefully monitored.  $R_p$  has notable values, in which for sensitized conditions, it's driven up significantly when bent, and more so when bent in the L direction for 175°C at 156 hours, but destabilized for the more extreme condition.  $\Delta E_{CRIT}$  and  $\Delta E_{RP}$  are greater when the sample has no bending applied for the 175°C 156 hour condition, but the opposite is true for the more extreme condition. Again,  $E_{CORR}$  is much lower for the 175°C 156 hour condition, meaning the material is more likely to corrode at this sensitization condition.

Scan 3		$R_p$	$i_p$	$E_{CORR}$	$\Delta E_{CRIT}$
Rolling Direction	Bending Applied	Ohm	A/cm <sup>2</sup>	V	V
<b>As Received (No Sensitization)</b>					
T	0 MPa	791	3.60E-05	-1.141	0.400
	150 Mpa	1226	2.17E-05	-1.101	0.346
L	0 MPa	1144	2.70E-05	-1.137	0.383
	150 MPa	961	3.25E-05	-1.144	0.408
<b>Sensitized 175°C for 156 Hours</b>					
T	0 MPa	3132	2.47E-05	-1.152	0.432
	150 Mpa	7222	2.16E-05	-1.072	0.310
L	0 MPa	566	3.70E-05	-1.146	0.422
	150 MPa	16390	1.23E-05	-1.065	0.323
<b>Sensitized 200°C for 336 Hours</b>					
T	0 MPa	2337	1.57E-05	-0.981	0.219
	150 Mpa	2220	2.09E-05	-1.067	0.315
L	0 MPa	2337	1.57E-05	-0.981	0.219
	150 MPa	2026	2.07E-05	-1.095	0.337

Table 6. EIS and CP scan 3 data, applied tension comparison of samples without sensitization, samples exposed to 175°C for 156 hours, and samples exposed to and 200°C for 336 hours.

When comparing bending conditions of the 175°C sensitized samples and 200°C samples, we confirm the effects of the material re-solutionizing itself and the  $\beta$  phase particles seem to redistribute and move away from grain boundaries, almost as if to make the material strength increase again. This is confirmed by the CP tables in the appendices. This shows that the control samples have a shift down in  $\Delta E_{CRIT}$ . The same behavior is seen for  $\Delta E_{RP}$ , but appears to have less effect on rolling direction. Once sensitized to 175°C for 156 hours, the samples' differential voltage drives up as expected. However, when sensitized and bent at the same condition, the voltage is driven down again and is the opposite of what was expected. It seems as the passive layer oxide is able to reform and is stronger in bending conditions in this region. The opposite is true for a condition of 200°C for 336 hours.

For  $i_p$ , the corrosive current density is driven down when comparing samples with no bending; the LT rolling direction drives it even further down. The

control samples compared to the 175°C for 156 hours condition seem to drive  $i_p$  down further. When comparing only the 175°C samples, the bend tends to drive  $i_p$  down.  $I_p$  for the 200°C for 336 hour condition seems erratic.

$R_p$  data for the two extreme sensitized conditions of 175°C for 156 hours and 200°C for 336 hours follow a great trend. This graph shows that bent samples'  $R_p$  is driven down significantly by half an order of magnitude by bending compared to the control. The “T” direction is also lower in all cases (not entirely significant when compared to “S”). This graph also depicts that the 175° for 156 hour sensitization level makes the metal the most sensitive condition for corrosion with the weakest passive layer film resistance, as noted Cormack and Oguocha et al. [15], [26]. By further sensitization at 200°C at 336 hours, we see the material is, in a sense, re-strengthening.

### C. LASER PEENED SAMPLES

In this set of data, the friction stir weld batch control sample and two laser peened conditions are compared. The least intense laser peened condition with irradiance of 1 GW/cm<sup>2</sup>, laser pulse width of 18 ns, and 1 pass (1–18–1) is compared to the most intense condition of 3 GW/cm<sup>2</sup>, 27 ns, and 2 passes (3–27–2). The laser peened samples exhibit the similar patterns to their overall shape as discussed previously for scan 1, while scan 3 in Figure 46 (and similarly scan 2) show a clear breakdown potential with a positive hysteresis loop. For CP scan 2, laser peening does appear to draw a greater distance between  $E_{CORR}$  and  $E_{BD}$  which would result in a shift in  $\Delta E_{CRIT}$ . The breakdown potential shifts with both laser peened conditions. The behavior for the sample with the laser peened condition denoted by 1–18–1 (sample 7) is irregular for the third scan, and the behavior is reflected for each of the 3 experiments run on that particular sample and not easy to interpret.

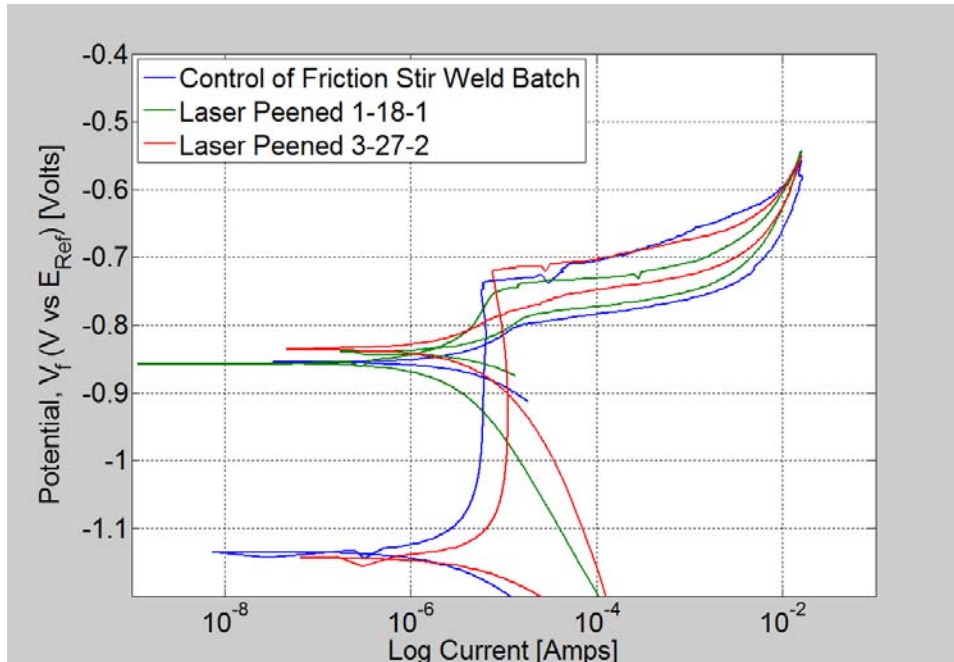


Figure 46. Cyclic polarization curves: non-laser peened and laser peened samples 7 and 14, scan 3.

No strong correlation was found between laser peening conditions and the measured corrosion response. Figure 47 shows the range of film impedance described by the laser peening conditions from EIS data. The range of  $R_p$  is hardly discernible from one condition to the next in regards to film passivity. The passivation current,  $i_p$ , displayed similar behavior as can be found for scans 2 and 3 in the Appendix (Figure 61). Figure 48 shows the ranges of  $E_{CORR}$  exhibited on the laser peened samples. Again, there appears to be no trend in the data, and it appears to be widely scattered from -0.9 to -1.2 V.  $\Delta E_{RP}$  and  $\Delta E_{CRIT}$  also had small, negligible variances in the data and do not appear to shift up or down in any type of pattern as the sensitized conditions did. The comparison charts for these parameters are seen in the Appendix, Figure 59 and 60.

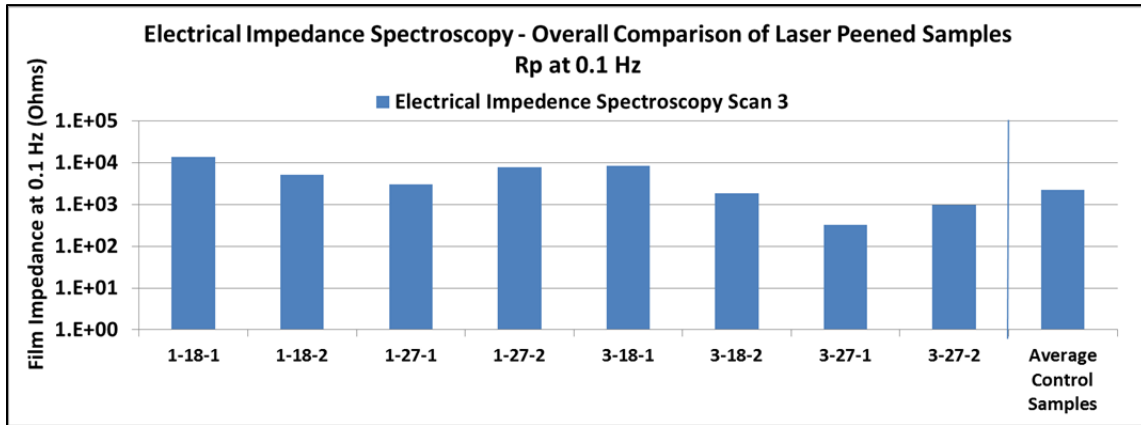


Figure 47. EIS various laser peened conditions scan 3 comparison of  $R_p$ .

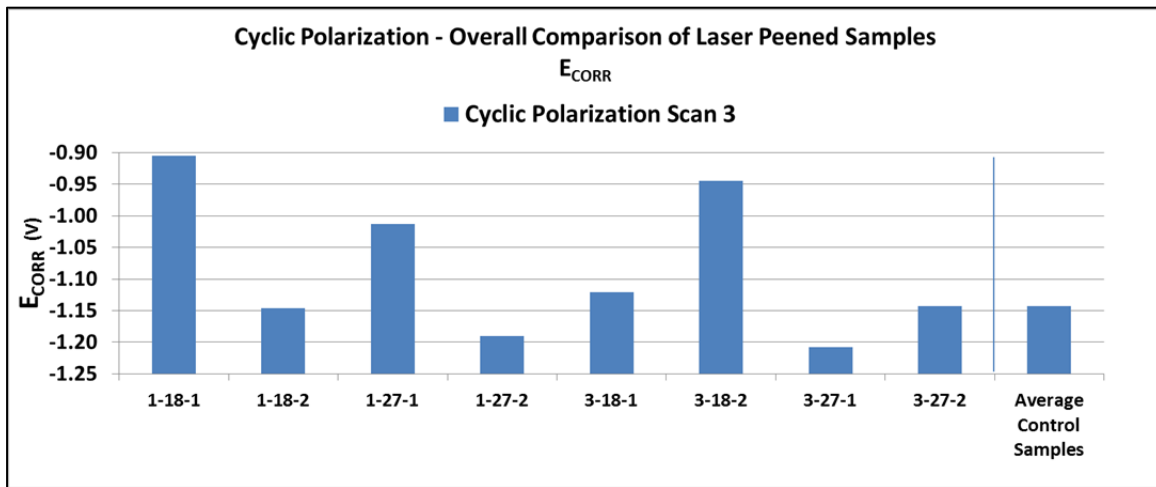


Figure 48. CP various laser peened conditions scan 3 comparison of  $E_{CORR}$ .

A multivariate analysis of variance, or ANOVA, did not reveal any significant correlation between laser peening parameters and measured corrosion response. Using commercial statistical software (JMP® 10) a linear regression model based upon irradiance, pulse width, number of peening passes, and their two-way interactions was created to analyze for significance. For example, the Fischer value for the model connection  $R_p$  with the laser peening factors was 0.17, suggesting that the variance in the data was not well described by the model. In addition, the largest t-value for any of the model parameters was 0.48, in no way large enough to identify a factor as being

significant to 95 percent confidence (which requires a t-value greater than 2). Lastly, the leverage plots (Figure 49) for this model connecting  $R_p$  with laser peening are all almost horizontal and the confidence bands do not cross the abscissa, thus demonstrating that  $R_p$  is not significantly affected by the laser peening conditions in this study. It is possible that the variation in measured corrosion response itself is large enough to mask the contributions from laser peening. If the variation in the measurement could be reduced, one might be able to discern a contribution from laser peening but not with the current data set.

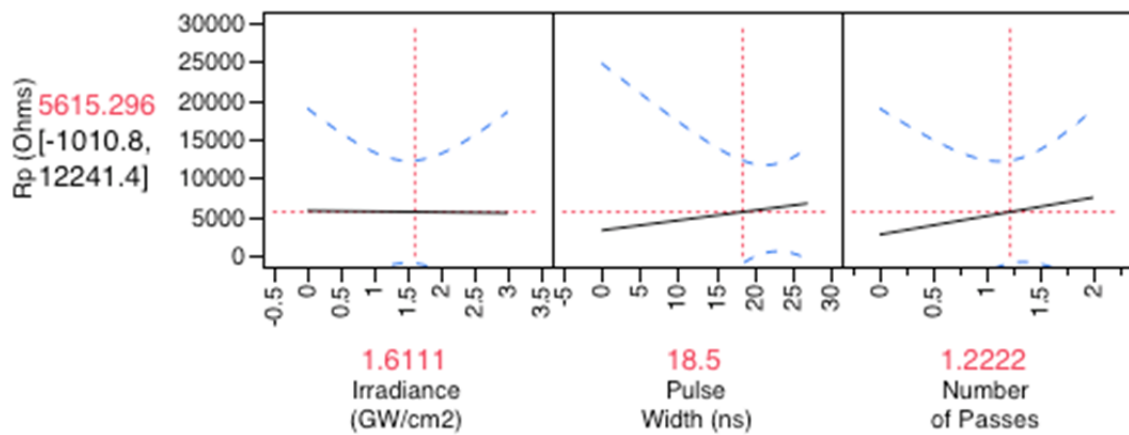


Figure 49. Leverage plots for regression model describing  $R_p$  as a function of laser peening irradiance, pulse width, and number of passes.

## IV. DISCUSSION

The results in this thesis point to the complex nature of the passivating oxide as a function of sensitization and stress. While the passivating oxide for aluminum is fundamentally based upon aluminum oxide or hydroxide, the oxide layer for sensitized AA5083 must be by nature multi-phase. At a minimum, the oxide should be a mixture of magnesium oxide and aluminum oxide, or perhaps, aluminum oxide and the spinel ( $\text{MgAl}_2\text{O}_4$ ) phase. It is also quite possible that the distribution of oxide phases is not uniform across the sample surface. Because the Mg-rich beta phase is distributed in large part along grain boundaries in sensitized material, it would be expected that Mg-based oxides would be prevalent in these areas. Using transmission electron microscopy (TEM), Jones et al. observed aluminum oxide particles along the crack path for IGSCC in AA5083; while he described these particles as aluminum oxide, he points out that they had more magnesium than in the bulk alloy and that the composition varied considerably from particle to particle [51].

The complexity of this evolving surface microstructure is further underscored by comparing the data from sensitization at 175°C versus 200°C. We found similar behaviors to that in literature in which AA5083-H116 is more corrosive when sensitized [3], [13]. The results of the sensitization experiments confirmed experiments and mimicked trends seen by Oguocha et al. and Searles et al., in which sensitization at 175°C proved detrimental, while sensitization at 200°C seemed to stabilize and increase solubility of the aluminum and magnesium [16]. While the binary phase diagram in Figure 3 suggests that one must be above 340°C (at the lowest at% of Mg) for full solutionization, other reports have observed that *intragranular*  $\beta$  phase is formed instead of *intergranular*  $\beta$  phase for temperatures around 200°C and greater. The passivating oxide that forms from this different metallic surface microstructure must necessarily be different than that formed by the grain boundary sensitized microstructure.

The application of an elastic, tensile stress definitely changed the electrochemical response of the sensitized AA5083 surface, but mechanisms behind this change are not completely clear. It is not clear why the corrosion potential ( $E_{\text{CORR}}$ ) would become more

cathodic with applied tension, but it did so for both samples with a comparable level of change for both loading directions. Both the increased polarization resistance and the decreased passivation current suggest that a more passivating film was formed under tension. This observation might be explained by the Pillings-Bedworth ratio for aluminum oxide. Aluminum oxide has a larger molar volume than aluminum metal and upon its formation, it generates a compressive stress in the surface. The application of a tensile stress may assist in the formation of the passivating oxide. Lastly, the electrochemical stability of the passivating oxide was systematically lowered by application of the tensile stress, as measured by the decrease in  $\Delta E_{\text{CRIT}}$ . It is not completely clear why the oxide would be destabilized by the tensile stress, but it seems intuitively reasonable that a tensile stress applied to an oxide film would degrade its stability, perhaps through fracture. Certainly, further experiments need to be performed to deconvolute these possible mechanisms.

The lack of influence of laser peening on the corrosion behavior of AA5083 may well be due to the gradient in residual stress values as a function of depth from the surface. Laser peening has indeed been successful in slowing fatigue and stress corrosion crack growth in steel and aluminum alloys [28], [35], [52], but it is really the compressive stress that it imparts which prevents or slows crack growth. In Figure 50, Banazwski shows that for laser peening on AA5083, the compressive stresses are quite small at the actual surface and only become larger below the surface. As the corrosion measurement itself is only probing the electrochemistry of the very surface layer, it is likely not strongly influenced by the larger compressive stresses that develop hundreds of microns below the surface.

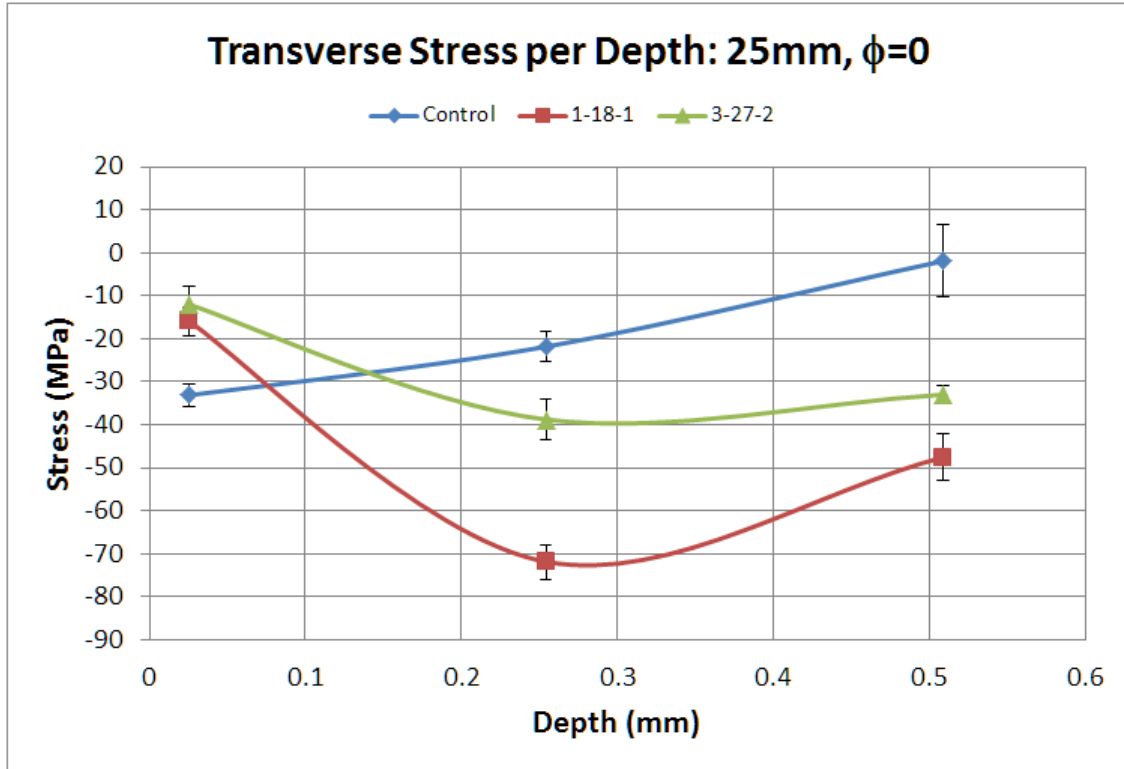


Figure 50. Transverse residual stresses as a function of depth in the 1–18–1 and 3–27–2 specimens at the 25 mm test point. From Banazwski (2011) (From [53]).

THIS PAGE INTENTIONALLY LEFT BLANK

## V. CONCLUSIONS

The purpose of this thesis was to determine the roles that stress may play in altering the corrosion behavior of AA5083. These stresses may be either harmful (residual stresses from welding) or beneficial (peening processes such as laser peening).

### 1. **Confirm Effects of Sensitization on Electrochemistry of Corrosion for AA5083-H116**

We observed the same general changes in electrochemistry after sensitization as have been previously observed for this alloy. The corrosion potential,  $E_{CORR}$ , did decrease as the sensitization time increased. In addition, we observed changes in the nature and corrosion response of the passivating oxide as a function of sensitization. The passivating current for this oxide film was comparable to the control sample, but the stability of the oxide decreased substantially.

### 2. **Assess the Effects of Elastic Stress on Electrochemistry of Corrosion for AA5083-H116**

The application of an elastic, tensile stress did measurably change the corrosion response of AA5083. The corrosion potential became slightly more cathodic for highly sensitized material. The polarization resistance increased and the passivation current decreased with the application of a tensile stress. The stability of the passivating oxide also decreased with the application of a tensile stress. These results suggest that the passivating oxide formed under tensile stress is effective at limiting ionic transport during corrosion, but that it is destabilized by the tensile stress.

### 3. **Assess the Effects of Laser Peening on Electrochemistry of Corrosion for AA5083-H116**

Laser peening appeared to have a minimal effect on the electrochemistry of corrosion for AA5083 when compared to non-sensitized samples. The irradiance, pulse width, and number of passes showed no strong correlation with the corrosion parameters measured. While laser peening does generate a compressive residual stress in this material, we found that this stress does not affect the stability or the passivity of the oxide

in a consistently measurable way. This lack of correlation is most likely due to the very surface nature of the electrochemical response. The surface carries a much lower residual stress than the near-surface layer of the material.

## VI. APPENDIX

### A. MATLAB CODE – CYCLIC POLARIZATION CURVES

```
%%MATLAB Code - Cyclic Polarization Curves
% For use in conjunction with output files from Gamry Framework™
software.
% Created by LT William Richard Fleming, USN
% Modified by LT Jennifer Sanders Fleming, USN
% Naval Postgraduate School, Monterey, CA
% 23 May, 2013

%% Acquiring Data
clear;
%cd('\special\jasandel$\Desktop\Jennifer Sanders Thesis Data\');%path
for
%data on campus, Naval Postgraduate School, Monterey, CA
cd('K:\Desktop\Jennifer Sanders Thesis Data')%%Path for Virtual Private
%Network to access data on campus, Naval Postgraduate School, Monterey,
CA
CP=3; %Cyclic Polarization Scan Number
switch CP
    case 1 %For scan 1
        cd('02JSF1CP'); %Folder path
        cmp_files={'17','18','29','30'}; %File number - correlates with
        %sample number
    case 2
        cd('04JSF2CP');
        cmp_files={'17','18','29','30'};
    case 3
        cd('06JSF3CP');
        cmp_files={'17','18','29','30'};
end

files = dir('*.xlsx');
volts=zeros(2000,size(cmp_files,2));
amps=zeros(2000,size(cmp_files,2));
c=1;
for i = 1:length(files)
    for j = 1:size(cmp_files,2)
        if(strcmp(files(i).name(1:length(files(i).name)-
5),cmp_files{j}))
            v=xlsread(files(i).name,'D66:D2000');
            a=xlsread(files(i).name,'E66:E2000');
            volts(1:size(v,1),c)=v;
            amps(1:size(a,1),c)=a;
            switch files(i).name
                case '01.xlsx'
                    n{c}='Control Rolled Direction T';
                case '01a.xlsx'
                    n{c}='01a Duplicate Control Rolled Direction T';
                case '01b.xlsx'
                    n{c}='01b Duplicate Control Rolled Direction T';
```

```

case '02.xlsx'
  n{c}='Control Rolled Direction S';
case '02a.xlsx'
  n{c}='02a Duplicate Control Rolled Direction S';
case '02b.xlsx'
  n{c}='02b Duplicate Control Rolled Direction S';
case '03.xlsx'
  n{c}='03 No Sensitization, Rolled Direction T, Bend
150MPa';
case '04.xlsx'
  n{c}='04 No Sensitization, Rolled Direction S, Bend
150MPa';
case '05.xlsx'
  n{c}='05 Friction Stir Weld, On Weld';
case '06.xlsx'
  n{c}='Control Friction Stir Weld Batch, No Laser
Peening, Not on Weld';
case '06a.xlsx'
  n{c}='06a Duplicate Control FSW';
case '06b.xlsx'
  n{c}='06b Duplicate Control FSW';
case '07.xlsx'
  n{c}='Laser Peened 1-18-1';
case '07a.xlsx'
  n{c}='07a Duplicate Laser Peened 1-18-1';
case '07b.xlsx'
  n{c}='07b Duplicate Laser Peened 1-18-1';
case '08.xlsx'
  n{c}='08 Laser Peened 1-18-2';
case '09.xlsx'
  n{c}='09 Laser Peened 1-27-1';
case '09a.xlsx'
  n{c}='09a Duplicate Laser Peened 1-27-1';
case '09b.xlsx'
  n{c}='09b Duplicate Laser Peened 1-27-1';
case '10.xlsx'
  n{c}='10 Laser Peened 1-27-2';
case '11.xlsx'
  n{c}='11 Laser Peened 3-18-1';
case '12.xlsx'
  n{c}='12 Laser Peened 3-18-2';
case '12a.xlsx'
  n{c}='12a Duplicate Laser Peened 3-18-2';
case '12b.xlsx'
  n{c}='12b Duplicate Laser Peened 3-18-2';
case '13.xlsx'
  n{c}='13 Laser Peened 3-27-1';
case '14.xlsx'
  n{c}='Laser Peened 3-27-2';
case '14a.xlsx'
  n{c}='14a Duplicate Laser Peened 3-27-2';
case '14b.xlsx'
  n{c}='14b Duplicate Laser Peened 3-27-2';
case '15.xlsx'

```

```

        n{c}='Sensitized 175deg/156hr, Rolled S Direction,
No Bend';
        case '16.xlsx'
        n{c}='Sensitized 175deg/156hr, Rolled T Direction,
No Bend';
        case '17.xlsx'
        n{c}='Sensitized 175 Degrees Celsius for 156 Hours,
Rolled S Direction, Bend 150MPa';
        case '18.xlsx'
        n{c}='Sensitized 175 Degrees Celsius for 156 Hours,
Rolled T Direction, Bend 150MPa';
        case '19.xlsx'
        n{c}='Sensitized 175deg/24hr, Rolled S Direction,
No Bend';
        case '20.xlsx'
        n{c}='20 Sensitized 175deg/24hr, Rolled T
Direction, No Bend';
        case '21.xlsx'
        n{c}='Sensitized 175deg/48hr, Rolled S Direction,
No Bend';
        case '22.xlsx'
        n{c}='22 Sensitized 175deg/48hr, Rolled T
Direction, No Bend';
        case '23.xlsx'
        n{c}='Sensitized 175deg/72hr, Rolled S Direction,
No Bend';
        case '24.xlsx'
        n{c}='24 Sensitized 175deg/72hr, Rolled T
Direction, No Bend';
        case '25.xlsx'
        n{c}='Sensitized 175deg/96hr, Rolled S Direction,
No Bend';
        case '26.xlsx'
        n{c}='26 Sensitized 175deg/96hr, Rolled T
Direction, No Bend';
        case '27.xlsx'
        n{c}='Sensitized 200 Degrees Celsius for 336 Hours,
Rolled S Direction, No Applied Tension';
        case '28.xlsx'
        n{c}='28 Sensitized 200deg/336hr, Rolled T
Direction, No Bend';
        case '29.xlsx'
        n{c}='Sensitized 200 Degrees Celsius for 336 Hours,
Rolled S Direction, Applied Tension of 150MPa';
        case '30.xlsx'
        n{c}='Sensitized 200 Degrees Celsius for 336 Hours,
Rolled T Direction, Applied Tension of 150MPa';
        otherwise
        n{c}=files(i).name(1:length(files(i).name)-5);
    end
    c=c+1;
end
end
end
end

```

```

s={'-', '+', 'o', 's', 'd'};

%%Data Plot
figure1 = figure;
axes1 = axes('Parent',figure1,'FontSize',18);
for i=1:ceil(size(cmp_files,2)/5)
    limlow=(i-1)*5+1;
    if(i==ceil(size(cmp_files,2)/5))
        limhigh=size(cmp_files,2);
    else
        limhigh=(i-1)*5+5;
    end

    semilogx(abs(amps(:,limlow:limhigh)),volts(:,limlow:limhigh),s{i},'Line
Width',2,'Parent',axes1)
    hold on;
end
ylabel('Potential, V_f (V vs E_R_e_f)
[Volts]','FontSize',30),xlabel('Log Current [Amps]','FontSize',30),grid
on,legend(n);
hold off;

cd('..');

```

## B. MATLAB CODE – ELECTRICAL IMPEDANCE SPECTROSCOPY: BODE AND NYQUIST PLOTS

```
%%MATLAB Code - Cyclic Polarization Curves
% For use in conjunction with output files from Gamry Framework™
software.
% Created by LT William Richard Fleming, USN
% Modified by LT Jennifer Sanders Fleming, USN
% Naval Postgraduate School, Monterey, CA
% 23 May, 2013

%% Acquire Data
clear;
%cd('\special\jasandel$\Desktop\Jennifer Sanders Thesis Data\');%for
school
cd('K:\Desktop\Jennifer Sanders Thesis Data') %for
home

EIS=1; % EIS Scan Number
switch EIS
    case 1
        cd('01JSF1EIS');
        cmp_files={'01b','02','06'};
    case 2
        cd('03JSF2EIS');
        cmp_files={'14','14a','14b'};
    case 3
        cd('05JSF3EIS');
        cmp_files={'21','23','25','27','29','30'};
    case 4
        cd('07JSF4EIS');
        cmp_files={'21','23','25','27','29','30'};
end

files = dir('*.xlsx');
freq=zeros(66,size(cmp_files,2));
zmod=zeros(66,size(cmp_files,2));
phase=zeros(66,size(cmp_files,2));
zreal=zeros(66,size(cmp_files,2));
zimag=zeros(66,size(cmp_files,2));
c=1;
for i = 1:length(files)
    for j = 1:size(cmp_files,2)
        if(strcmp(files(i).name(1:length(files(i).name)-
5),cmp_files{j}))
            f=xlsread(files(i).name,'D3:D68');
            o=xlsread(files(i).name,'H3:H68');
            p=xlsread(files(i).name,'I3:I68');
            re=xlsread(files(i).name,'E3:E68');
            im=xlsread(files(i).name,'F3:F68');
            freq(1:size(f,1),c)=f;
            zmod(1:size(o,1),c)=o;
            phase(1:size(o,1),c)=p;
            zreal(1:size(o,1),c)=re;
            zimag(1:size(o,1),c)=im;
        end
    end
end
```

```

switch files(i).name
  case '01.xlsx'
    n{c}='Control Rolled Direction T';
  case '01a.xlsx'
    n{c}='Control Rolled Direction T';
  case '01b.xlsx'
    n{c}='Control Rolled Direction T';
  case '02.xlsx'
    n{c}='Rolled Direction S';
  case '02a.xlsx'
    n{c}='Control Rolled Direction S';
  case '02b.xlsx'
    n{c}='Control Rolled Direction S';
  case '03.xlsx'
    n{c}='03 No Sensitization, Rolled Direction T, Bend
150MPa';
  case '04.xlsx'
    n{c}='04 No Sensitization, Rolled Direction S, Bend
150MPa';
  case '05.xlsx'
    n{c}='05 Friction Stir Weld, On Weld';
  case '06.xlsx'
    n{c}='Control from Friction Stir Weld Batch, No
Laser Peening, Not on Weld';
  case '06a.xlsx'
    n{c}='Control from Friction Stir Weld Batch, No
Laser Peening, Not on Weld';
  case '06b.xlsx'
    n{c}='Control from Friction Stir Weld Batch, No
Laser Peening, Not on Weld';
  case '07.xlsx'
    n{c}='07 Laser Peened 1-18-1';
  case '07a.xlsx'
    n{c}='07a Duplicate Laser Peened 1-18-1';
  case '07b.xlsx'
    n{c}='07b Duplicate Laser Peened 1-18-1';
  case '08.xlsx'
    n{c}='08 Laser Peened 1-18-2';
  case '09.xlsx'
    n{c}='09 Laser Peened 1-27-1';
  case '09a.xlsx'
    n{c}='09a Duplicate Laser Peened 1-27-1';
  case '09b.xlsx'
    n{c}='09b Duplicate Laser Peened 1-27-1';
  case '10.xlsx'
    n{c}='10 Laser Peened 1-27-2';
  case '11.xlsx'
    n{c}='11 Laser Peened 3-18-1';
  case '12.xlsx'
    n{c}='12 Laser Peened 3-18-2';
  case '12a.xlsx'
    n{c}='12a Duplicate Laser Peened 3-18-2';
  case '12b.xlsx'
    n{c}='12b Duplicate Laser Peened 3-18-2';
  case '13.xlsx'

```

```

        n{c}='13 Laser Peened 3-27-1';
    case '14.xlsx'
        n{c}='14 Laser Peened 3-27-2';
    case '14a.xlsx'
        n{c}='14a Duplicate Laser Peened 3-27-2';
    case '14b.xlsx'
        n{c}='14b Duplicate Laser Peened 3-27-2';
    case '15.xlsx'
        n{c}='Sensitized 175 Degrees Celsius for 156 Hours,
Rolled S Direction, No Bend';
    case '16.xlsx'
        n{c}='Sensitized 175 Degrees Celsius for 156 Hours,
Rolled T Direction, No Bend';
    case '17.xlsx'
        n{c}='Sensitized 175 Degrees Celsius for 156 Hours,
Rolled S Direction, Bend 150MPa';
    case '18.xlsx'
        n{c}='Sensitized 175 Degrees Celsius for 156 Hours,
Rolled T Direction, Bend 150MPa';
    case '19.xlsx'
        n{c}='Sensitized 175 Degrees Celsius for 24 Hours,
Rolled S Direction, No Bend';
    case '20.xlsx'
        n{c}='Sensitized 175 Degrees Celsius for 24 Hours,
Rolled T Direction, No Bend';
    case '21.xlsx'
        n{c}='Sensitized 175 Degrees Celsius for 48 Hours,
Rolled S Direction, No Bend';
    case '22.xlsx'
        n{c}='Sensitized 175 Degrees Celsius for 48 Hours,
Rolled T Direction, No Bend';
    case '23.xlsx'
        n{c}='Sensitized 175 Degrees Celsius for 72 Hours,
Rolled S Direction, No Bend';
    case '24.xlsx'
        n{c}='Sensitized 175 Degrees Celsius for 72 Hours,
Rolled T Direction, No Bend';
    case '25.xlsx'
        n{c}='Sensitized 175 Degrees Celsius for 96 Hours,
Rolled S Direction, No Bend';
    case '26.xlsx'
        n{c}='Sensitized 175 Degrees Celsius for 96 Hours,
Rolled T Direction, No Bend';
    case '27.xlsx'
        n{c}='Sensitized 200 Degrees Celsius for 336 Hours,
Rolled S Direction, No Bend';
    case '28.xlsx'
        n{c}='Sensitized 200 Degrees Celsius for 336 Hours,
Rolled T Direction, No Bend';
    case '29.xlsx'
        n{c}='Sensitized 200 Degrees Celsius for 336 Hours,
Rolled S Direction, Bend 150MPa';
    case '30.xlsx'
        n{c}='Sensitized 200 Degrees Celsius for 336 Hours,
Rolled T Direction, Bend 150MPa';

```

```

                otherwise
                    n{c}=files(i).name(1:length(files(i).name)-5);
            end
            c=c+1;
        end
    end
end

s={'-', '+', 'o', 's', 'd'};

%% Data Plot: Frequency vs Zmod
figure1 = figure;
axes1 = axes('Parent',figure1,'FontSize',18);
for i=1:ceil(size(cmp_files,2)/5)
    limlow=(i-1)*5+1;
    if(i==ceil(size(cmp_files,2)/5))
        limhigh=size(cmp_files,2);
    else
        limhigh=(i-1)*5+5;
    end

    loglog((abs(freq(:,limlow:limhigh))), (abs(zmod(:,limlow:limhigh))), s{i}
    , ...
        'LineWidth', 2, 'Parent', axes1);
    hold on;
end
ylabel('Zmod [Ohms]', 'FontSize', 30), xlabel('Frequency
[Hertz]', 'FontSize', 30), grid on, legend(n);
hold off;

%% %% freq vs phase
% figure1 = figure;
% axes1 = axes('Parent',figure1,'FontSize',18);
% for i=1:ceil(size(cmp_files,2)/5)
%     limlow=(i-1)*5+1;
%     if(i==ceil(size(cmp_files,2)/5))
%         limhigh=size(cmp_files,2);
%     else
%         limhigh=(i-1)*5+5;
%     end
% end
% semilogx((abs(freq(:,limlow:limhigh))), (phase(:,limlow:limhigh)), s{i}, .
. .
%     'LineWidth', 2, 'Parent', axes1);
%     hold on;
% end
% ylabel('Degrees', 'FontSize', 18), xlabel('Hertz', 'FontSize', 18), grid
on, legend(n);
% hold off;
%
% %% real vs imag
% figure1 = figure;
% axes1 = axes('Parent',figure1,'FontSize',18);
% for i=1:ceil(size(cmp_files,2)/5)
%     limlow=(i-1)*5+1;

```

```

%     if(i==ceil(size(cmp_files,2)/5))
%         limhigh=size(cmp_files,2);
%     else
%         limhigh=(i-1)*5+5;
%     end
%
%
plot((abs(zreal(:,limlow:limhigh))),abs(zimag(:,limlow:limhigh)),s{i},.
    ..
%         'LineWidth',2,'Parent',axes1);
%     hold on;
% end
% ylabel('Real','FontSize',18),xlabel('Imag','FontSize',18),grid
on,legend(n);
% hold off;

cd('...');

```

### C. SAMPLE CONDITIONS

Sample	Rolled Direction	Laser			Temperature [°C]	Time [hours]	Bend Stress [MPa]
		Irradiance [GW/cm <sup>2</sup> ]	Pulse Width	No. of Passes			
1	L-T	0	0	0	0	0	0
1a	L-T	0	0	0	0	0	0
1b	L-T	0	0	0	0	0	0
2	L-S	0	0	0	0	0	0
2a	L-S	0	0	0	0	0	0
2b	L-S	0	0	0	0	0	0
3	L-T	0	0	0	0	0	150
4	L-S	0	0	0	0	0	150
5	NA	0	0	0	0	0	0
6	NA	0	0	0	0	0	0
6a	NA	0	0	0	0	0	0
6b	NA	0	0	0	0	0	0
7	NA	1	18	1	0	0	0
7a	NA	1	18	1	0	0	0
7b	NA	1	18	1	0	0	0
8	NA	1	18	2	0	0	0
9	NA	1	27	1	0	0	0
9a	NA	1	27	1	0	0	0
9b	NA	1	27	1	0	0	0
10	NA	1	27	2	0	0	0
11	NA	3	18	1	0	0	0
12	NA	3	18	2	0	0	0
12a	NA	3	18	2	0	0	0
12b	NA	3	18	2	0	0	0
13	NA	3	27	1	0	0	0
14	NA	3	27	2	0	0	0
14a	NA	3	27	2	0	0	0
14b	NA	3	27	2	0	0	0
15	L-S	0	0	0	175	156	0
16	L-T	0	0	0	175	156	0
17	L-S	0	0	0	175	156	150
18	L-T	0	0	0	175	156	150
19	L-S	0	0	0	175	24	0
21	L-S	0	0	0	175	48	0
23	L-S	0	0	0	175	72	0
25	L-S	0	0	0	175	96	0
27	L-S	0	0	0	200	336	0
28	L-T	0	0	0	200	336	0
29	L-S	0	0	0	200	336	150
30	L-T	0	0	0	200	336	150

Table 7. Full sample list with conditions applied.

#### D. CYCLIC POLARIZATION DATA

Sample	Cyclic Polarization Scan 1						
	Corrosion Potential		Breakdown	Repassivation		$\Delta E$	
	$i_{CORR}$ A	$E_{CORR}$ V	$E_{CRIT}$ V	$i_p$ A	$E_{RP}$ V	$\Delta E_{CRIT}$ V	$\Delta E_{RP}$ V
1	4.7120E-06	-6.6090E-01	0.0000E+00	6.4990E-06	-8.4480E-01	6.6090E-01	-1.8390E-01
1a	3.9300E-08	-8.3580E-01	0.0000E+00	7.3410E-06	-8.0400E-01	8.3580E-01	3.1800E-02
1b	2.1950E-07	-7.5160E-01	0.0000E+00	1.0300E-06	-9.1240E-01	7.5160E-01	-1.6080E-01
2	9.5630E-07	-7.4700E-01	0.0000E+00	1.8950E-06	-8.8180E-01	7.4700E-01	-1.3480E-01
2a	9.9120E-08	-7.2090E-01	0.0000E+00	2.6110E-05	-7.7670E-01	7.2090E-01	-5.5800E-02
2b	1.5930E-07	-7.5520E-01	0.0000E+00	1.5310E-06	-8.6410E-01	7.5520E-01	-1.0890E-01
3	2.0700E-09	-6.5700E-01	0.0000E+00	1.3250E-06	-8.4690E-01	6.5700E-01	-1.8990E-01
4	3.8420E-07	-6.9870E-01	0.0000E+00	1.1500E-06	-8.3360E-01	6.9870E-01	-1.3490E-01
5	3.1210E-07	-7.8550E-01	0.0000E+00	4.4760E-06	-8.7490E-01	7.8550E-01	-8.9400E-02
6	5.4780E-07	-7.4990E-01	0.0000E+00	2.4110E-06	-8.9660E-01	7.4990E-01	-1.4670E-01
6a	1.2400E-06	-5.9210E-01	0.0000E+00	2.8610E-06	-8.7900E-01	5.9210E-01	-2.8690E-01
6b	1.8730E-06	-7.2280E-01	0.0000E+00	2.9580E-06	-8.9580E-01	7.2280E-01	-1.7300E-01
7	1.2630E-08	-9.7490E-01	-7.5000E-01	4.9320E-06	-8.7600E-01	2.2490E-01	9.8900E-02
7a	7.5020E-08	-7.2810E-01	0.0000E+00	8.7730E-07	-8.8610E-01	7.2810E-01	-1.5800E-01
7b	3.2350E-08	-9.2520E-01	-7.5730E-01	1.0310E-05	-8.3280E-01	1.6790E-01	9.2400E-02
8	3.6960E-08	-8.8820E-01	0.0000E+00	3.3650E-06	-8.5930E-01	8.8820E-01	2.8900E-02
9	5.4860E-09	-9.1410E-01	0.0000E+00	2.0890E-06	-8.9780E-01	9.1410E-01	1.6300E-02
9a	8.8770E-11	-6.8870E-01	0.0000E+00	3.9200E-07	-8.9150E-01	6.8870E-01	-2.0280E-01
9b	2.2480E-07	-9.9770E-01	-7.6590E-01	8.9670E-05	-8.0190E-01	2.3180E-01	1.9580E-01
10	2.5510E-07	-5.8680E-01	0.0000E+00	6.9830E-07	-8.9510E-01	5.8680E-01	-3.0830E-01
11	5.3040E-08	-9.0600E-01	0.0000E+00	2.8030E-06	-8.8500E-01	9.0600E-01	2.1000E-02
12	3.8800E-09	-7.1730E-01	0.0000E+00	6.0430E-07	-9.2520E-01	7.1730E-01	-2.0790E-01
12a	4.8340E-09	-9.1530E-01	-6.1550E-01	3.3730E-07	-9.1130E-01	2.9980E-01	4.0000E-03
12b	5.8990E-09	-6.6670E-01	0.0000E+00	1.0190E-06	-9.2450E-01	6.6670E-01	-2.5780E-01
13	8.0040E-10	-9.0130E-01	-7.3250E-01	5.3050E-07	-8.6630E-01	1.6880E-01	3.5000E-02
14	4.2860E-08	-8.9750E-01	-5.8720E-01	6.6910E-07	-8.9000E-01	3.1030E-01	7.5000E-03
14a	1.0370E-07	-7.4180E-01	0.0000E+00	6.9630E-07	-8.9020E-01	7.4180E-01	-1.4840E-01
14b	4.5560E-09	-8.3830E-01	-6.9730E-01	4.0130E-07	-9.0520E-01	1.4100E-01	-6.6900E-02
15	2.5230E-07	-8.2840E-01	0.0000E+00	3.1410E-06	-8.2090E-01	8.2840E-01	7.5000E-03
16	6.6000E-07	-6.7050E-01	0.0000E+00	1.9580E-06	-8.4840E-01	6.7050E-01	-1.7790E-01
17	4.8820E-08	-8.2350E-01	0.0000E+00	4.4580E-06	-8.1240E-01	8.2350E-01	1.1100E-02
18	9.9480E-08	-8.4060E-01	0.0000E+00	3.6390E-06	-8.3060E-01	8.4060E-01	1.0000E-02
19	2.5000E-08	-7.6620E-01	0.0000E+00	1.3920E-06	-8.5110E-01	7.6620E-01	-8.4900E-02
21	1.1680E-07	-7.2600E-01	0.0000E+00	1.2500E-06	-8.6590E-01	7.2600E-01	-1.3990E-01
23	3.0750E-07	-7.3310E-01	0.0000E+00	1.1600E-06	-8.8790E-01	7.3310E-01	-1.5480E-01
25	1.1030E-07	-7.3840E-01	0.0000E+00	3.3080E-06	-8.4190E-01	7.3840E-01	-1.0350E-01
27	2.6240E-07	-7.4850E-01	0.0000E+00	2.0020E-06	-8.3940E-01	7.4850E-01	-9.0900E-02
29	3.6700E-07	-7.4920E-01	0.0000E+00	1.2410E-06	-8.3520E-01	7.4920E-01	-8.6000E-02
30	6.0750E-07	-7.6510E-01	0.0000E+00	1.6650E-06	-8.2990E-01	7.6510E-01	-6.4800E-02

Table 8. CP data for all samples scan 1.

Sample	Cyclic Polarization Scan 2						
	Corrosion Potential		Breakdown	Repassivation		ΔE	
	$i_{CORR}$	$E_{CORR}$	$E_{CRIT}$	$i_P$	$E_{RP}$	$\Delta E_{CRIT}$	$\Delta E_{RP}$
	A	V	V	A	V	V	V
1	1.5850E-08	-9.7140E-01	-7.1050E-01	2.7270E-06	-7.9540E-01	2.6090E-01	1.7600E-01
1a	6.6590E-09	-1.0660E+00	-7.3300E-01	7.5900E-06	-8.1040E-01	3.3300E-01	2.5560E-01
1b	9.2290E-09	-1.0200E+00	-7.6280E-01	4.3270E-06	-8.5270E-01	2.5720E-01	1.6730E-01
2	1.6700E-08	-1.1280E+00	-7.2520E-01	5.2040E-06	-8.0980E-01	4.0280E-01	3.1820E-01
2a	1.2580E-08	-8.5620E-01	-7.2920E-01	2.0560E-06	-7.8630E-01	1.2700E-01	6.9900E-02
2b	1.7920E-08	-1.1400E+00	-7.2770E-01	7.6630E-06	-8.0080E-01	4.1230E-01	3.3920E-01
3	1.2780E-08	-9.8660E-01	-7.4400E-01	3.6350E-06	-8.1560E-01	2.4260E-01	1.7100E-01
4	3.7610E-09	-9.9070E-01	-7.4290E-01	3.8780E-06	-8.2000E-01	2.4780E-01	1.7070E-01
5	4.9240E-09	-9.2910E-01	-7.5520E-01	3.0730E-06	-8.7010E-01	1.7390E-01	5.9000E-02
6	2.5090E-10	-9.8500E-01	-7.6300E-01	2.1900E-06	-8.6920E-01	2.2200E-01	1.1580E-01
6a	2.0880E-08	-9.5810E-01	-7.4740E-01	4.4390E-06	-8.6430E-01	2.1070E-01	9.3800E-02
6b	4.5090E-09	-9.5180E-01	-7.6480E-01	2.4390E-06	-9.0430E-01	1.8700E-01	4.7500E-02
7	3.3860E-09	-1.1060E+00	-7.2660E-01	5.0080E-06	-8.1820E-01	3.7940E-01	2.8780E-01
7a	7.6360E-09	-1.0000E+00	-7.4330E-01	1.7720E-06	-8.4030E-01	2.5670E-01	1.5970E-01
7b	1.8950E-08	-1.0890E+00	-7.3150E-01	7.8720E-06	-7.9450E-01	3.5750E-01	2.9450E-01
8	1.0700E-08	-9.6020E-01	-7.5330E-01	9.3570E-06	-8.3930E-01	2.0690E-01	1.2090E-01
9	1.0010E-08	-1.0700E+00	-7.3460E-01	1.6390E-06	-8.5550E-01	3.3540E-01	2.1450E-01
9a	3.8940E-08	-9.7010E-01	-7.6330E-01	1.0230E-05	-8.4220E-01	2.0680E-01	1.2790E-01
9b	6.0910E-08	-1.1960E+00	-7.3880E-01	1.7410E-05	-7.7580E-01	4.5720E-01	4.2020E-01
10	1.8200E-08	-9.7060E-01	-7.4470E-01	5.2150E-06	-8.6570E-01	2.2590E-01	1.0490E-01
11	1.4840E-08	-9.6710E-01	-7.5120E-01	5.8290E-06	-8.7260E-01	2.1590E-01	9.4500E-02
12	3.5510E-09	-9.4370E-01	-7.5570E-01	1.6740E-06	-8.7080E-01	1.8800E-01	7.2900E-02
12a	5.0060E-09	-1.1150E+00	-7.1960E-01	2.3300E-06	-8.4750E-01	3.9540E-01	2.6750E-01
12b	1.7270E-08	-9.1780E-01	-7.5890E-01	9.7180E-07	-8.9590E-01	1.5890E-01	2.1900E-02
13	6.9150E-08	-1.1470E+00	-7.4230E-01	9.1710E-06	-7.9530E-01	4.0470E-01	3.5170E-01
14	1.3140E-08	-1.1460E+00	-7.0360E-01	2.2460E-06	-8.2540E-01	4.4240E-01	3.2060E-01
14a	7.3140E-09	-9.2570E-01	-7.4200E-01	1.9630E-06	-8.7000E-01	1.8370E-01	5.5700E-02
14b	1.4990E-08	-9.0230E-01	-7.6050E-01	1.2040E-06	-8.8040E-01	1.4180E-01	2.1900E-02
15	3.7960E-08	-1.1170E+00	-7.0630E-01	4.3580E-06	-7.7630E-01	4.1070E-01	3.4070E-01
16	7.6170E-09	-1.1800E+00	-7.0470E-01	4.7650E-06	-7.7860E-01	4.7530E-01	4.0140E-01
17	5.0860E-09	-9.3520E-01	-7.5430E-01	2.7470E-06	-7.8840E-01	1.8090E-01	1.4680E-01
18	5.2560E-09	-1.0630E+00	-7.1300E-01	2.5470E-06	-7.7510E-01	3.5000E-01	2.8790E-01
19	8.8910E-09	-1.1160E+00	-7.3870E-01	5.0380E-06	-8.0370E-01	3.7730E-01	3.1230E-01
21	1.9510E-08	-1.1320E+00	-7.3040E-01	4.6820E-06	-7.9940E-01	4.0160E-01	3.3260E-01
23	2.7310E-09	-1.1370E+00	-7.4510E-01	3.9800E-06	-8.1900E-01	3.9190E-01	3.1800E-01
25	3.7440E-08	-1.1100E+00	-7.3350E-01	4.1650E-06	-8.2230E-01	3.7650E-01	2.8770E-01
27	2.6690E-09	-9.3320E-01	-7.6330E-01	3.5670E-06	-7.9220E-01	1.6990E-01	1.4100E-01
29	1.4670E-08	-9.9810E-01	-7.5630E-01	4.5040E-06	-7.9220E-01	2.4180E-01	2.0590E-01
30	7.7710E-09	-1.0580E+00	-7.4560E-01	5.6700E-06	-7.9260E-01	3.1240E-01	2.6540E-01

Table 9. CP data for all samples scan 2.

Sample	Cyclic Polarization Scan 3						
	Corrosion Potential		Breakdown	Repassivation		$\Delta E$	
	$i_{CORR}$	$E_{CORR}$	$E_{CRIT}$	$i_P$	$E_{RP}$	$\Delta E_{CRIT}$	$\Delta E_{RP}$
A	V	V	A	V	V	V	
1	1.3340E-07	-1.1410E+00	-7.4100E-01	1.1370E-05	-7.7690E-01	4.0000E-01	3.6410E-01
1a	6.8820E-08	-1.1080E+00	-7.5070E-01	1.1680E-05	-8.1450E-01	3.5730E-01	2.9350E-01
1b	1.6400E-08	-1.1010E+00	-7.5860E-01	7.8780E-06	-8.1270E-01	3.4240E-01	2.8830E-01
2	9.4910E-08	-1.1370E+00	-7.5440E-01	8.5340E-06	-8.0750E-01	3.8260E-01	3.2950E-01
2a	1.2860E-08	-9.6780E-01	-7.5490E-01	5.3540E-06	-7.9280E-01	2.1290E-01	1.7500E-01
2b	3.5170E-08	-1.1280E+00	-7.3660E-01	8.5060E-06	-7.9050E-01	3.9140E-01	3.3750E-01
3	2.9490E-08	-1.1010E+00	-7.5480E-01	6.8660E-06	-8.0690E-01	3.4620E-01	2.9410E-01
4	8.8690E-08	-1.1440E+00	-7.3610E-01	1.0260E-05	-7.9130E-01	4.0790E-01	3.5270E-01
5	1.8120E-08	-1.1210E+00	-7.5120E-01	5.3500E-06	-7.9510E-01	3.6980E-01	3.2590E-01
6	7.2510E-09	-1.1350E+00	-7.4320E-01	6.4350E-06	-8.2820E-01	3.9180E-01	3.0680E-01
6a	2.0110E-08	-1.1240E+00	-7.2200E-01	5.6750E-06	-7.7800E-01	4.0200E-01	3.4600E-01
6b	2.1090E-09	-1.1700E+00	-7.5390E-01	6.6660E-06	-8.2180E-01	4.1610E-01	3.4820E-01
7	1.1560E-09	-9.0490E-01	-7.2720E-01	1.4620E-06	-8.5110E-01	1.7770E-01	5.3800E-02
7a	1.8160E-09	-9.1620E-01	-7.1740E-01	2.1290E-07	-8.5330E-01	1.9880E-01	6.2900E-02
7b	1.1610E-09	-8.5610E-01	-7.5420E-01	1.9750E-06	-8.3230E-01	1.0190E-01	2.3800E-02
8	2.3140E-09	-1.1460E+00	-7.2890E-01	5.4570E-06	-8.0380E-01	4.1710E-01	3.4220E-01
9	1.3260E-07	-1.1720E+00	-7.2030E-01	1.0520E-05	-8.0830E-01	4.5170E-01	3.6370E-01
9a	2.0870E-08	-9.6170E-01	-7.6090E-01	2.2180E-05	-8.1380E-01	2.0080E-01	1.4790E-01
9b	2.5010E-09	-1.0130E+00	-7.3080E-01	1.3140E-05	-7.8170E-01	2.8220E-01	2.3130E-01
10	5.1970E-08	-1.1900E+00	-7.2220E-01	6.6990E-06	-7.9910E-01	4.6780E-01	3.9090E-01
11	1.4160E-09	-1.1210E+00	-7.3320E-01	6.3380E-06	-8.0730E-01	3.8780E-01	3.1370E-01
12	2.0860E-08	-1.0810E+00	-7.2720E-01	6.7630E-06	-8.2570E-01	3.5380E-01	2.5530E-01
12a	9.7800E-08	-1.1640E+00	-7.3400E-01	1.0380E-05	-7.9180E-01	4.3000E-01	3.7220E-01
12b	6.5210E-09	-9.4490E-01	-7.5310E-01	1.9340E-06	-8.6210E-01	1.9180E-01	8.2800E-02
13	1.7090E-07	-1.2080E+00	-7.2730E-01	1.2280E-05	-7.8430E-01	4.8070E-01	4.2370E-01
14	6.4120E-08	-1.1430E+00	-7.2120E-01	8.8870E-06	-7.8570E-01	4.2180E-01	3.5730E-01
14a	1.4710E-09	-9.5120E-01	-7.2840E-01	3.2160E-07	-8.4830E-01	2.2280E-01	1.0290E-01
14b	3.6870E-08	-1.1530E+00	-7.2370E-01	5.2980E-06	-8.0360E-01	4.2930E-01	3.4940E-01
15	3.6280E-08	-1.1460E+00	-7.2420E-01	1.1690E-05	-7.6530E-01	4.2180E-01	3.8070E-01
16	2.9610E-08	-1.1520E+00	-7.1980E-01	7.8190E-06	-7.6970E-01	4.3220E-01	3.8230E-01
17	9.6140E-09	-1.0720E+00	-7.6170E-01	6.8270E-06	-7.7960E-01	3.1030E-01	2.9240E-01
18	5.3160E-09	-1.0650E+00	-7.4170E-01	3.8760E-06	-7.7460E-01	3.2330E-01	2.9040E-01
19	2.5080E-08	-1.0640E+00	-7.4410E-01	5.1190E-06	-7.9210E-01	3.1990E-01	2.7190E-01
21	2.1320E-08	-1.0840E+00	-7.2520E-01	4.8430E-06	-7.9710E-01	3.5880E-01	2.8690E-01
23	1.8910E-08	-1.0730E+00	-7.3850E-01	3.4160E-06	-8.0750E-01	3.3450E-01	2.6550E-01
25	4.1530E-08	-1.1330E+00	-7.2710E-01	5.0400E-06	-7.8600E-01	4.0590E-01	3.4700E-01
27	8.0910E-09	-9.8140E-01	-7.6250E-01	4.9720E-06	-7.8950E-01	2.1890E-01	1.9190E-01
29	8.4910E-09	-1.0950E+00	-7.5830E-01	6.5420E-06	-7.8630E-01	3.3670E-01	3.0870E-01
30	3.4110E-08	-1.0670E+00	-7.5220E-01	6.5970E-06	-7.8820E-01	3.1480E-01	2.7880E-01

Table 10. CP data for all samples scan 3.

1. Supplemental Cyclic Polarization Comparison Charts for Sensitized Samples

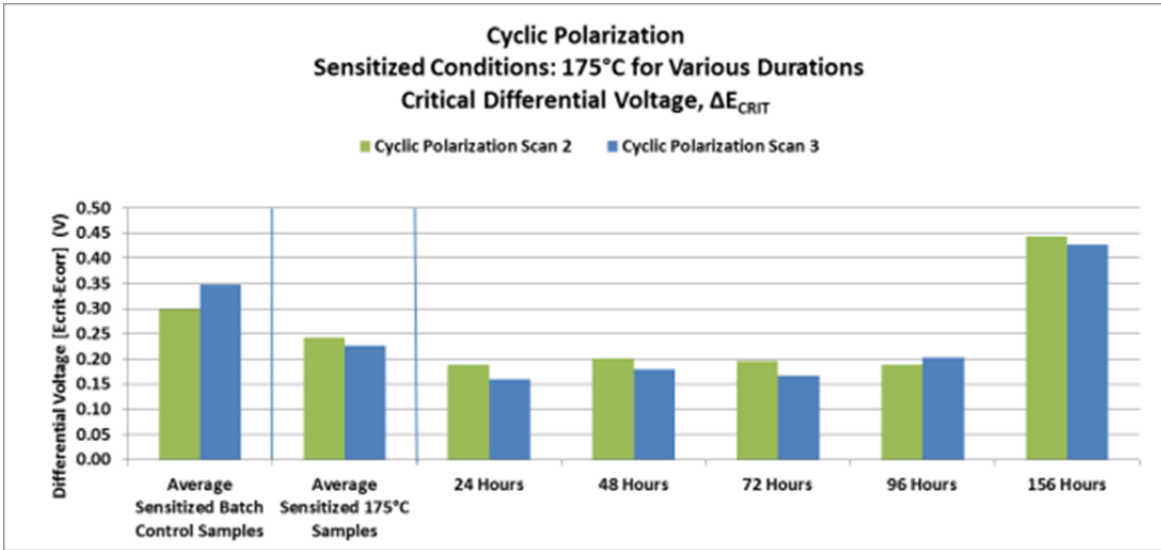


Figure 51. CP sensitized conditions: 175°C for various durations, scans 2–3 comparison of  $\Delta E_{CRIT}$ .

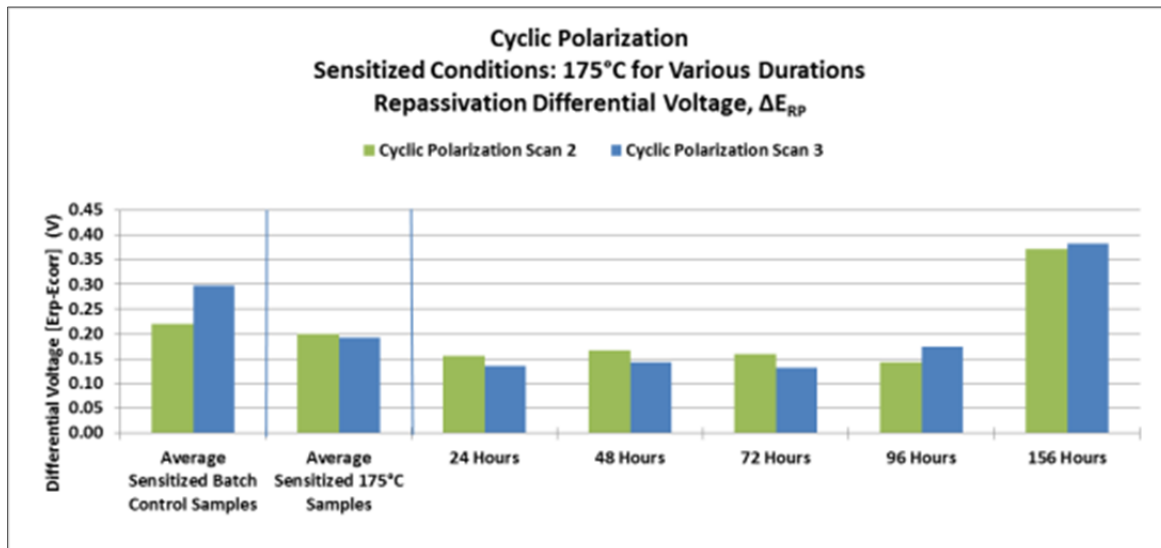


Figure 52. CP sensitized conditions: 175°C for various durations, Scans 2–3 comparison of  $\Delta E_{RP}$ .

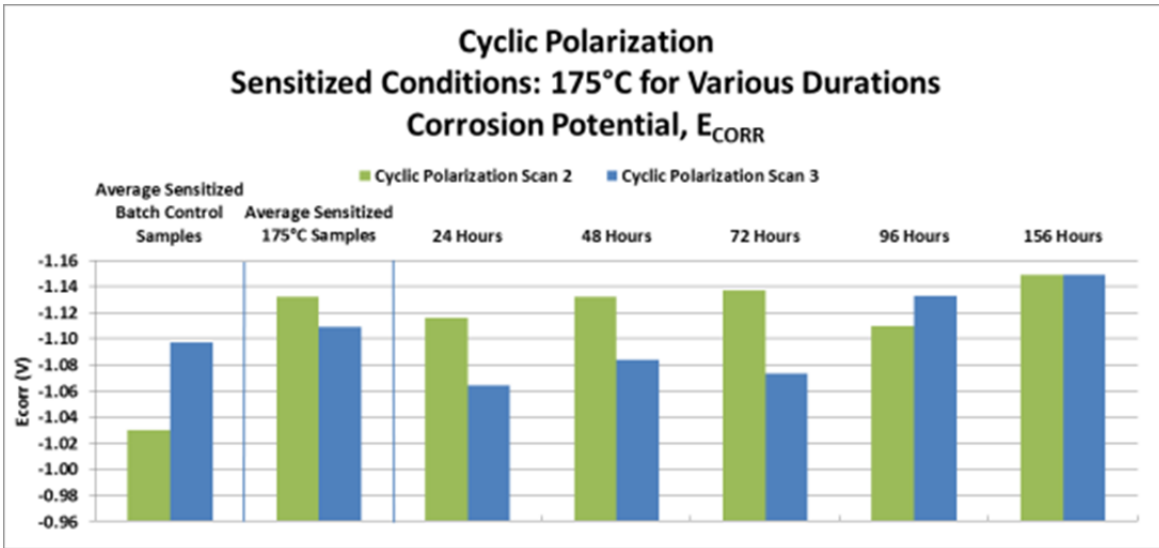


Figure 53. CP sensitized conditions: 175°C for various durations, scans 2–3 comparison of  $E_{CORR}$ .

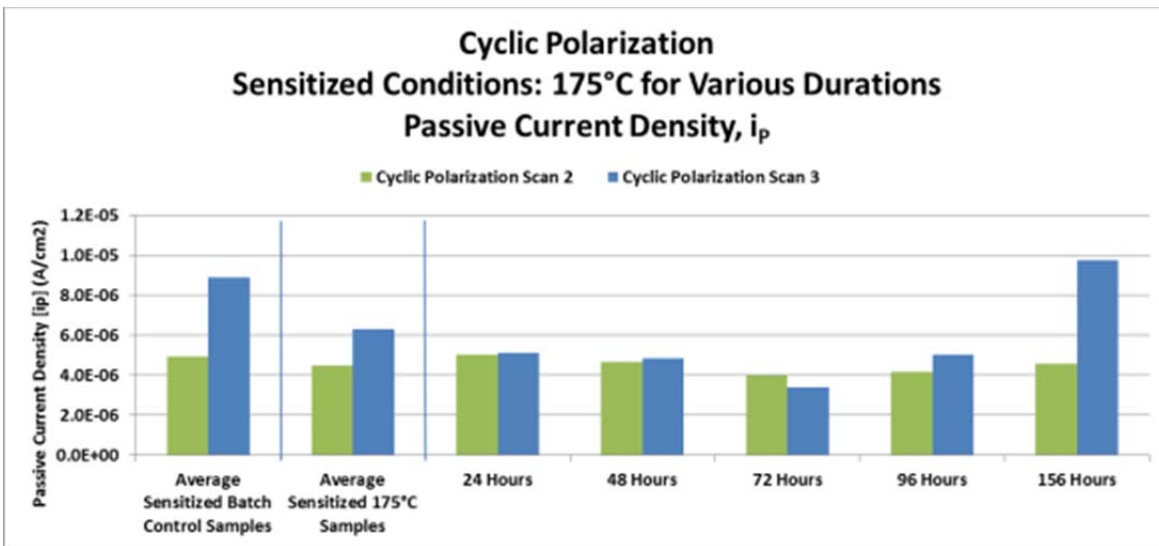


Figure 54. CP sensitized conditions: 175°C for various durations, scans 2–3 comparison of  $i_p$ .

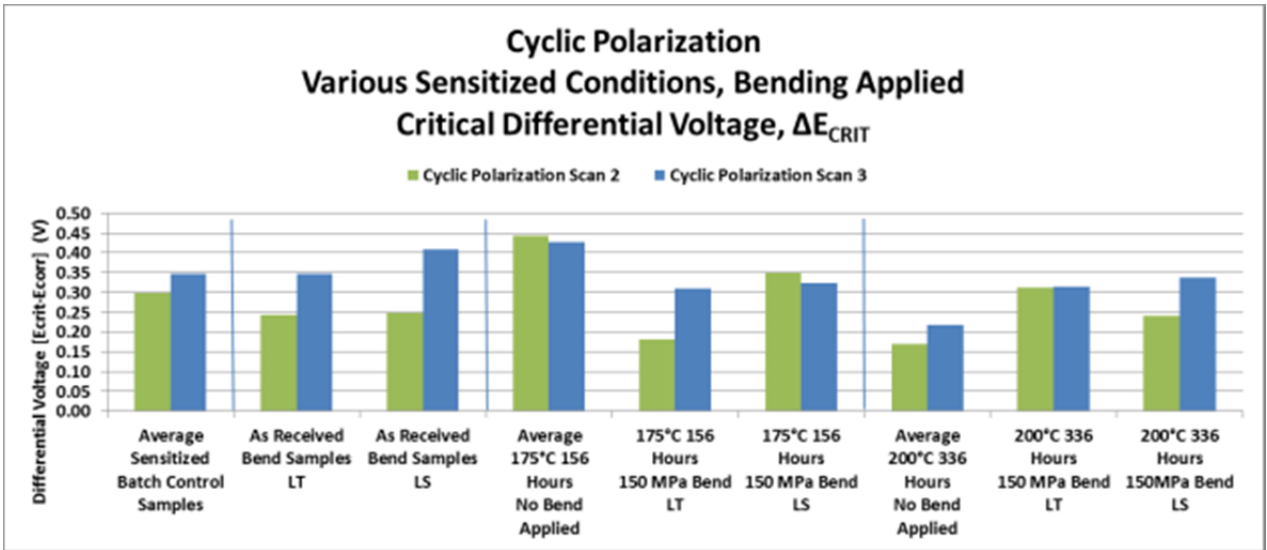


Figure 55. CP sensitized conditions: various sensitized conditions, bending applied, scans 2–3 comparison of  $\Delta E_{CRIT}$ .

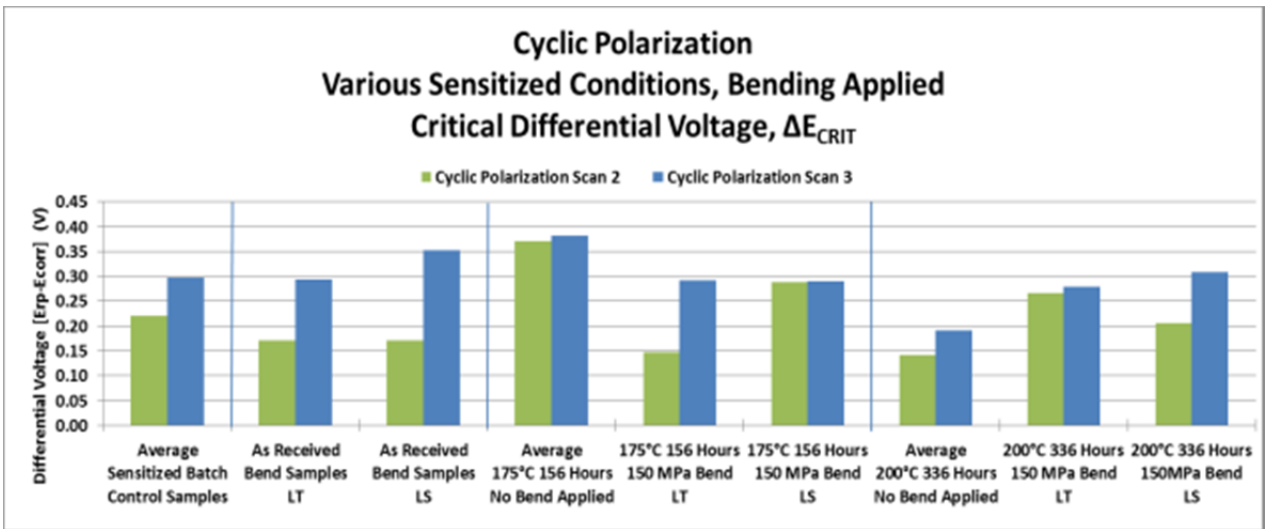


Figure 56. CP sensitized conditions: various sensitized conditions, bending applied, scans 2–3 comparison of  $\Delta E_{CRIT}$ .

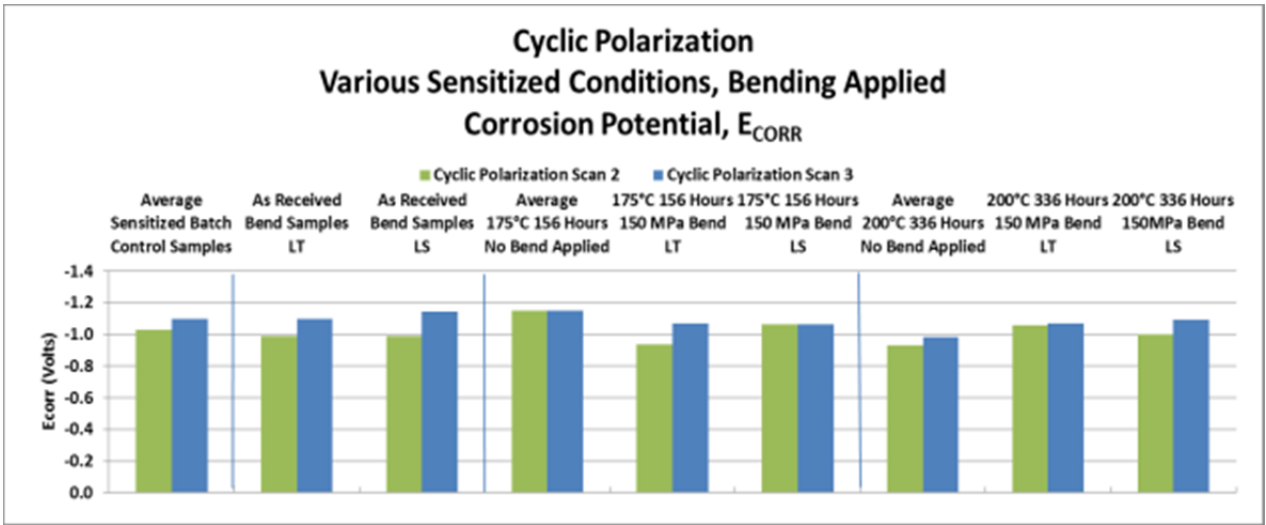


Figure 57. CP sensitized conditions: various sensitized conditions, bending applied, scans 2–3 comparison of  $E_{CORR}$ .

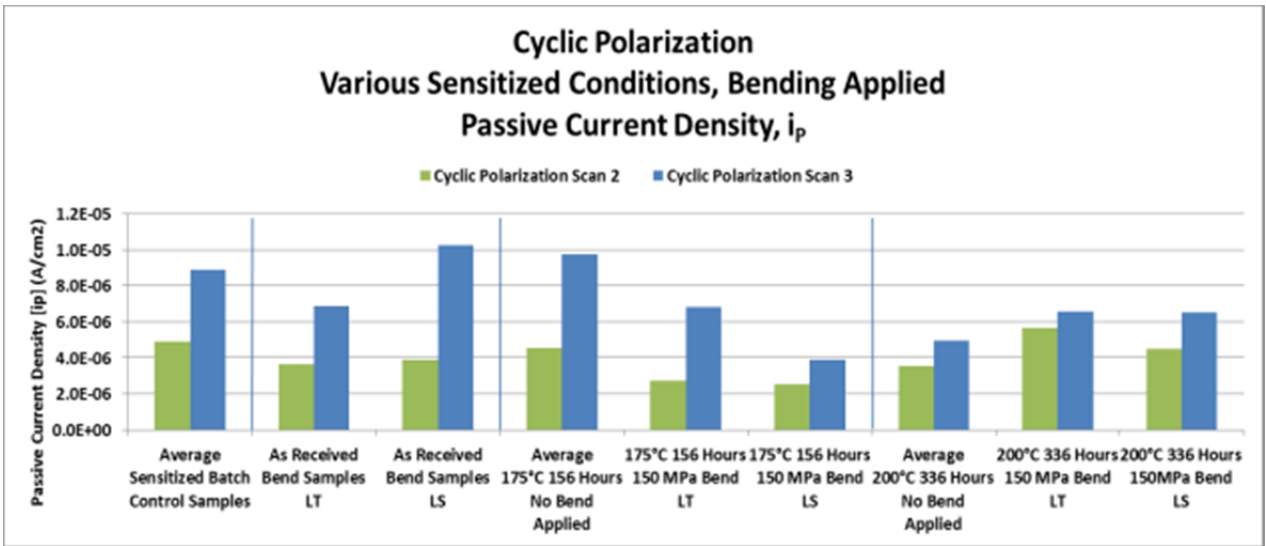


Figure 58. CP sensitized conditions: various sensitized conditions, bending applied, scans 2–3 comparison of  $i_p$ .

2. Supplemental Cyclic Polarization Comparison Charts for Laser Peened Samples

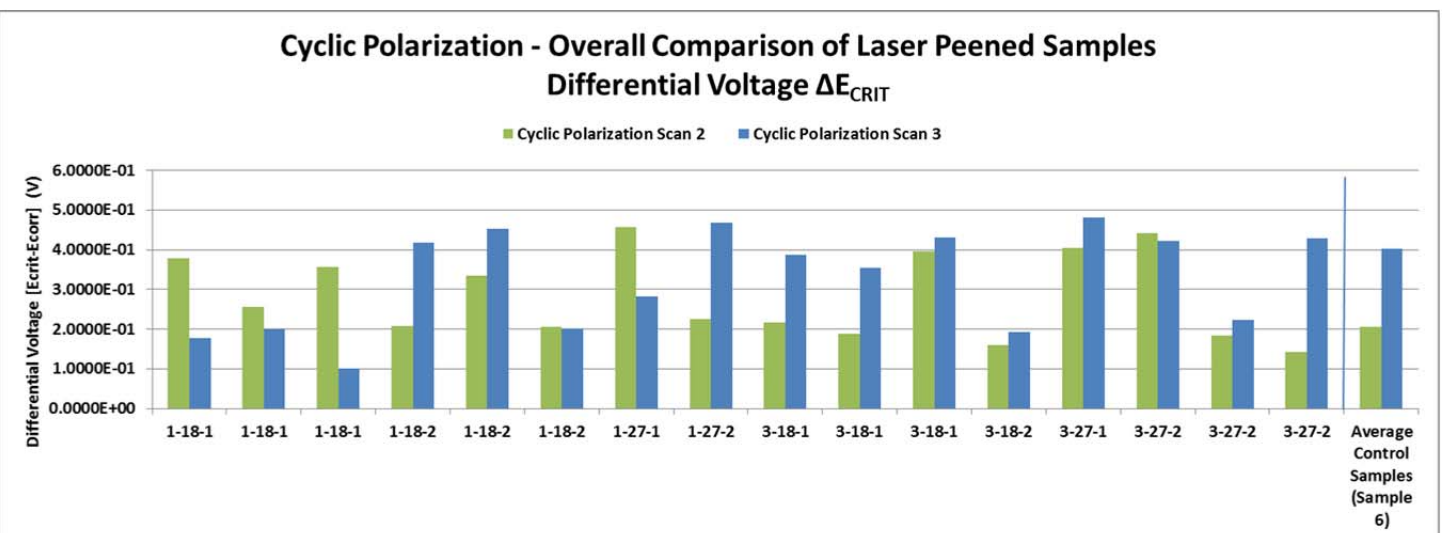
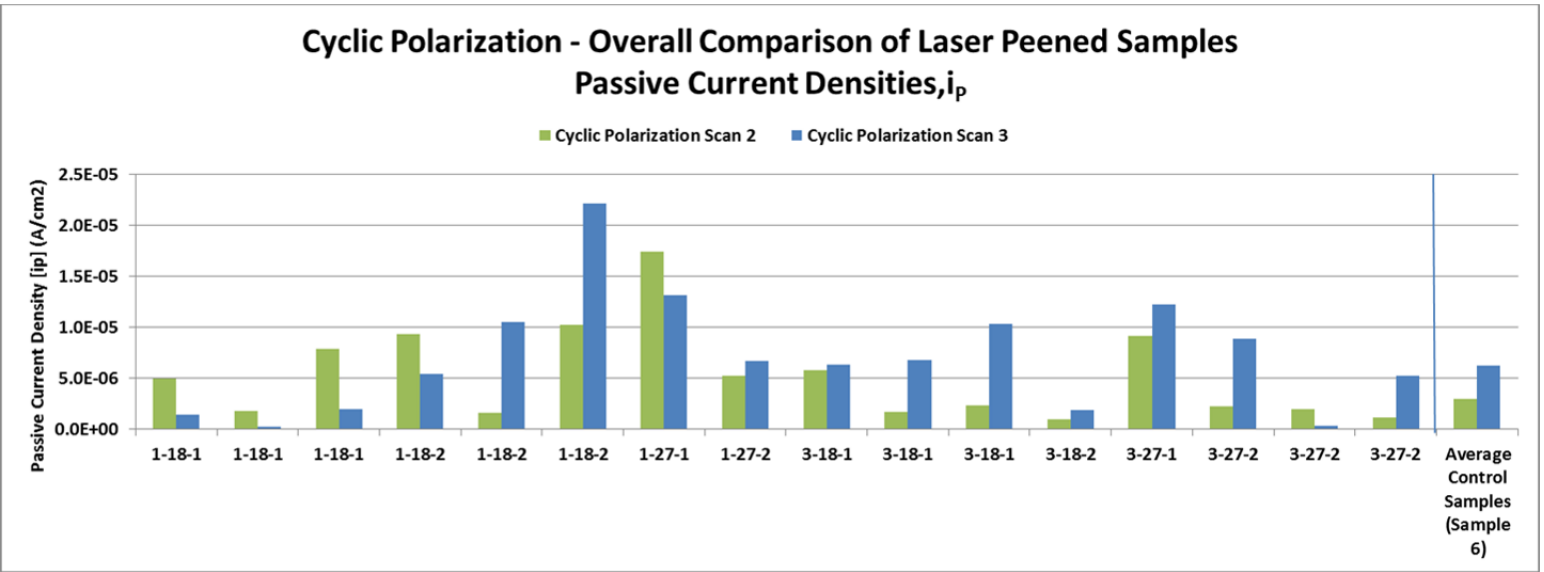


Figure 59. CP various laser peened conditions scans 2–3 comparison of  $\Delta E_{CRIT}$ .



Figure 61. CP various laser peened conditions scans 2–3 comparison of  $i_p$ .



**E. ELECTRICAL IMPEDENCE SPECTROSCOPY DATA**

	Electrical Impedance Spectroscopy Scan 1		
	Impedance at 0.1 Hz		
Sample	Rs	Rp	Rs+Rp
	Ohm	Ohm	Ohm
1	8.2180E+00	5.4868E+03	5.4950E+03
1a	7.9130E+00	6.4270E+00	1.4340E+01
1b	7.0620E+00	3.3389E+03	3.3460E+03
2	6.6920E+00	8.8883E+04	8.8890E+04
2a	1.0110E+01	2.7190E+04	2.7200E+04
2b	8.0780E+00	1.1009E+05	1.1010E+05
3	7.3710E+00	2.5559E+05	2.5560E+05
4	7.9430E+00	3.7929E+05	3.7930E+05
5	8.9230E+00	8.0841E+04	8.0850E+04
6	9.6260E+00	5.6504E+03	5.6600E+03
6a	1.0220E+01	8.8629E+05	8.8630E+05
6b	9.0060E+00	1.5941E+04	1.5950E+04
7	8.4000E+00	4.1190E+01	4.9590E+01
7a	8.8720E+00	6.4669E+05	6.4670E+05
7b	1.0030E+01	1.1650E+03	1.1750E+03
8	9.5310E+00	1.3710E+04	1.3720E+04
9	8.5440E+00	5.2379E+05	5.2380E+05
9a	8.9010E+00	7.1789E+05	7.1790E+05
9b	8.8270E+00	4.7317E+02	4.8200E+02
10	8.1460E+00	1.2049E+05	1.2050E+05
11	9.3290E+00	1.5569E+05	1.5570E+05
12	8.6240E+00	7.3779E+05	7.3780E+05
12a	9.3310E+00	7.3879E+05	7.3880E+05
12b	8.5960E+00	6.6529E+05	6.6530E+05
13	7.3890E+00	2.8921E+01	3.6310E+01
14	8.9670E+00	7.6919E+05	7.6920E+05
14a	9.0600E+00	4.8449E+05	4.8450E+05
14b	7.4710E+00	4.2449E+05	4.2450E+05
15	8.6720E+00	1.0449E+05	1.0450E+05
16	9.4070E+00	3.2159E+05	3.2160E+05
17	8.9330E+00	5.0721E+04	5.0730E+04
18	8.3840E+00	1.6949E+05	1.6950E+05
19	7.2050E+00	5.1360E+02	5.2080E+02
21	6.9710E+00	1.3069E+05	1.3070E+05
23	6.5960E+00	1.0909E+05	1.0910E+05
25	6.8810E+00	1.3729E+05	1.3730E+05
27	6.6580E+00	1.5033E+04	1.5040E+04
29	8.1370E+00	1.7639E+05	1.7640E+05
30	8.1280E+00	1.5349E+03	1.5430E+03

Table 11. EIS data for all samples scan 1.

	Electrical Impedance Spectroscopy Scan 2		
	Impedance at 0.1 Hz		
Sample	Rs	Rp	Rs+Rp
	Ohm	Ohm	Ohm
1	8.8260E+00	4.2942E+03	4.3030E+03
1a	8.9270E+00	3.2211E+03	3.2300E+03
1b	7.5110E+00	3.5005E+03	3.5080E+03
2	7.6610E+00	1.7513E+03	1.7590E+03
2a	1.1310E+01	3.8237E+03	3.8350E+03
2b	8.8420E+00	7.2936E+02	7.3820E+02
3	8.2330E+00	7.0627E+02	7.1450E+02
4	8.2330E+00	8.1267E+02	8.2090E+02
5	9.0550E+00	9.7239E+03	9.7330E+03
6	8.7130E+00	1.6843E+03	1.6930E+03
6a	1.0450E+01	8.0096E+03	8.0200E+03
6b	8.9480E+00	2.8811E+03	2.8900E+03
7	1.0030E+01	8.5970E+03	8.6070E+03
7a	1.0160E+01	4.4688E+03	4.4790E+03
7b	9.9390E+00	1.2921E+03	1.3020E+03
8	1.1140E+01	5.9259E+03	5.9370E+03
9	9.4520E+00	8.2145E+03	8.2240E+03
9a	1.2860E+01	2.9091E+03	2.9220E+03
9b	8.3770E+00	6.4732E+02	6.5570E+02
10	9.5890E+00	5.9174E+03	5.9270E+03
11	1.1870E+01	4.6021E+03	4.6140E+03
12	9.0500E+00	2.1890E+03	2.1980E+03
12a	1.0020E+01	7.9890E+03	7.9990E+03
12b	1.1230E+01	2.5608E+03	2.5720E+03
13	8.3900E+00	1.2256E+03	1.2340E+03
14	8.9670E+00	7.6919E+05	7.6920E+05
14a	1.0260E+01	5.6747E+03	5.6850E+03
14b	8.6300E+00	2.3364E+03	2.3450E+03
15	9.5590E+00	6.3274E+02	6.4230E+02
16	1.0730E+01	6.0553E+03	6.0660E+03
17	9.8860E+00	5.6751E+03	5.6850E+03
18	1.0260E+01	7.8147E+03	7.8250E+03
19	7.9350E+00	1.0141E+03	1.0220E+03
21	7.6660E+00	9.7553E+02	9.8320E+02
23	6.9470E+00	1.9431E+03	1.9500E+03
25	7.5400E+00	3.5245E+03	3.5320E+03
27	7.1200E+00	8.0438E+02	8.1150E+02
29	8.9240E+00	6.2038E+02	6.2930E+02
30	9.5630E+00	6.0224E+02	6.1180E+02

Table 12. EIS data for all samples scan 2.

	Electrical Impedance Spectroscopy Scan 3		
	Impedance at 0.1 Hz		
Sample	Rs	Rp	Rs+Rp
	Ohm	Ohm	Ohm
1	1.0640E+01	7.9146E+02	8.0210E+02
1a	9.2030E+00	1.8968E+03	1.9060E+03
1b	8.2190E+00	4.0008E+03	4.0090E+03
2	7.7660E+00	1.1442E+03	1.1520E+03
2a	1.2590E+01	4.8014E+03	4.8140E+03
2b	8.5360E+00	2.3095E+03	2.3180E+03
3	7.7480E+00	1.2263E+03	1.2340E+03
4	8.0920E+00	9.6131E+02	9.6940E+02
5	9.4850E+00	4.9585E+03	4.9680E+03
6	7.5260E+00	2.0025E+03	2.0100E+03
6a	1.1170E+01	1.5988E+03	1.6100E+03
6b	8.6630E+00	1.7893E+03	1.7980E+03
7	9.8320E+00	1.3740E+04	1.3750E+04
7a	1.0500E+01	2.0570E+04	2.0580E+04
7b	1.0990E+01	2.1160E+03	2.1270E+03
8	1.0590E+01	5.1774E+03	5.1880E+03
9	9.4730E+00	1.0985E+03	1.1080E+03
9a	1.1700E+01	1.7163E+03	1.7280E+03
9b	8.1600E+00	2.9748E+03	2.9830E+03
10	1.0410E+01	7.6586E+03	7.6690E+03
11	1.0320E+01	8.4417E+03	8.4520E+03
12	8.5170E+00	1.7285E+03	1.7370E+03
12a	9.6570E+00	1.4963E+03	1.5060E+03
12b	9.6720E+00	1.8163E+03	1.8260E+03
13	7.5780E+00	3.2812E+02	3.3570E+02
14	1.1120E+01	9.5558E+02	9.6670E+02
14a	9.1300E+00	2.5341E+04	2.5350E+04
14b	7.8800E+00	2.5861E+03	2.5940E+03
15	8.8210E+00	5.6628E+02	5.7510E+02
16	1.0870E+01	3.1321E+03	3.1430E+03
17	1.1130E+01	7.2219E+03	7.2330E+03
18	1.0470E+01	1.6390E+04	1.6400E+04
19	8.1640E+00	2.4898E+03	2.4980E+03
21	8.3380E+00	2.4177E+03	2.4260E+03
23	7.2250E+00	6.0138E+03	6.0210E+03
25	7.6700E+00	3.6983E+03	3.7060E+03
27	8.8770E+00	2.3371E+03	2.3460E+03
29	8.9240E+00	2.0261E+03	2.0350E+03
30	8.7820E+00	2.2202E+03	2.2290E+03

Table 13. EIS data for all samples scan 3.

	<b>Electrical Impedance Spectroscopy Scan 4</b>		
	<b>Impedance at 0.1 Hz</b>		
<b>Sample</b>	<b>Rs</b>	<b>Rp</b>	<b>Rs+Rp</b>
	<b>Ohm</b>	<b>Ohm</b>	<b>Ohm</b>
1	8.2440E+00	3.8256E+02	3.9080E+02
1a	7.0970E+00	2.7169E+03	2.7240E+03
1b	7.8130E+00	4.6172E+03	4.6250E+03
2	7.9870E+00	4.6580E+03	4.6660E+03
2a	9.0710E+00	3.6879E+03	3.6970E+03
2b	8.6150E+00	2.7154E+03	2.7240E+03
3	8.6510E+00	1.4273E+03	1.4360E+03
4	8.2450E+00	2.3868E+03	2.3950E+03
5	8.4290E+00	2.1472E+04	2.1480E+04
6	7.6980E+00	2.8173E+03	2.8250E+03
6a	1.0600E+01	7.2200E+02	7.3260E+02
6b	9.2250E+00	2.1598E+03	2.1690E+03
7	9.3450E+00	8.1317E+03	8.1410E+03
7a	1.0020E+01	6.8520E+03	6.8620E+03
7b	1.1510E+01	1.8115E+03	1.8230E+03
8	1.1630E+01	5.6204E+03	5.6320E+03
9	8.4640E+00	3.2164E+02	3.3010E+02
9a	1.1820E+01	1.3972E+03	1.4090E+03
9b	8.1700E+00	3.6118E+03	3.6200E+03
10	1.1240E+01	1.2209E+04	1.2220E+04
11	1.1230E+01	6.1448E+03	6.1560E+03
12	8.5120E+00	2.8495E+03	2.8580E+03
12a	9.1600E+00	3.7124E+02	3.8040E+02
12b	8.5010E+00	2.1955E+03	2.2040E+03
13	7.0840E+00	3.0362E+02	3.1070E+02
14	9.1180E+00	3.7128E+02	3.8040E+02
14a	1.0150E+01	1.0100E+04	1.0110E+04
14b	8.8760E+00	4.3411E+03	4.3500E+03
15	8.8210E+00	5.6628E+02	5.7510E+02
16	1.0150E+01	5.4205E+02	5.5220E+02
17	1.1350E+01	7.4767E+03	7.4880E+03
18	1.0600E+01	8.9864E+03	8.9970E+03
19	8.8210E+00	2.7062E+03	2.7150E+03
21	8.1910E+00	3.1328E+03	3.1410E+03
23	7.3540E+00	4.3926E+03	4.4000E+03
25	8.0120E+00	6.5920E+03	6.6000E+03
27	7.7230E+00	3.3653E+03	3.3730E+03
29	9.8470E+00	2.6792E+03	2.6890E+03
30	8.7350E+00	3.0003E+03	3.0090E+03

Table 14. EIS data for all samples scan 4.

1. Supplemental Electrical Impedance Spectroscopy Comparison Charts for Sensitized Samples

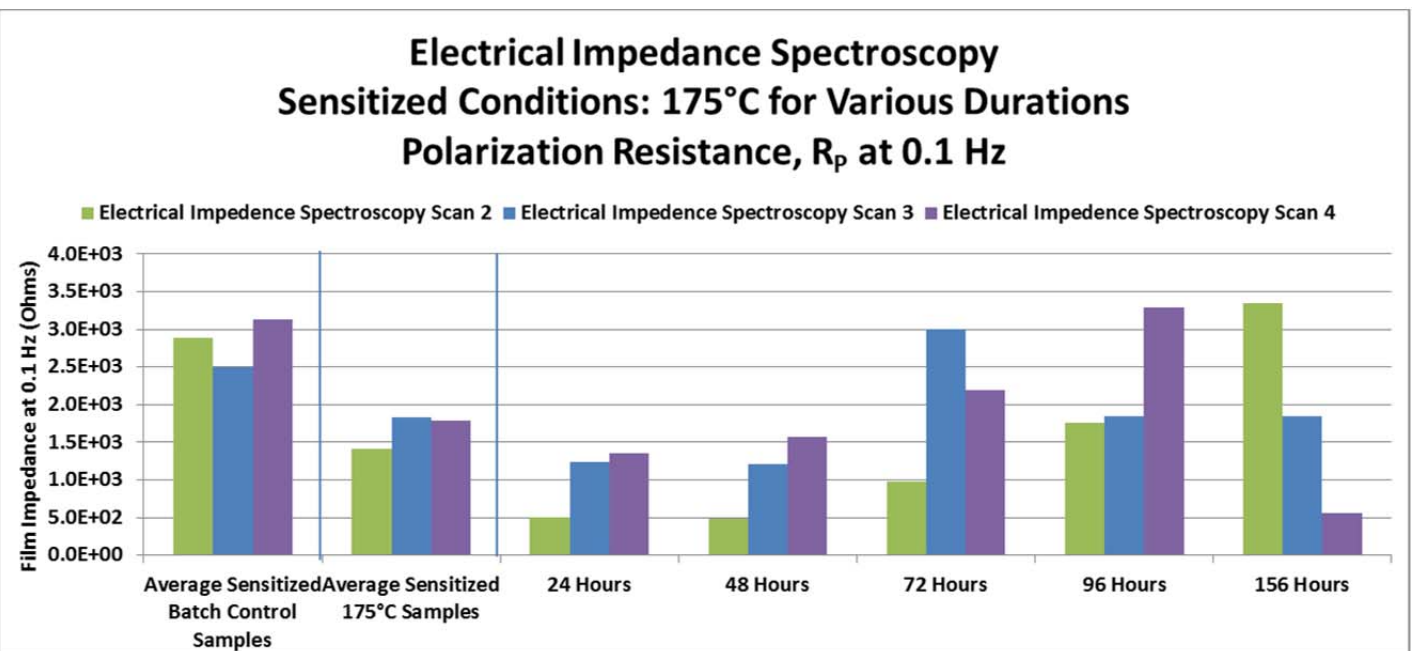
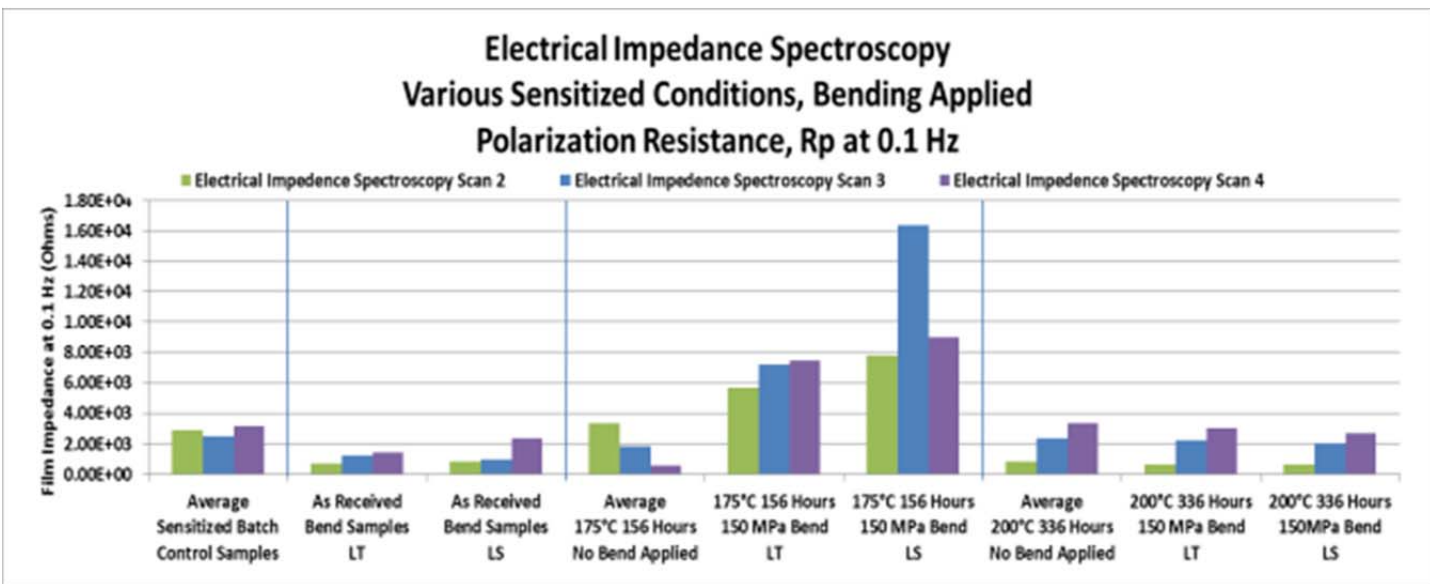


Figure 62. EIS sensitized conditions: 175°C for various durations, scans 2–4 comparison of

Figure 63. EIS various sensitized conditions, bending applied, scans 2–4 comparison of  $R_p$ .



$R_p$ .



**F. MODEL IMPEDENCE EDITOR DATA**

Sample	Scan 1			
	Impedance Model Editor			Rp-R2 Ohm
	R1 Ohm	R2 Ohm	C3 F	
1	9.0000E+00	1.3570E+03	1.2970E-06	4129.78
1a	6.5280E+00	8.8170E+00	3.7630E-07	-2.39
1b	6.9800E+00	3.6220E+02	5.1180E-07	2976.74
2	7.0480E+00	7.4040E+04	1.9030E-06	14843.31
2a	1.1180E+01	1.0840E+04	3.7080E-06	16349.89
2b	8.6500E+00	8.5040E+04	1.5770E-06	25051.92
3	7.7710E+00	2.4430E+05	6.7900E-07	11292.63
4	8.1720E+00	3.0340E+05	6.6160E-07	75892.06
5	9.5530E+00	1.9660E+04	9.8520E-07	61181.08
6	9.5150E+00	3.9590E+02	2.1740E-07	5254.47
6a	1.0640E+01	9.5530E+03	6.2380E-07	876736.78
6b	1.1230E+01	2.1030E+03	8.5800E-07	13837.99
7	7.6860E+00	1.5720E+01	9.8560E-07	25.47
7a	9.2870E+00	6.6310E+05	1.4290E-06	-16408.87
7b	1.0460E+01	1.1250E+03	1.8160E-05	39.97
8	1.0020E+01	3.0360E+03	4.7110E-07	10674.47
9	8.8460E+00	3.7480E+05	1.1700E-06	148991.46
9a	8.5780E+00	2.2170E+04	2.3670E-07	695721.10
9b	9.1120E+00	4.5810E+02	3.5450E-05	15.07
10	8.3190E+00	1.8770E+06	8.8920E-07	-1756508.15
11	1.0440E+01	1.0620E+05	8.9880E-07	49490.67
12	9.7060E+00	6.7690E+05	1.4050E-06	60891.38
12a	9.0850E+00	3.0720E+05	4.5870E-07	431590.67
12b	9.4630E+00	6.4880E+05	9.5810E-07	16491.40
13	6.8370E+00	1.4980E+01	9.3120E-07	13.94
14	9.5580E+00	7.0110E+05	1.1570E+06	68091.03
14a	9.3800E+00	3.2870E+05	1.0900E-06	155790.94
14b	7.6200E+00	2.5210E+05	8.4390E-07	172392.53
15	6.8320E+00	7.5140E+04	1.6000E-06	29351.33
16	9.5910E+00	2.8580E+05	9.9850E-07	35790.59
17	9.6430E+00	4.2350E+04	1.8820E-06	8371.07
18	8.8110E+00	1.2970E+05	1.3180E-06	39791.62
19	6.8780E+00	4.8860E+01	1.5270E-06	464.74
21	7.1910E+00	1.0990E+05	1.3830E-06	20793.03
23	6.8430E+00	8.7350E+04	1.7040E-06	21743.40
25	7.1990E+00	1.0740E+05	1.5520E-06	29893.12
27	6.8410E+00	1.0860E+04	2.3160E-06	4173.34
28	7.0840E+00	1.0910E+05	9.8070E-07	-109100.00
29	8.1920E+00	1.1090E+05	6.4560E-07	65491.86
30	7.7100E+00	1.2750E+02	8.4890E-07	1407.37

Table 15. Impedance Model Editor data scan 1.

Sample	Scan 2			
	Impedance Model Editor			Rp-R2 Ohm
	R1 Ohm	R2 Ohm	C3 F	
1	9.6480E+00	4.0890E+03	1.4270E-05	205.17
1a	9.4700E+00	3.1620E+03	1.6030E-05	59.07
1b	8.2890E+00	3.3810E+03	1.2820E-05	119.49
2	9.1670E+00	7.1200E+02	2.5760E-05	1039.34
2a	1.2720E+01	3.3640E+03	2.4220E-05	459.69
2b	9.1680E+00	7.1200E+02	2.5760E-05	17.36
3	8.9310E+03	6.8250E+02	1.6740E-05	23.77
4	8.8070E+00	7.8610E+02	1.6680E-05	26.57
5	9.4430E+00	9.2230E+03	1.0570E-05	500.95
6	9.4260E+00	1.6320E+03	1.1450E-05	52.29
6a	1.0960E+01	7.5960E+03	9.8070E-06	413.55
6b	9.5150E+00	2.8060E+03	1.1210E-05	75.05
7	1.0750E+01	6.8150E+03	1.7450E-05	1781.97
7a	1.1020E+01	7.3170E+03	1.0010E-05	-2848.16
7b	1.0390E+01	1.2570E+03	2.0860E-05	35.06
8	1.2450E+01	5.5930E+03	9.9340E-06	332.86
9	1.0550E+01	7.7510E+03	9.3340E-06	463.55
9a	1.6650E+01	2.7590E+03	6.3040E-06	150.14
9b	8.6680E+00	6.3120E+02	3.9460E-05	16.12
10	1.0130E+01	5.6560E+03	9.0140E-06	261.41
11	1.2960E+01	4.3570E+03	8.7800E-06	245.13
12	1.0990E+01	4.4680E+03	1.0380E-05	-2279.05
12a	1.2070E+01	2.4560E+03	9.2600E-06	5532.98
12b	9.5760E+00	2.1130E+03	1.0170E-05	447.77
13	9.2760E+00	6.7650E+02	1.6160E-05	549.11
14	1.1240E+01	8.5920E+03	9.2820E-06	760599.03
14a	1.0740E+01	5.3600E+03	8.6410E-06	314.74
14b	9.1360E+00	2.2450E+03	8.4800E-06	91.37
15	9.8190E+00	2.7960E+03	1.7940E-05	-2163.26
16	1.1270E+01	5.4870E+03	2.1120E-05	568.27
17	1.0860E+01	4.9960E+03	2.0030E-05	679.11
18	1.0660E+01	6.9640E+03	2.0030E-05	850.74
19	8.4510E+00	9.8500E+02	2.0430E-05	29.07
21	7.9800E+00	9.5000E+02	2.1180E-05	25.53
23	7.3020E+00	1.8090E+03	1.9160E-05	134.05
25	8.3750E+00	2.6540E+03	2.0910E-05	870.46
27	7.4400E+00	7.7990E+02	2.1470E-05	24.48
28	9.5810E+00	4.4320E+02	2.1780E-05	-443.20
29	9.2970E+00	6.0070E+02	1.9000E-05	19.68
30	2.5900E+00	5.8570E+02	1.9150E-05	16.54

Table 16. Impedance Model Editor data scan 2.

Sample	Scan 3			
	Impedance Model Editor			Rp-R2 F
	R1 Ohm	R2 Ohm	C3 Ohm	
1	1.1450E+01	5.0690E+02	2.1470E-05	284.56
1a	1.1770E+01	1.7210E+04	3.9060E-06	-15313.20
1b	8.6440E+00	3.7230E+03	1.7600E-05	277.78
2	8.2050E+00	6.2010E+02	3.0430E-05	524.13
2a	1.3950E+01	4.3690E+03	3.0860E-05	432.41
2b	8.9180E+00	2.1560E+03	2.3960E-05	153.46
3	1.0830E+01	1.7910E+03	2.6960E-05	-564.75
4	8.4370E+00	9.3680E+02	2.6790E-05	24.51
5	9.9790E+00	3.7590E+03	1.8400E-05	1199.52
6	7.9380E+00	1.9520E+03	1.4020E-05	50.47
6a	1.1630E+01	1.0470E+03	1.8240E-05	551.83
6b	9.0330E+00	1.7310E+03	1.6690E-05	58.34
7	1.0330E+01	1.2410E+04	1.4380E-05	1330.17
7a	1.1410E+01	1.9170E+04	1.3090E-05	1399.50
7b	1.1560E+01	2.0570E+03	1.8700E-05	59.01
8	1.1470E+01	4.7240E+03	1.5860E-05	453.41
9	1.0790E+01	5.9230E+02	1.9590E-05	506.23
9a	1.3360E+01	1.6490E+03	9.8810E-06	67.30
9b	8.4700E+00	2.9070E+03	2.5130E-05	67.84
10	1.1080E+01	6.4880E+03	1.6610E-05	1170.59
11	1.1020E+01	6.9190E+03	1.5690E-05	1522.68
12	1.0390E+01	4.2300E+02	2.2650E-05	1305.48
12a	1.0260E+01	1.7580E+03	1.4080E-05	-261.66
12b	8.8930E+00	1.6790E+03	1.4590E-05	137.33
13	8.4910E+00	1.8240E+02	4.5340E-05	145.72
14	1.2150E+01	5.3930E+02	1.8640E-05	416.28
14a	9.5940E+00	1.3620E+04	9.0540E-06	11720.87
14b	2.2556E-02	2.5060E+03	1.2230E-05	80.12
15	1.0220E+01	4.2240E+02	2.7840E-05	143.88
16	1.1460E+01	2.8630E+03	2.1780E-05	269.13
17	1.1850E+01	6.5960E+03	2.4340E-05	625.87
18	1.1030E+01	1.2260E+04	1.8560E-05	4129.53
19	8.6520E+00	2.4210E+03	1.7400E-05	68.84
21	8.7230E+00	2.3520E+03	1.6850E-05	65.66
23	7.6050E+00	5.1950E+03	1.5300E-05	818.78
25	8.1760E+00	3.2390E+03	1.9050E-05	459.33
27	9.3410E+00	2.2470E+03	1.9720E-05	90.12
28	8.8810E+00	1.1440E+03	2.2180E-05	-1144.00
29	9.3360E+00	1.9670E+03	1.6730E-05	59.08
30	9.1640E+00	2.1240E+03	1.5390E-05	96.22

Table 17. Impedance Model Editor data scan 3.

Sample	Scan 4			
	Impedance Model Editor			Rp-R2 Ohm
	R1 Ohm	R2 Ohm	C3 F	
1	8.9520E+00	2.2130E+02	4.3590E-05	161.26
1a	7.4940E+00	2.7600E+03	1.6590E-05	-43.10
1b	8.1290E+00	4.5170E+03	1.6790E-05	100.19
2	8.5020E+00	3.9820E+03	1.5690E-05	676.01
2a	1.0180E+01	3.1400E+03	2.9650E-05	547.93
2b	8.9950E+00	2.5960E+03	2.4110E-05	119.39
3	9.0720E+00	1.3900E+03	2.0610E-05	37.35
4	8.5940E+00	2.3230E+03	2.3350E-05	63.76
5	8.8520E+00	1.9440E+04	1.7130E-05	2031.57
6	8.1070E+00	2.7630E+03	1.3830E-05	54.30
6a	1.1070E+01	4.6690E+02	2.6150E-05	255.10
6b	9.6660E+00	2.1200E+03	1.3650E-05	39.78
7	9.7470E+00	7.7950E+03	1.5360E-05	336.66
7a	1.0690E+01	6.7060E+03	1.3090E-05	145.98
7b	1.2080E+01	1.7620E+03	2.1330E-05	49.49
8	1.2910E+01	4.9310E+03	2.0400E-05	689.37
9	9.2960E+00	1.7020E+02	5.3130E-05	151.44
9a	1.3510E+01	1.3490E+03	1.2830E-05	48.18
9b	8.5090E+00	3.5450E+03	2.5970E-05	66.83
10	1.1820E+01	1.1200E+04	1.5150E-05	1008.76
11	1.1790E+01	5.7010E+03	1.3690E-05	443.77
12	9.0500E+00	1.9390E+02	3.7160E-05	2655.59
12a	8.9480E+00	2.1320E+03	1.5560E-05	-1760.76
12b	8.9040E+00	2.7810E+03	1.5200E-05	-585.50
13	8.0040E+00	1.6720E+02	4.1080E-05	136.42
14	9.8610E+00	2.1120E+02	4.3130E-05	160.08
14a	1.0610E+01	9.9550E+03	1.2100E-05	144.85
14b	9.5150E+00	4.2250E+03	1.1030E-05	116.12
15	9.5020E+00	3.7930E+02	5.0090E-05	186.98
16	1.0760E+01	3.6740E+02	3.7880E-05	174.65
17	1.2090E+01	6.9900E+03	2.5720E-05	486.65
18	1.1140E+01	4.4730E+03	1.7980E-05	4513.40
19	9.3100E+00	2.6320E+03	1.8690E-05	74.18
21	8.5490E+00	3.0560E+03	1.7630E-05	76.81
23	7.7370E+00	4.2090E+03	1.5820E-05	183.65
25	8.5040E+00	5.9670E+03	1.5890E-05	624.99
27	8.1640E+00	3.1970E+03	2.0080E-05	168.28
28	8.3300E+00	2.1800E+03	1.9080E-05	-2180.00
29	1.0310E+01	2.5860E+03	1.6490E-05	93.15
30	9.1240E+00	2.8910E+03	1.5970E-05	109.27

Table 18. Impedance Model Editor data scan 4.

**G. SUMMARY TABLE DATA SCANS 1–3 EIS AND CP**

Scan 1		R <sub>p</sub>	E <sub>CORR</sub>	i <sub>p</sub>	ΔE <sub>CRIT</sub>	ΔE <sub>RP</sub>
Rolling Direction	Bending Applied	Ohm	V	A/cm <sup>2</sup>	V	V
<b>As Received (No Sensitization)</b>						
T	0 MPa	5486.78	-0.6609	2.06E-05	0.6609	-0.1839
	150 Mpa	255592.63	-0.6570	4.19E-06	0.6570	-0.1899
L	0 MPa	88883.31	-0.7470	6.00E-06	0.7470	-0.1348
	150 MPa	379292.06	-0.6987	3.64E-06	0.6987	-0.1349
<b>Sensitized 175°C for 156 Hours</b>						
T	0 MPa	321590.59	-0.6705	6.20E-06	0.6705	-0.1779
	150 Mpa	50721.07	-0.8235	1.41E-05	0.8235	0.0111
L	0 MPa	104491.33	-0.8284	9.94E-06	0.8284	0.0075
	150 MPa	169491.62	-0.8406	1.15E-05	0.8406	0.0100
<b>Sensitized 200°C for 336 Hours</b>						
T	0 MPa	15033.34	-0.7485	6.34E-06	0.7485	-0.0909
	150 Mpa	1534.87	-0.7651	5.27E-06	0.7651	-0.0648
L	0 MPa	15033.34	-0.7485	6.34E-06	0.7485	-0.0909
	150 MPa	176391.86	-0.7492	3.93E-06	0.7492	-0.0860

Table 19. EIS and CP scan 1 data, applied tension comparison of samples without sensitization, samples exposed to 175°C for 156 hours, and samples exposed to and 200°C for 336 hours.

Scan 2		R <sub>p</sub>	E <sub>CORR</sub>	i <sub>p</sub>	ΔE <sub>CRIT</sub>	ΔE <sub>RP</sub>
Rolling Direction	Bending Applied	Ohm	V	A/cm <sup>2</sup>	V	V
<b>As Received (No Sensitization)</b>						
T	0 MPa	4294.17	-0.9714	8.63E-06	0.2609	0.1760
	150 Mpa	706.27	-0.9866	1.15E-05	0.2426	0.1710
L	0 MPa	1751.34	-1.1280	1.65E-05	0.4028	0.3182
	150 MPa	812.67	-0.9907	1.23E-05	0.2478	0.1707
<b>Sensitized 175°C for 156 Hours</b>						
T	0 MPa	6055.27	-1.1800	1.51E-05	0.4753	0.4014
	150 Mpa	5675.11	-0.9352	8.69E-06	0.1809	0.1468
L	0 MPa	632.74	-1.1170	1.38E-05	0.4107	0.3407
	150 MPa	7814.74	-1.0630	8.06E-06	0.3500	0.2879
<b>Sensitized 200°C for 336 Hours</b>						
T	0 MPa	804.38	-0.9332	1.13E-05	0.1699	0.1410
	150 Mpa	602.24	-1.0580	1.79E-05	0.3124	0.2654
L	0 MPa	804.38	-0.9332	1.13E-05	0.1699	0.1410
	150 MPa	620.38	-0.9981	1.43E-05	0.2418	0.2059

Table 20. EIS and CP scan 2 data, applied tension comparison of samples without sensitization, samples exposed to 175°C for 156 hours, and samples exposed to

and 200°C for 336 hours.

<b>Scan 3</b>		<b>R<sub>p</sub></b>	<b>E<sub>CORR</sub></b>	<b>i<sub>p</sub></b>	<b>ΔE<sub>CRIT</sub></b>	<b>ΔE<sub>RP</sub></b>
Rolling Direction	Bending Applied	<b>Ohm</b>	<b>V</b>	<b>A/cm<sup>2</sup></b>	<b>V</b>	<b>V</b>
<b>As Received (No Sensitization)</b>						
T	0 MPa	791.46	-1.1410	3.60E-05	0.4000	0.3641
	150 MPa	1226.25	-1.1010	2.17E-05	0.3462	0.2941
L	0 MPa	1144.23	-1.1370	2.70E-05	0.3826	0.3295
	150 MPa	961.31	-1.1440	3.25E-05	0.4079	0.3527
<b>Sensitized 175°C for 156 Hours</b>						
T	0 MPa	3132.13	-1.1520	2.47E-05	0.4322	0.3823
	150 MPa	7221.87	-1.0720	2.16E-05	0.3103	0.2924
L	0 MPa	566.28	-1.1460	3.70E-05	0.4218	0.3807
	150 MPa	16389.53	-1.0650	1.23E-05	0.3233	0.2904
<b>Sensitized 200°C for 336 Hours</b>						
T	0 MPa	2337.12	-0.9814	1.57E-05	0.2189	0.1919
	150 MPa	2220.22	-1.0670	2.09E-05	0.3148	0.2788
L	0 MPa	2337.12	-0.9814	1.57E-05	0.2189	0.1919
	150 MPa	2026.08	-1.0950	2.07E-05	0.3367	0.3087

Table 21. EIS and CP scan 3 data, applied tension comparison of samples without sensitization, samples exposed to 175°C for 156 hours, and samples exposed to and 200°C for 336 hours

THIS PAGE INTENTIONALLY LEFT BLANK

## LIST OF REFERENCES

- [1] M. G. Fontana, *Corrosion Engineering*, Third ed. Singapore: McGraw-Hill, 1986.
- [2] Austal Shipyards, “Aluminum hull structure in naval applications,” Austal Shipyards [Online]. Available: <http://www.austal.com/Libraries/Newsletters-Presentations-Presentations-and-Publications/Aluminium---Hull-Structure-in-Naval-Applications.pdf>.
- [3] S. Jain, M. L. C. Lim, J. L. Hudson, and J. R. Scully, “Spreading of intergranular corrosion on the surface of sensitized al-4.4Mg alloys: A general finding,” *Corrosion Science*, no. 59, pp. 136–147, 2012.
- [4] ElectraWatch Inc., “U.S. Navy Ships,” ElectraWatch, Inc., 2009 [Online]. Available: <http://www.electrawatch.com/Ships.html>.
- [5] E. D. Thomas II, “Cost of Corrosion for Ships, Submarines, and Naval Aviation,” *SAE International*, 2012. Available: [http://www.sae.org/events/DoD/presentations/2012/cost\\_of\\_corrosion\\_for\\_ships\\_submarines\\_and\\_naval\\_aviation.pdf](http://www.sae.org/events/DoD/presentations/2012/cost_of_corrosion_for_ships_submarines_and_naval_aviation.pdf).
- [6] New York Times, “Navy reverting to steel in shipbuilding after cracks in aluminum,” *New York Times*, New York, 11 August, 1987.
- [7] A. Butler-Franco, *Request for Information*, S.E. Washington Navy Yard, DC: Department of the Navy, Naval Sea Systems Command, NAVSEA HQ, 2012.
- [8] P. J. Regis, FFG 7 Class Advisory No. 06–95, Arlington, VA: NAVSEA, 1995.
- [9] R. Schwarting, G. Ebel, and T. J. Dorsch, “Manufacturing techniques and process challenged with CG47 class ship aluminum superstructures modernization and repairs,” in *Fleet Maintenance & Modernization Symposium 2001: Assessing Current & Future Maintenance Strategies*, BAE Systems, San Diego, October 2011. [Online] Available: <https://www.navalengineers.org/SiteCollectionDocuments/2011%20Proceedings%20Documents/FMMS2011/Presentations/Schwarting.pdf>
- [10] Defense Industry Daily, “LCS: The USA’s Littoral Combat Ships,” *Defense Industry Daily*, 13 May, 2013. [Online]. Available: <http://www.defenseindustrydaily.com/the-usas-new-littoral-combat-ships-updated-01343/>
- [11] DOT&E, “Littoral Combat Ship (LCS),” Navy Programs, Director, Operational Test and Evaluation (DOT&E), 2012. [Online] Available: <http://www.dote.osd.mil/pub/reports/fy2012/pdf/navy/2012lcs.pdf>

- [12] N. Birbilis and R. Buchheit, "Electrochemical characteristics of intermetallic phases in aluminum alloys - An experimental survey and discussion," *Journal of Electrochemistry Society*, vol. 152, no. 4, 9pp. B140-B151, 2005.
- [13] J. L. Searles, P. I. Gouma, and R. G. Buchheit., "Stress corrosion cracking of sensitized AA5083 (Al-4.5Mg-1.0Mn)," *Metallurgical and Materials Transactions*, vol. 32A, no. 11, pp. 2859–2867, 2001.
- [14] F. Latrash, B. Conner, and D. Novak, "Advantages of Aluminum in Marine Applications: Lighter, Faster, Stronger," Alcoa Defense Inc., Alcoa Business System. [Online] Available: [http://www.alcoa.com/global/en/news/webinar/al\\_shipbuilding/alcoa\\_defense\\_and\\_abs\\_webinar.pdf](http://www.alcoa.com/global/en/news/webinar/al_shipbuilding/alcoa_defense_and_abs_webinar.pdf)
- [15] I. N. Oguocha, O. J. Adigun, and S. Yannacopoulos, "Effect of sensitization heat treatment on properties of Al-Mg alloy AA5083-H116," *Journal Of Materials Science*, vol. 43, pp. 4208–4214, 2008.
- [16] MatWeb LLC., "Aluminum alloy heat treatment temper designations," MatWeb LLC, Material Property Data, [Online] Available: <http://www.matweb.com/reference/aluminumtemper.aspx>.
- [17] Aluminum Association, Inc., "International alloy designations and chemical composition limits for wrought aluminum and wrought aluminum alloys," Arlington, VA: The Aluminum Association, 2009. [Online] Available: [http://www.aluminum.org/Content/NavigationMenu/TheIndustry/IndustryStandards/Teal\\_Sheets.pdf](http://www.aluminum.org/Content/NavigationMenu/TheIndustry/IndustryStandards/Teal_Sheets.pdf)
- [18] M. Collette and R. Sielski, "Aluminum ship structures," ASNE Day 2013, Marine Structures Design Laboratory. [Online] Available: [https://www.navalengineers.org/ProceedingsDocs/ASNEDay2013/Collette\\_Paper.pdf](https://www.navalengineers.org/ProceedingsDocs/ASNEDay2013/Collette_Paper.pdf)
- [19] ASM International, "Properties and selection: Non-ferrous alloys and special purpose metals," *ASM Handbook*, vol. 2. ASM International, 1990.
- [20] B. Scott, "The role of stress in the corrosion cracking of aluminum alloys," M.S. thesis, Dept. Mech. and Aero. Eng., Naval Postgraduate School, Monterey, CA, 2013.
- [21] J. Kaufman, Introduction to Aluminum Alloys and Tempers. Materials Park, OH: *ASM International*. 2000.
- [22] J. E. Hatch, Aluminum: Properties and Physical Metallurgy. Metals Park, OH: *ASM International*, vol. 1, 1984, p. 295.

- [23] A. H. Clausen, T. Borvik, O. S. Hopperstad, and A. Benallal, “Flow and fracture characteristics of aluminum alloy AA5083-H116 as function of strain rate, temperature, and triaxiality,” *Material Science Engineering*, p. A364:260, 2004.
- [24] J. R. Davis, “Corrosion of aluminum and aluminum alloys,” *ASM International*, 2<sup>nd</sup> ed. 1999, p. 313.
- [25] L. Kramer, M. Phillippi, W. T. Track, and C. Wong, “Locally reversing sensitization in 5xxx aluminum plate,” *Journal of Materials Engineering and Performance*, vol. 21, issue 6, pp. 1025–1029, June 2012. [Online] Available: [https://ext.sharepoint.ctc.com/ctcComContent/StageMedia/General%20News/Journal%20Article\\_Sensitization.pdf](https://ext.sharepoint.ctc.com/ctcComContent/StageMedia/General%20News/Journal%20Article_Sensitization.pdf).
- [26] E. C. Cormack, “The effect of sensitization on the stress corrosion cracking of aluminum alloy 5456,” M.S. thesis, Dept. Mech. and Aero. Eng., Naval Postgraduate School, Monterey, CA, 2012.
- [27] R. S. Hafner and J. C. Farmer, “Modeling and mitigation of stress corrosion cracking in closure welds of high-level waste containers for Yucca Mountain,” *Transportation, Storage, and Disposal of Radioactive Materials, American Society of Mechanical Engineers: Pressure Vessels and Piping Division, Pressure Vessels and Piping Conference*, Seattle, WA, 2000.
- [28] H. R. Mattern, “Laser peening for mitigation of stress corrosion cracking at welds in marine aluminum,” M.S. thesis, Dept. Mech. and Aero. Eng., Naval Postgraduate School, Monterey, CA, 2011.
- [29] M. Pourbaix, *Atlas of Electrochemical Equilibria in Aqueous Solutions, Aluminum*. pp. 168–176, Houston, TX: NACE, 1974.
- [30] Y. Uematsu, T. Kakiuchi, and N. Masaki, “Stress corrosion cracking behavior of the wrought magnesium alloy AZ31 under controlled cathodic potentials,” *Materials Science and Engineering A*, vol. 531, pp. 171–177, 01 January, 2012.
- [31] G. M. Abady, N. H. Hilal, M. El-Rabiee, and W. A. Badawy, “Effect of Al content on the corrosion behavior of Mg-Al alloys in aqueous solutions of different pH,” *Electrochimica Acta*, vol. 55, no. 22, pp. 6651–6658, 2010.
- [32] R. G. Buchheit, R. K. Boger, M. C. Carroll, R. M. Leard, C. Paglia, and J. L. Searles, “The electrochemistry of intermetallic particles and localized corrosion in Al alloys,” *JOM*, vol. 53, issue 7, pp. 29–33, 2001.
- [33] A. R. Troiano, R. Gibala, and R. F. Hehemann, *Hydrogen embrittlement and stress corrosion cracking*, American Society for Metals, 1984.
- [34] R. H. Jones, “Stress-corrosion cracking,” *ASM International*, 1992.

- [35] D. W. Sokol, "Preventing fatigue failures with laser peening," Metal Finishing News, Zurich, Switzerland.
- [36] L. Hackel and J. Rankin, "Production Laser Peening of High Strength Metals," Metal Improvement Company, Livermore, CA.
- [37] A. Andreasen, Properties of MgAl alloys in Relation to Hydrogen Storage, Rise National Lab, Materials Research Dept., DK, 2005.
- [38] M. N. de Noirfontaine, "High Temperature Oxidation of the Al<sub>3</sub>Mg<sub>2</sub> Complex Metallic Alloy," *Oxid Met*, vol. 73, pp. 219–232, September 2009.
- [39] J. C. Farmer and S. Menon, "General corrosion, localized corrosion, and environmental cracking of modern engineering materials," *Encyclopedia of Life Support Systems*, 2011.
- [40] K. A. Gruss, G. A. Cragolino, D. S. Dunn, and N. Sridhar, "Repassivation potential for localized corrosion of alloys 625 and C22 in simulated repository environments," in *Proceedings of Corrosion 98*, San Diego, CA, 1998.
- [41] D. C. Silverman, "Tutorial on Polexpert™ and the cyclic potentiodynamic polarization technique," *NACE International*, Houston, TX.
- [42] R. Baboian, "Primer on the AC impedance technique," *Electrochemical Techniques for Corrosion Engineering*, NACE, 1987.
- [43] E. Barsoukov and J. R. Macdonald, *Impedance Spectroscopy: Theory, Experiment, and Applications*, John Wiley & Sons, 2005.
- [44] D. C. Silverman and J. E. Carrico, "Electrochemical impedance technique – A practical tool for corrosion prediction," *Corrosion*, vol. 44, no. 5, p. 280, 1988.
- [45] J. Farmer, S. Menon, P. Legrand, and L. Hackel, "Studies of passive films on friction stir processed and laser peened NiAl bronze," *Corrosion Resistant Metal Alloys, III, DoD Corrosion Conference, July 31 - August 5 2011, Palm Springs CA, NACE paper 20194*, National Association of Corrosion Engineers, Houston, TX, 2011.
- [46] J. Farmer, T. Omlor, S. Menon, and L. Brewer, "Long-term corrosion resistance of iron-based amorphous metal coatings II," in *DOD Corrosion Conference*, Palm Springs, CA, 31 July - 5 August, 2011.
- [47] D. C. Silverman, "Sterling guidance on corrosion and materials degradation," [Online] Available: [http://www.argentumsolutions.com/tutorials/impedance\\_tutorialpg3.html](http://www.argentumsolutions.com/tutorials/impedance_tutorialpg3.html).

- [48] ASTM International, “Standard practice for preparation and use of bent-beam stress-corrosion test specimens,” *ASTM G39*.
- [49] Thermo Fisher Scientific Inc., “Product listing: Fisher Scientific™ Accumet™ glass body Ag/AgCl reference electrodes – mercury-free,” Fisher Scientific. [Online] Available: [http://www.fishersci.com/ecom/servlet/fsproductdetail\\_10652\\_1430310\\_-1\\_0](http://www.fishersci.com/ecom/servlet/fsproductdetail_10652_1430310_-1_0).
- [50] Gamry Instruments, “Reference electrodes,” Gamry Instruments, 2013. [Online] Available: <http://www.gamry.com/products/accessories/reference-electrodes/>.
- [51] R. H. Jones, V. Y. Gertsman, J. S. Vetrano, and C.F. Windisch, Jr., “Crack-particle interactions during intergranular stress corrosion of AA5083 as observed by cross-section transmission electron microscopy,” *Scripta Materialia*, vol. 50, pp. 1355–1359, 2004.
- [52] K. N. Tran, M. R. Hill, and L. A. Hackel, “Laser shock peening improves fatigue life of lightweight alloys,” *Welding Journal*, pp. 28–31.
- [53] B. J. Banazwski, “Using x-ray diffraction to assess residual stresses in laser peened and welded aluminum,” M.S. thesis, Dept. Mech. and Aero. Eng., Naval Postgraduate School, Monterey, CA, 2011.

THIS PAGE INTENTIONALLY LEFT BLANK

## **INITIAL DISTRIBUTION LIST**

1. Defense Technical Information Center  
Ft. Belvoir, Virginia
2. Dudley Knox Library  
Naval Postgraduate School  
Monterey, California